UNIVERSITÀ
DEGLI STUDI
FIRENZE

**Scuola di**
**Scienze Matematiche**
**Fisiche e Naturali**

Corso di Laurea Specialistica in
Scienze Fisiche e Astrofisiche

# Interferometria atomica con un Condensato di Bose-Einstein in un potenziale a doppia buca

# Atom interferometry with a Bose-Einstein Condensate in a double-well potential

**Relatore**
Prof. Massimo Inguscio

**Candidato**
Giacomo Colzi

Anno Accademico 2013/2014

# Contents

# Introduction

The experimental realization of Bose-Einstein Condensation (BEC) is one of the most important scientific achievements of the last two decades. Beyond the fundamental physical interest of the phenomenon per se, it triggered a revolution allowing for the experimental simulation of quantum systems with experimentally tunable parameters. BECs are indeed characterized by a matter wavefunction coherent over macroscopic length scales, easily manipulated with different kinds of trapping potentials and observable with modern optical microscopy techniques. Control over interatomic interactions in cold atoms experiments is also possible via well-established techniques that exploit Feshbach Resonances.

In this framework, one of the simplest and more promising quantum system to study is the BEC trapped in a double-well potential with tunable interatomic interactions. This system is very interesting from a fundamental viewpoint, since it is the realization of a Bosonic Josephson Junction (BJJ) that allows to study the underlying physics with a degree of control and tunability over the system parameters unmatched by its solid state counterparts. From the viewpoint of metrological applications, this system allows to devise compact atomic interferometers with very high spatial resolution (on the micrometric scale) and with interrogation times limited only by the stability of the system. BECs in this context represent the analogous of the lasers in the field of optical interferometry and are considered one of the most promising candidates for high precision measurements. Finally, another fundamental characteristic of this system is the possibility to construct, control and study Entangled states exploiting the control over interatomic interactions. Entangled states are very interesting from the fundamental viewpoint and for the broad emerging field of quantum-enhanced technologies; moreover in metrological applications, including the above mentioned interferometers, they can be exploited to overcome the maximum precision limit set by quantum

fluctuations of uncorrelated atomic states, or "Shot Noise Limit".

In this Thesis I report on the experimental activity devoted to the development of a double-well trapping potential for high sensitivity atom interferometry, studies on quantum entanglement and simulation of condensed matter physics. We have been able to observe, for the first time, coherent phase evolution for a macroscopic number of atoms (about $10^3$) over a timescale of $\sim 200\, ms$, beating by one order of magnitude state-of the art similar experiments. This striking result was obtained thanks to the insightful choice of $^{39}K$ as the species to be condensed: the degree of control with which the effective interatomic interactions can be set to zero outperforms other alkali atoms traditionally used in cold atom experiments. We were also able to prepare the condensate in a single well and, after coupling it via tunneling with the other well over a distance of $5\, \mu m$, observe periodic oscillations in the population of the two wells for essentially the same amount of time as the coherent evolution, that is another unprecedented result on a double-well interferometer of this interwell separation and atom number scales.

This Thesis is organized in this way. In the first chapter I will give a general introduction to the phenomenon of Bose-Einstein Condensation for non-interacting trapped atoms and for weakly interacting atoms in the mean-field approximation. Then the Double-Well system will be discussed in the two mode approximation, highlighting some of its features relevant for interferometric applications. In the second Chapter I will describe the atomic Mach-Zehnder interferometer operations using the Bloch Sphere representation, with particular attention to the reachable precision limits and the advantages of interaction tunability. In the third Chapter I describe the whole experimental apparatus. Then, in the fourth Chapter i describe in details a Second Harmonic Generation of light stage constructed during the Thesis, focusing on the important aspects to keep into consideration when optimizing the crystal operations. In the fifth Chapter, I will describe the important results obtained in the general experimental framework; from the frequency of the coherent oscillations in phase and population we were able to experimentally quantify the parameters of the Hamiltonian describing the non-interacting system, namely the tunneling energy and the energy imbalance between the two wells. From the experimental measurement of the phase coherence of the system and the theoretical modeling of how it is affected by thermal fluctuations we estimated an upper bound for the temperature of our condensate, at least one order of magnitude below

the transition temperature, where the thermal fraction of atoms is negligible and cannot be quantified by direct observation of the expanding condensate.

# Chapter 1

# Theory of BEC in a Double-Well potential

In this Chapter I will give a general survey to the theory of BEC in a double well potential reporting several known results necessary to contextualize the system properties in the framework of quantum interferometry . In the first Section an introduction to the Bose-Einstein Condensation phenomenon for an ideal gas will be given. In the second Section the relevant properties of Bose-Einstein condensation for non-interacting particles will be reported for atoms confined in a 3D harmonic trap. In the third Section the well-known derivation of the Gross-Pitaevskii Equation (GPE) will be reported starting from the general Many-Body Hamiltonian for a weakly-interacting BEC. The fourth Section will be devoted to discussing the stationary properties of the BEC confined in a double-well potential, following closely the approach found in[45]. It will be demonstrated that the system Hamiltonian reduces to a two-mode Bose-Hubbard Hamiltonian within the two-level approximation for the double-well system , its energy spectrum will be computed and the system coherence will be discussed with particular attention to the interplay between thermal fluctuations and interaction energy.

## 1.1 Bose-Einstein Condensation Theory

### 1.1.1 Bose-Einstein Condensation for an ideal gas

Bose-Einstein Condensation is a phenomenon theorized in 1924 [1, 2], and observed experimentally for the first time in 1995 [3, 4]. It corresponds to the macroscopic occupation of the system ground state below a nonzero critical temperature $T_C$. This behavior directly depends on the particle exchange symmetry of Bosons and does not require, ideally, the presence of interactions. Deviations from the classically predicted behavior of the system are to be expected in the regime of low energies or high density. Introducing the length scale over which the quantum nature of the atoms start to play an important role, identified with De Broglie's thermal wavelength [8]

$$\lambda_T = \sqrt{\frac{2\pi\hbar^2}{mk_BT}} \tag{1.1.1}$$

where $\hbar$ is the reduced Planck constant, $m$ is the atomic mass and $k_B$ is the Boltzmann constant, we can estimate the condensation temperature for a 3D system requiring the mean distance between atoms to be of the same order of magnitude of the thermal wavelength

$$\lambda_{T_C}^3 n = \rho \sim 1 \tag{1.1.2}$$

$\rho$ is defined as the Phase Space Density (PSD) of the quantum gas. The functional dependence of the transition temperature $T_C$ on the atomic density $n$ for a uniform system is

$$T_C \propto n^{2/3} \tag{1.1.3}$$

To study the thermodynamic properties one can start from the mean thermal occupation of non degenerate single-particle states for bosons, obtained from the Grancanonical ensemble [5]

$$\langle n_i \rangle = \frac{1}{e^{\beta(\epsilon_i - \mu)} - 1} \tag{1.1.4}$$

where $\beta = \frac{1}{k_BT}$, $\mu$ is the chemical potential and $\epsilon_i$ is the energy of the $i$-th state. The thermal dependence of $\mu(T)$ is obtained fixing the mean number of atoms in the system (in

the grancanonical ensemble)

$$N = \sum_i \frac{1}{e^{\beta(\epsilon_i - \mu)} - 1} \tag{1.1.5}$$

To have a positive distribution of occupation numbers the chemical potential must be less than the single particle energies $\epsilon_i$ for every value of $i$, hence less than the ground state energy

$$\mu \leq \epsilon_0 \tag{1.1.6}$$

This condition bounds the excited states occupation number

$$\langle n_i \rangle \leq \frac{1}{e^{\beta(\epsilon_i - \epsilon_0)} - 1} \qquad (i \neq 0) \tag{1.1.7}$$

while the ground state occupation number can diverge. Fixing the system temperature, there will be a particle number $N$ above which all the excess particles will have to occupy the fundamental state. In the same way fixing the atom number and reducing the system temperature may require a macroscopic fraction of the atoms to occupy the ground state of the system to satisfy the constraint dictated by the chemical potential maximum value. This is exactly the BEC phenomenon discussed in the most general terms; the exact conditions for the onset of the condensation, or if they are present at all [6] , depend on the system dimensionality and on the presence and features of an external potential.

### 1.1.2 BEC for non-interacting atoms in a 3D harmonic potential

In this subsection I will describe BEC for a system of non-interacting particles confined in a 3D harmonic potential. This model is is representative of the majority of experimental situations with cold trapped atoms (with some exceptions [7]) . Taking an anisotropic trapping potential of the form

$$V(x, y, z) = \frac{m}{2}\left(\omega_x^2 x^2 + \omega_y^2 y^2 + \omega_z^2 z^2\right) \tag{1.1.8}$$

where $\omega_i$ are the harmonic trapping frequencies in different directions. The total number of atoms $N$ can be written as the sum between the condensed fraction, occupying the system

ground state $N_0$ and the thermal fraction $N_T$

$$N = N_0 + N_T \tag{1.1.9}$$

The thermal fraction $N_T$ can be calculated from (1.1.5) in the thermodynamic limit, approximating the harmonic potential energy spectrum as a continuum, and the sum as an integral. The resulting number of atoms corresponds only to the thermal fraction because the ground state occupation is not accounted for in the integral. With this approach, after some calculations [9] the condensation temperature can be obtained

$$k_B T_C = \hbar \omega_{ho} \left( \frac{N}{\zeta(3)} \right)^{\frac{1}{3}} \tag{1.1.10}$$

where $\omega_{ho} = (\omega_x \omega_y \omega_z)^{1/3}$ is the geometric average of the harmonic trapping frequencies, and $\zeta(3) \simeq 1.202$ is the Riemann Zeta function. Below the condensation temperature the condensed atoms number is

$$\frac{N_0}{N} = 1 - \left( \frac{T}{T_C} \right)^3 \tag{1.1.11}$$

## 1.2 Mean Field description of weakly interacting BEC

**The Many-Body Hamiltonian** The general Many-Body Hamiltonian for a Bose Gas, with pairwise interactions $V_{int}(\mathbf{x}, \mathbf{y})$ confined in an external potential $V_{ext}(\mathbf{x})$ is, in the real space basis

$$\begin{aligned} \hat{H} = & \int \mathsf{dx} \hat{\Psi}^\dagger(\mathbf{x}) \left( -\frac{\nabla^2}{2m} + V_{ext}(\mathbf{x}) \right) \hat{\Psi}(\mathbf{x}) + \\ & + \frac{1}{2} \int \mathsf{dxdy} \hat{\Psi}^\dagger(\mathbf{x}) \hat{\Psi}^\dagger(\mathbf{x}) V_{int}(\mathbf{x}, \mathbf{y}) \hat{\Psi}(\mathbf{x}) \hat{\Psi}(\mathbf{x}) \end{aligned} \tag{1.2.1}$$

where $\hat{\Psi}(\mathbf{x}), \hat{\Psi}^\dagger(\mathbf{x})$ are the boson field operators that destroy (create) an atom in $\mathbf{x}$ position, satisfying the canonical commutation relations at equal time

$$\left[ \hat{\Psi}(\mathbf{x}), \hat{\Psi}^\dagger(\mathbf{y}) \right] = \delta(\mathbf{x} - \mathbf{y}) \tag{1.2.2}$$

and

$$\left[\hat{\Psi}\left(\mathbf{x}\right),\hat{\Psi}\left(\mathbf{y}\right)\right]=\left[\hat{\Psi}^{\dagger}\left(\mathbf{x}\right),\hat{\Psi}^{\dagger}\left(\mathbf{y}\right)\right]=0 \tag{1.2.3}$$

For low temperature and dilute neutral gas the interaction part of the Hamiltonian can be approximated by a contact pseudopotential

$$V_{int}\left(\mathbf{x},\mathbf{y}\right)\simeq g\delta\left(\mathbf{x}-\mathbf{y}\right) \tag{1.2.4}$$

where the interaction parameter $g$ is related to the s-wave scattering length $a$

$$g=\frac{4\pi\hbar^{2}a}{m} \tag{1.2.5}$$

Then (1.2.1) becomes

$$\hat{H}=\int \mathsf{d}\mathbf{x}\hat{\Psi}^{\dagger}\left(\mathbf{x}\right)\left(-\frac{\hbar^{2}\nabla^{2}}{2m}+V_{DW}\left(\mathbf{x}\right)\right)\hat{\Psi}\left(\mathbf{x}\right)+\frac{g}{2}\int \mathsf{d}\mathbf{x}\hat{\Psi}^{\dagger}\left(\mathbf{x}\right)\hat{\Psi}^{\dagger}\left(\mathbf{x}\right)\hat{\Psi}\left(\mathbf{x}\right)\hat{\Psi}\left(\mathbf{x}\right) \tag{1.2.6}$$

**Mean Field approximation and Gross-Pitaevskii Equation** In general, the field operators can be expanded in the single atom state basis

$$\hat{\Psi}\left(\mathbf{x}\right)=\sum_{i}\hat{a}_{i}\phi_{i}\left(\mathbf{x}\right) \tag{1.2.7}$$

where $\phi_{i}\left(\mathbf{x}\right)$ is the wavefunction of a particle in the $i$ state and $\hat{a}_{i}$ is the corresponding bosonic annihilation operator. In a Bose-Einstein condensate a finite fraction of the total atom number occupies the system ground state, below a non-zero critical temperature. In this condition, for a very large atom number (ideally in the thermodynamic limit), single atom fluctuation in the condensate are negligible and the operators $\hat{a}_{0}$ and $\hat{a}_{0}^{\dagger}$ can be approximated as complex numbers.

$$\hat{a}_{0}=\hat{a}_{0}^{\dagger}=\sqrt{N_{0}} \tag{1.2.8}$$

the ground state contribution in (1.2.7) can be explicitly separated from the sum, and generalizing this prescription for time-dependent configurations we obtain

$$\hat{\Psi}(\mathbf{x},t) = \Phi_0(\mathbf{x},t) + \hat{\psi}(\mathbf{x},t) \tag{1.2.9}$$

with $\Phi_0(\mathbf{x},t) = \sqrt{N_0}\phi_0(\mathbf{x},t)$ is a complex value function, defined as the expectation value of the field operator, that is a classical field with a defined phase and whose modulus fixes the condensate density $n_0(\mathbf{x},t) = |\Phi_0(\mathbf{x},t)|^2$. The zeroth order approximation for the Many-Body Hamiltonian (1.2.6) consists in neglecting the fluctuations $\hat{\Psi}(\mathbf{x},t) \simeq \Phi(\mathbf{x},t)$, obtaining the energy functional

$$E[\Phi(\mathbf{x},t)] = \int \mathsf{d}\mathbf{x} \left[\frac{\hbar^2}{2m}|\nabla\Phi_0(\mathbf{x},t)|^2 + V_{ext}(\mathbf{x})|\Phi_0(\mathbf{x},t)|^2 + \frac{g}{2}|\Phi_0(\mathbf{x},t)|^4\right] \tag{1.2.10}$$

from which, requiring the stationarity with the variational condition

$$i\hbar\frac{\partial}{\partial t}\Phi_0(\mathbf{x},t) = \frac{\delta E[\Phi_0(\mathbf{x},t)]}{\delta\Phi_0^\star(\mathbf{x},t)} \tag{1.2.11}$$

the time-dependent Gross-Pitaevskii equation (GPE) is obtained

$$i\hbar\frac{\partial}{\partial t}\Phi_0(\mathbf{x},t) = \left(-\frac{\hbar^2}{2m}\nabla^2 + V_{ext}(\mathbf{x}) + g|\Phi_0(\mathbf{x},t)|^2\right)\Phi_0(\mathbf{x},t) \tag{1.2.12}$$

that is an equation for the order parameter. For the (stationary) ground state of the condensate, with the substitution $\Phi_0(\mathbf{x},t) = e^{-i\frac{\mu}{\hbar}t}\Phi_0(\mathbf{x})$ the GPE takes the form of a nonlinear Schrödinger equation for the chemical potential

$$\mu\Phi_0(\mathbf{x}) = \left(-\frac{\hbar^2}{2m}\nabla^2 + V_{ext}(\mathbf{x}) + g|\Phi_0(\mathbf{x})|^2\right)\Phi_0(\mathbf{x}) \tag{1.2.13}$$

The validity of the GPE is restricted to temperatures much below the condensation temperature, for which the thermal fraction of atoms is negligible. It is also the zeroth order approximation on which the effects of fluctuations in the order parameter are calculated with a perturbative approach, but pursuing further this topic is outside the scope of this Thesis.

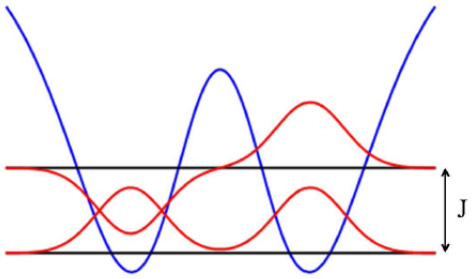


Figure 1.3.1: The first two energy eigenstates of the double well potential for non-interacting particles. In the two-mode approximation these two levels are often referred to as "symmetric" (the ground) and "antisymmetric" (the first excited) eigenstate for their spatial symmetry.

## 1.3 Bose-Einstein Condensate in a double well potential

**Two Mode approximation** The double well potential system in the context of BECs is usually discussed in the simplifying two-mode approximation. Solving the eigenstates problem for single particles results that the energy difference between the first two states, defined as the tunneling energy (Figure 1.3.1) diminishes exponentially with the barrier height, while the difference between the ground state and the higher excited levels remains of the order of the energy level separation of the corresponding harmonic trap. For this reason if the energy scales of the system (including, for example, thermal energy) are much lower than the harmonic trap energy separation the system can be described effectively as a two-level system, neglecting all the higher states. To further reinforce this assumption without having to calculate the exact energy values one can consider the two physical limits of this potential. In the limit of an infinite barrier the system consists in two separated harmonic potential whose energy levels are the harmonic oscillator levels with double degeneracy. In this limit the first two energy levels are exactly degenerate (zero tunneling energy) and the energy separation between these two levels and the next excited is exactly $\hbar\omega_{HO}$. In the opposite limit of zero height central barrier the energy difference between the ground state and first excited level equals the energy difference between the second and third excited (since the system degenerates to a single harmonic well), and the two-mode approximation cannot be

justified. Between these two limits, depending on the energy scale of the system, there is a minimum value of the central barrier height from which the basic assumption is justified.

The next conceptual step is to infer that for weakly interacting atoms this approximation is still valid. One can think to turn on repulsive interactions with an s-wave scattering length tendent to zero, and ramp it up; there will be a point where the interaction energy contribution in the first two levels is so high that a macroscopic occupation of the higher levels is favorable, breaking the two mode approximation. On the contrary the approximation can be retained. Another subtle point is that in presence of interactions the definition of the first excited state is not so straightforward, since the wavefunction of the single-particle excited state depends on the population of all states. One possibility consists in defining the spatial wavefunction of each of the two states as the solution of a stationary GPE

$$\mu_{g,e}\phi_{g,e}\left(\mathbf{x}\right)=\left(-\frac{\hbar^2}{2m}\nabla^2+V\left(\mathbf{x}\right)+\frac{g}{2}N\left|\phi_{g,e}\left(\mathbf{x}\right)\right|^2\right)\phi_{g,e}\left(\mathbf{x}\right) \tag{1.3.1}$$

discriminating the ground and first excited states by their symmetry properties. Introducing the two-mode approximation with the ansatz on the field operators

$$\hat{\Psi}\left(\mathbf{x}\right)=\hat{a}_g\phi_g\left(\mathbf{x}\right)+\hat{a}_e\phi_e\left(\mathbf{x}\right) \tag{1.3.2}$$

and the normalization condition

$$\int \mathsf{d}\mathbf{x}\ \left|\phi_{g,e}\right|^2=1 \tag{1.3.3}$$

**Bose-Hubbard Hamiltonian** A more straightforward, although equivalent, basis to discuss this problem is the left-right localized modes basis. Introducing the creation/annihilation operators in the left-right localized states basis

$$\hat{a}_g=\frac{\hat{a}_l+\hat{a}_r}{\sqrt{2}}\qquad \hat{a}_e=\frac{\hat{a}_l-\hat{a}_r}{\sqrt{2}} \tag{1.3.4}$$

in the field operator definition in the two mode approximation (1.3.2)

$$\hat{\Psi}\left(\mathbf{x}\right)=\left(\frac{\phi_g\left(\mathbf{x}\right)+\phi_e\left(\mathbf{x}\right)}{\sqrt{2}}\right)\hat{a}_l+\left(\frac{\phi_g\left(\mathbf{x}\right)-\phi_e\left(\mathbf{x}\right)}{\sqrt{2}}\right)\hat{a}_r \tag{1.3.5}$$

Substituting this field operator definition in the Many-Body Hamiltonian (1.2.6), discarding terms that depend only on the total number of atoms (that we assume conserved) and carrying the necessary algebra

$$\hat{H}_{2M} = \frac{E_C}{8}\left(\hat{a}_l^\dagger \hat{a}_l - \hat{a}_r^\dagger \hat{a}_r\right)^2 - \frac{E_J}{N}\left(\hat{a}_l^\dagger \hat{a}_r + \hat{a}_r^\dagger \hat{a}_l\right) + \delta E\left(\hat{a}_l^\dagger \hat{a}_r + \hat{a}_r^\dagger \hat{a}_l\right)^2 \tag{1.3.6}$$

defining

$$\mathcal{K}_{i,j} = \frac{g}{2}\int \mathbf{dx}\, |\phi_i|^2 \, |\phi_j|^2 \tag{1.3.7}$$

$$E_c = 8\mathcal{K}_{g,e} \tag{1.3.8}$$

$$E_J = \frac{N\left(\mu_e - \mu_g\right)}{2} - \frac{N\left(N+1\right)}{2}\left(\mathcal{K}_{e,e} - \mathcal{K}_{g,g}\right) \tag{1.3.9}$$

$$\delta E = \frac{\mathcal{K}_{e,e} + \mathcal{K}_{g,g} - 2\mathcal{K}_{g,e}}{4} \tag{1.3.10}$$

The three terms in (1.3.6) can be straightforwardly interpreted as the interaction energy contribution, the tunneling of atoms between the two wells, and two-particles additional processes. This last term can be neglected if it is small enough compared to the others or in the more stringent approximation $\mathcal{K}_{e,e} = \mathcal{K}_{g,g} = \mathcal{K}_{g,e}$ where it is exactly zero [10]. In both cases the Hamiltonian can be written, formally introducing angular momentum operators

$$\hat{J}_z = \frac{1}{2}\left(\hat{a}_l^\dagger \hat{a}_l - \hat{a}_r^\dagger \hat{a}_r\right) \tag{1.3.11}$$

$$\hat{J}_x = \frac{1}{2}\left(\hat{a}_l^\dagger \hat{a}_r + \hat{a}_r^\dagger \hat{a}_l\right) \tag{1.3.12}$$

$$\hat{J}_y = \frac{1}{2i}\left(\hat{a}_l^\dagger \hat{a}_r - \hat{a}_r^\dagger \hat{a}_l\right) \tag{1.3.13}$$

that satisfy the commutation relations expected for angular momentum operators

$$\left[\hat{J}_i, \hat{J}_j\right] = i\epsilon_{ijk}\hat{J}_k \tag{1.3.14}$$

using the commutation relations

$$\left[\hat{a}_i, \hat{a}_j^\dagger\right] = \delta_{i,j} \tag{1.3.15}$$

$$[\hat{a}_i, \hat{a}_j] = 0 \tag{1.3.16}$$

$$\left[\hat{a}_i^\dagger, \hat{a}_j^\dagger\right] = 0 \tag{1.3.17}$$

as the Bose-Hubbard Hamiltonian for the two-well system

$$\hat{H}_{2M} = \frac{E_C}{2}\hat{J}_z{}^2 - \frac{2E_J}{N}\hat{J}_x \tag{1.3.18}$$

The physical interpretation of the angular momentum operator $\hat{J}_z$ is straightforward in the left-right mode basis, as the number difference operator. The $\hat{J}_x$ operator in this basis is a tunneling operator and, interestingly, corresponds to the number difference in the two mode energy eigenstate basis. The $\hat{J}_y$ component instead is tied to the condensate momentum in the double well system [11]. Choosing this formalism a coherent state can be represented as an angular momentum vector on a Bloch Sphere, allowing for a complete pictorial representation of the state of the system and its dynamics. This will be introduced in Chapter 2 to discuss the interferometric operations.

### 1.3.1 Energy spectrum of Bose-Hubbard Hamiltonian for a symmetric well.

The energy spectrum of the Bose-Hubbard Hamiltonian will be calculated in the Fock states basis

$$|n\rangle = \left|\frac{N}{2} + n\right\rangle_l \left|\frac{N}{2} - n\right\rangle_r \tag{1.3.19}$$

where $n$ is the population imbalance. Notice that $|n\rangle$ are eigenstates of the $\hat{J}_z$ operator, and zero tunneling Hamiltonian would be already diagonalized in this basis. The effect of the full

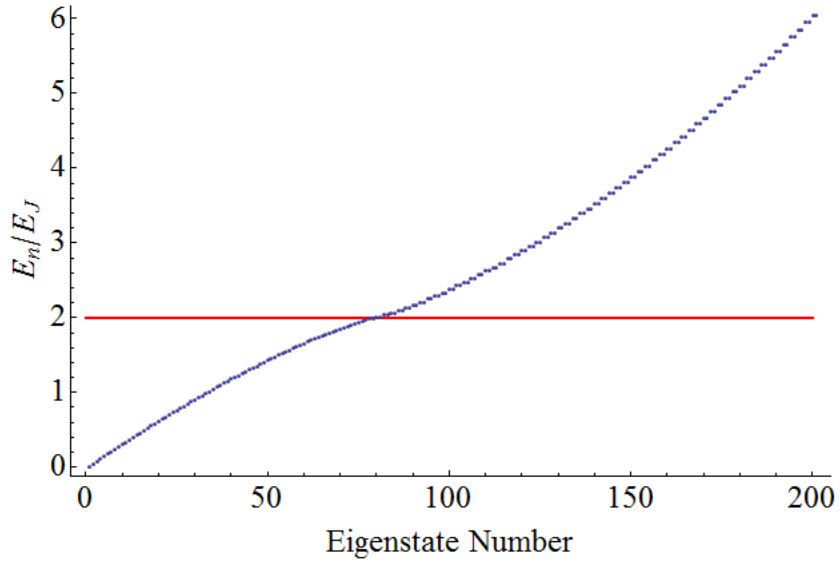


Figure 1.3.2: The energy spectrum for a system of 200 atoms. The interactions and tunneling parameters were chosen to show all the relevant features of the spectrum. The spectrum is linear for low interactions, while for $E_c > 2E_J$ it shows a quadratic behavior and the levels are twofold degenerate.

symmetric Hamiltonian on the generic vector belonging to this space can be expressed

$$\hat{H}\sum_n c_n |n\rangle = \sum_n \left\{ \frac{E_c}{2} c_n n^2 - \frac{E_J}{N}\left[ c_{n-1}\sqrt{\left(\frac{N}{2}+n\right)\left(\frac{N}{2}-n+1\right)} + \right.\right. \\ \left.\left. + \; c_{n+1}\sqrt{\left(\frac{N}{2}+n+1\right)\left(\frac{N}{2}-n\right)}\right]\right\} |n\rangle \quad (1.3.20)$$

and the Hamiltonian is represented as a $(2N+1)\,\mathrm{x}\,(2N+1)$ matrix

$$\begin{pmatrix} \frac{E_C}{2}\left(\frac{N}{2}\right)^2 & \frac{E_J}{N}\sqrt{N} & 0 & 0 & \dots \\ \frac{E_J}{N}\sqrt{N} & \frac{E_C}{2}\left(\frac{N}{2}-1\right)^2 & \frac{E_J}{N}\sqrt{2\,(N-1)} & 0 & \dots \\ 0 & \frac{E_J}{N}\sqrt{2\,(N-1)} & \frac{E_C}{2}\left(\frac{N}{2}-2\right)^2 & \frac{E_J}{N}\sqrt{3\,(N-2)} & \dots \\ 0 & 0 & \frac{E_J}{N}\sqrt{3\,(N-2)} & \frac{E_C}{2}\left(\frac{N}{2}-3\right)^2 & \dots \\ \dots & \dots & \dots & \dots & \dots \end{pmatrix} \quad (1.3.21)$$

corresponding to matrix elements

$$\langle i|\,\hat{H}\,|j\rangle = \frac{E_C}{2}\left(\frac{N}{2}-j+1\right)^2\delta_{i,j}+ \\ +\frac{E_J}{N}\left[\sqrt{(N-j)\,(j+1)}\delta_{i+1,j}+\sqrt{(N-j+1)\,(j)}\delta_{i-1,j}\right] \tag{1.3.22}$$

Solving the eigenvalue problem for the matrix (1.3.21) the energy spectrum and the correspondent eigenvalues can be computed for a typical experimental atom number. The computed spectrum, using $E_J$ as the energy unit, for different values of $E_C/E_J$ is shown in Figure 1.3.2.

**Analytical approximation** Also an analytical approximation for the eigenstates of the Hamiltonian (1.3.21) can be obtained for the lowest energy states following the approach in [10]. In case the coefficients $\mathcal{K}$ are equal, assuming $c_{n+1}-c_n$ to be small and expanding the coefficients in series (treating $n$ as a continuous variable and writing the corresponding coefficients as $C(n)$) we get the equation

$$\left[-\frac{E_J}{2}\frac{\mathsf{d}^2}{\mathsf{d}n^2}+\left(\frac{E_J}{2N^2}+4\mathcal{K}\right)n^2\right]C\,(n)=\epsilon C\,(n) \tag{1.3.23}$$

That is the Schrödinger equation for an Harmonic oscillator with frequency

$$\omega_p=\frac{1}{\hbar}\sqrt{E_J\left(E_c+\frac{4E_J}{N^2}\right)} \tag{1.3.24}$$

which is referred as the "plasma frequency", and approximates the linear energy behavior for the first part of the spectrum. In Figure 1.3.3 the energy interval between each eigenstate and the subsequent is compared to the plasma frequency.

### 1.3.2 Coherence

The tunneling operator $\hat{J}_x$ is also tied to the coherence of the system. The coherence operator can be defined

$$\hat{\alpha}_+=\frac{2}{N}\hat{J}_x \tag{1.3.25}$$

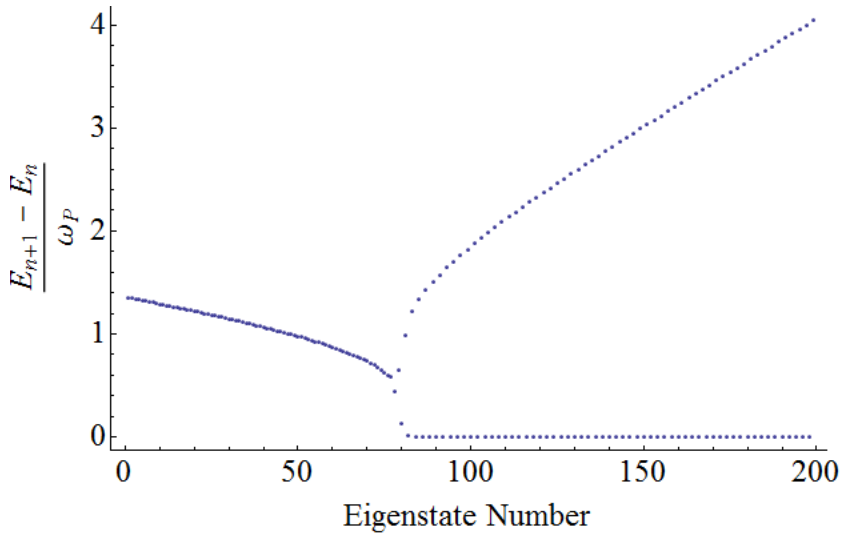


Figure 1.3.3: Energy difference between near eigenstates of the whole spectrum in units of of $\hbar\omega_p$, for the same parameters of the previous figure.

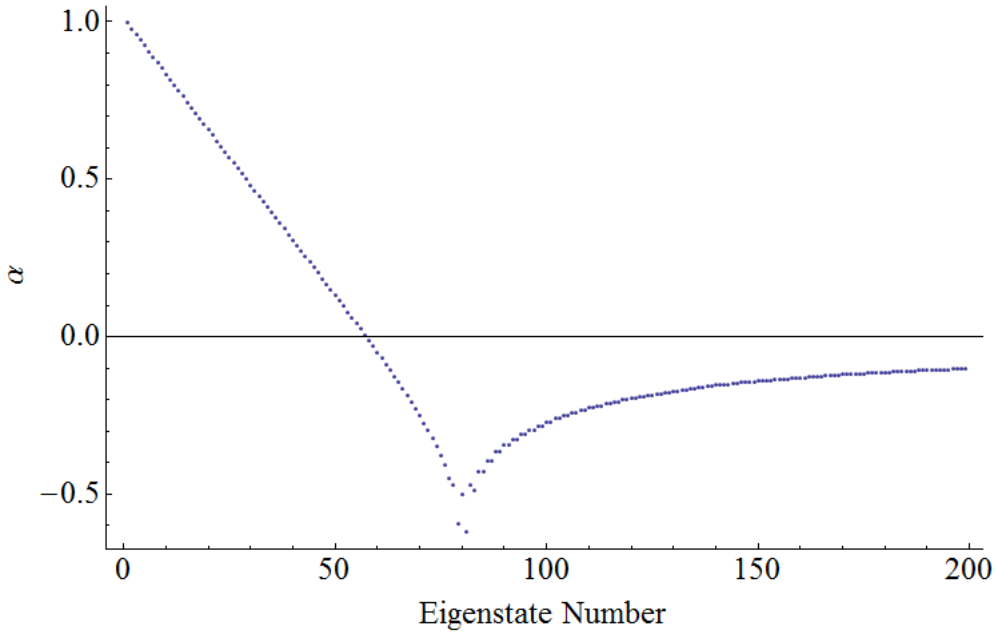


Figure 1.3.4: The coherence of all the spectrum eigenstates for 200 atoms.

and the average $\langle \hat{\alpha}_+ \rangle$ is referred to as "coherence" of the state. This results from quantitative definition of first-order coherence as the renormalized first-order spatial correlation function of the field

$$\alpha = g^{(1)}(\mathbf{x}', \mathbf{x}) = \frac{\left\langle \hat{\Psi}^\dagger(\mathbf{x}')\, \hat{\Psi}(\mathbf{x}) \right\rangle}{\sqrt{\left\langle \hat{\Psi}^\dagger(\mathbf{x}')\, \hat{\Psi}(\mathbf{x}') \right\rangle \left\langle \hat{\Psi}^\dagger(\mathbf{x})\, \hat{\Psi}(\mathbf{x}) \right\rangle}} \tag{1.3.26}$$

where $\mathbf{x}$ and $\mathbf{x}'$ are points located respectively in the left and in the right well, then re-writing the field operators in the two-mode left-right eigenfunctions basis it results that if the overlap region is negligible $g^{(1)}(\mathbf{x}', \mathbf{x})$ does not depend on the coordinates [12]

$$\alpha = \frac{\left\langle \hat{a}_l^\dagger \hat{a}_r + \hat{a}_r^\dagger \hat{a}_l \right\rangle}{N} = \frac{\left\langle \hat{a}_g^\dagger \hat{a}_g - \hat{a}_e^\dagger \hat{a}_e \right\rangle}{N} = \left\langle \frac{2}{N} \hat{J}_x \right\rangle \tag{1.3.27}$$

This quantity is experimentally related to the fluctuations of the relative phase between the two modes. In Figure 1.3.4 the coherence of each eigenstate of the system is plotted. The ground state shows the higher degree of coherence. After reaching zero it's absolute value increases again (negative coherence indicates a population inversion between the two states) and slowly decreases again.

A classical approximation for the coherence factor can be obtained substituting for the operators $\hat{a}$ and $\hat{a}^\dagger$ in the definition of $\hat{J}_x$

$$\hat{a}_j \to \sqrt{n_j} e^{i\varphi_j} \qquad j = l, r \tag{1.3.28}$$

obtaining

$$\alpha_{cl} = \left\langle \sqrt{1 - \frac{n^2}{N^2}} Cos(\varphi) \right\rangle \tag{1.3.29}$$

where $n = n_l - n_r$ and $\varphi = \varphi_l - \varphi_r$. For small average population imbalances this is well approximated as

$$\alpha_{cl} = \langle Cos(\varphi) \rangle \tag{1.3.30}$$

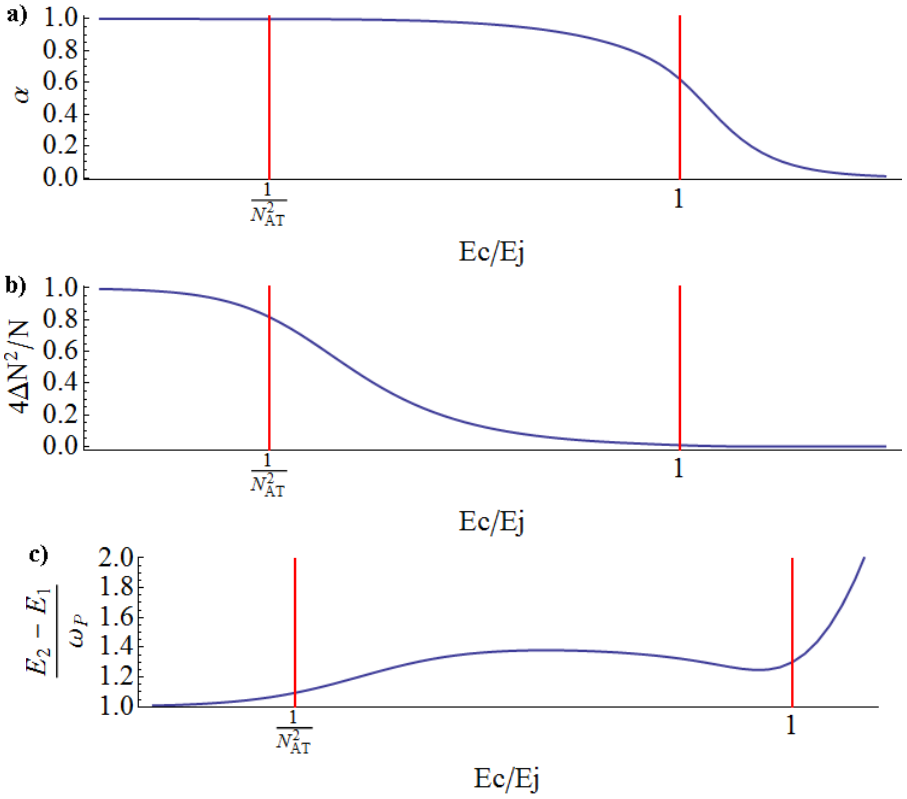


Figure 1.3.5: Coherence **(a)** and atom number fluctuation **(b)** in units of $N/2$ of the ground eigenstate in function of the parameter $E_c/E_J$ numerically computed diagonalizing the system Hamiltonian (1.3.21) for N atoms. The red lines represent the boundaries between Rabi, Josephson and Fock regimes. As we can see from the direct comparison, Rabi (non-interacting) regime is characterized by high coherence and Poissonian atom fluctuations, Fock (dominant interactions) regime shows both very low atom number fluctuations and coherence. In the Josephson regime the system coherence is still high and number fluctuations are reduced compared to Rabi regime. **c)** Energy difference between the ground and first excited eigenstate in units of $\hbar\omega_p$ for the three interacting regimes. As we can see the plasma frequency is still a good approximation for the energy level difference until interactions become dominant.

### 1.3.3 Ground state properties and regimes

In Figure 1.3.5 are shown the calculated number fluctuations and coherence of the ground eigenstate in function of the ratio between interaction and tunneling energy $E_c/E_J$. Since

these results do not include the thermal occupation of the states, they can be taken as a description of the properties of the system only at zero temperature. Three regimes are identified.

**Rabi:** $E_c/E_j \ll N^{-2}$ The Rabi regime corresponds to the non-interacting limit, where the atom number fluctuations follow a Poissonian statistics and the coherence of the system is high.

**Josephson:** $N^{-2} \ll E_c/E_j \ll 1$ In the Josephson regime the coherence of the system is still reasonably high, while the number fluctuations decrease.

**Fock :**$1 \ll E_c/E_j$ In the Fock regime interactions are dominant, the number fluctuations are heavily suppressed, while the coherence of the system vanishes and the phase is undefined.

### 1.3.4 Temperature and Interactions

To extend the treatment of the system coherence carried in the previous subsection to the case of $T \neq 0$ the coherence factor for a thermal occupation of Fock states has been calculated for different temperatures and interaction parameter values (Figure 1.3.6). The first result is that when taken independently both temperature and interactions decrease the system coherence. The interplay between these two quantities however has interesting features. While for zero temperature the coherence decreases crossing the Josephson regime to the Fock regime, for nonzero temperature the (lower) coherence exhibits a maximum in the Josephson regime before reducing in the Fock regime, where it becomes totally irrespective of temperature for high enough interaction values. Even the opposite is true, for nonzero interactions the system coherence shows increased stability against thermal fluctuations, although the maximum reachable coherence value is reduced. This stabilizing effect is due to the increase of the excitation energies, approximated with the Plasma Frequency (1.3.24) up to the Josephson regime and for the first part of the spectrum, and the consequent reduction of the ratio between excitation energies and the thermal energy scale of the system ($\hbar\omega_p/k_BT$)

Beyond the fundamental physical interest this behavior has two interesting consequences for interferometric experiments with cold atoms, where the interatomic interactions can be

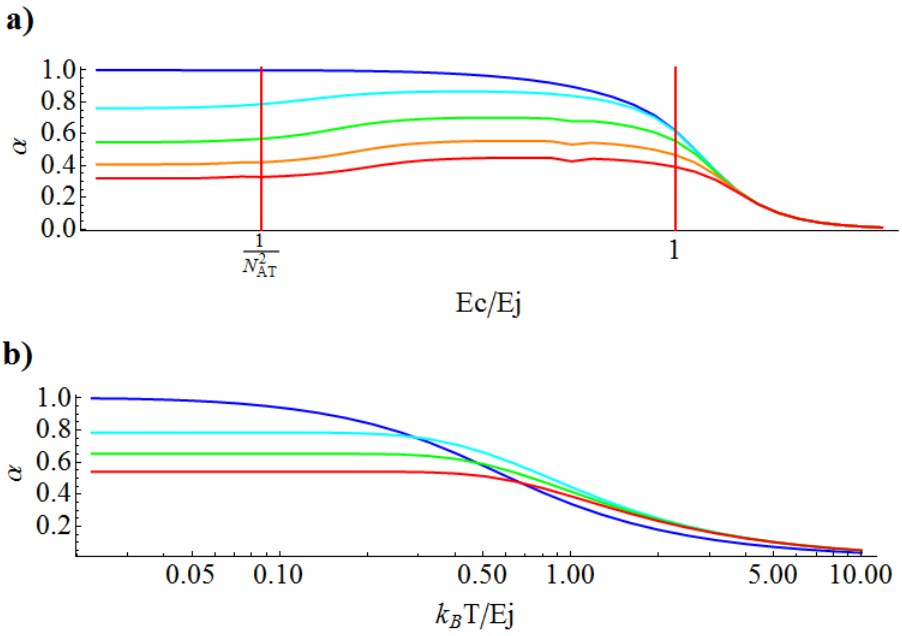


Figure 1.3.6: **a)** Coherence as a function of $E_c/E_J$ for different temperatures, in logarithmic scale. Remarkably for nonzero temperature in the Josephson Regime the presence of interactions increases the coherence. The numerical calculation has been carried for $N = 100$ atoms and temperatures $k_BT \ll E_J$ (Blue), $k_BT = 1/4 E_J$ (Cyan), $1/2 E_J$ (Green), $3/4 E_J$ (Orange), $E_J$ (Red) **b)** Coherence as a function of temperature for different values of interactions. $N = 100$, $E_c \ll E_J$ (Blue), $E_c = 1/2 E_J$ (Cyan), $E_J$ (Green), $3/2 E_J$ (Red)

tuned exploiting Feshbach resonances (see Subsection 3.2.1): first, particular care must be adopted against thermal excitations in the non-interacting case; second, correctly modeling the experimental system opens the interesting possibility of finding the optimal interplay between involved parameters, to enhance its performance.

### 1.3.5 Well imbalance

So far we considered a perfectly symmetric double well confining potential. However, the energy imbalance between the two wells is an important parameter. It is unlikely that in real experimental realization of such systems noise or drifts in this parameter could be completely canceled; more importantly, in interferometric applications, it represents the effect of the

external perturbation that is to be measured, and for this reason it must be addressed. In our case the imbalance is set shifting the relative position of two optical lattices (see Subsection 3.3.1)

$$V(x) = V_2 Cos^2\left(2k_L x\right) - V_1 Cos^2\left(k_L\left(x + \Delta x\right)\right) \tag{1.3.31}$$

approximating the main well as an Harmonic potential it is straightforward to find

$$\frac{1}{2} m\omega^2 \left(x + \Delta x\right)^2 = V_{HO}\left(x\right) + m\omega^2 x\, \Delta x + const. \tag{1.3.32}$$

so in these conditions the effect of the shift can be written as the symmetric double well potential plus an additional linear gradient

$$V\left(x\right) = V_{DW}\left(x\right) + \left(m\omega^2 \Delta x\right) x \tag{1.3.33}$$

The effect of this gradient is to introduce an additional energy shift between the two localized spatial modes of the system; substituting (1.3.33) in place of the symmetric potential in (1.2.6) the Bose-Hubbard Hamiltonian comprising the energy shift term is

$$\hat{H}_{2M} = \frac{E_C}{2} \hat{J}_z^2 - \frac{2E_J}{N} \hat{J}_x + \delta \hat{J}_z \tag{1.3.34}$$

with

$$\delta = 2m\omega^2 \int \mathbf{dx} \phi_g^\star x \phi_e \tag{1.3.35}$$

This additional term, if present, favors the occupation of a single spatial mode. Ramping up the central barrier with a sufficient imbalance allows to prepare the condensate in a single well. The dynamical effect of this term instead is to induce a relative phase evolution between the two spatial modes.

### 1.3.6 Matter-Wave interference as direct measurement of relative phase.

The possibility to observe the interference fringes between two matter wavepackets overlapped after free expansion allows to directly measure their phase difference [21, 22]. The

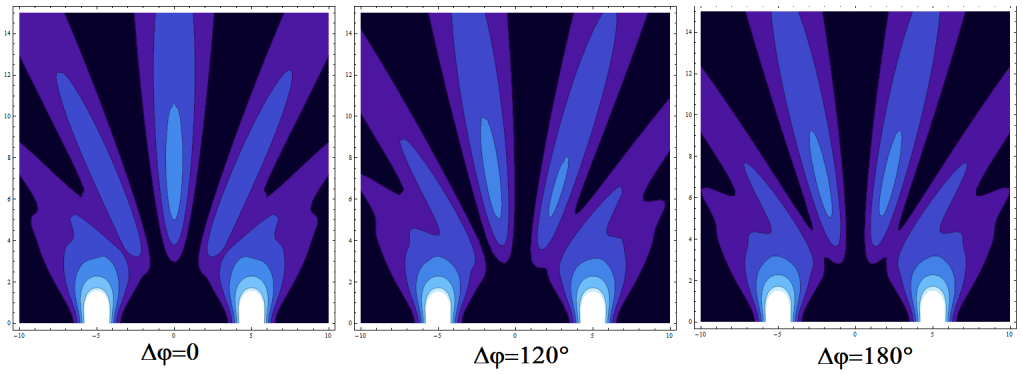


Figure 1.3.7: Expansion simulation of two localized Gaussian wavepackets for different values of the relative phase $\Delta\varphi$. Real space is represented on x-axis and time on y axis, both in arbitrary units. After some time the fringes maintain an asymptotic profile. White corresponds to the maximum probability density, darker blue for the minimum. From the comparison emerges that the fringes position depends on the relative phase.

phase depends on the position of the fringes relative to a Gaussian envelope function. To represent this situation one possibility is to compute the condensates expansion in real space, and after the complete overlap of the two expanding modes we obtain the asymptotic distribution fringes (See Figure 1.3.7) and the optimal experimental expansion time. If we are not interested in the whole dynamics, but instead only to the asymptotic distribution a possible shortcut is to exploit the fact that for long enough expansion times (in the ballistic regime) the observed space distribution corresponds to the initial momentum distribution.

$$\langle \hat{\rho}\left(p\right)\rangle = \left\langle \hat{\Psi}^{\dagger}\left(p\right)\hat{\Psi}\left(p\right)\right\rangle \tag{1.3.36}$$

To compute the Fourier transform of the field operators one can start in a simple situation, following from the symmetry of the potential, of two equal Gaussian modes whose peaks are separated by the distance $d$

$$\hat{\Psi}\left(x\right) = \hat{a}_l\phi\left(x+\frac{d}{2}\right) + \hat{a}_r\phi\left(x-\frac{d}{2}\right) \tag{1.3.37}$$

In momentum space we obtain

$$\hat{\Psi}(p) = \hat{a}_l \phi(p) e^{i\frac{pd}{2}} + \hat{a}_r \phi(p) e^{-i\frac{pd}{2}} \tag{1.3.38}$$

and the momentum density distribution (1.3.36)

$$\langle \hat{\rho}(p) \rangle = |\phi(p)|^2 \left( N + 2 \left\langle \hat{J}_x \right\rangle Cos(pd) + 2 \left\langle \hat{J}_y \right\rangle Sin(pd) \right) \tag{1.3.39}$$

Defining the phase origin for $\left\langle \hat{J}_y \right\rangle = 0$ and collecting the $N$ factor

$$\langle \hat{\rho}(p) \rangle = N |\phi(p)|^2 \left( 1 + \left\langle 2\frac{\hat{J}_x}{N} \right\rangle Cos(pd) \right) \tag{1.3.40}$$

The averaged density distribution corresponds a Gaussian overlap function on which interference fringes are superimposed and their visibility is proportional to the coherence factor $\alpha$

# Chapter 2

# Atom Interferometry with a BEC in a Double-Well potential

In this chapter I will describe the Mach-Zehnder atom interferometer operations and its parallelism with the traditional Mach-Zehnder light interferometer. In the first Section I will introduce the Bloch Sphere representation of the atomic system state, since it is a useful pictorial representation that allows to visualize in a simple and compact way both the atom number imbalance between the two wells and the relative phase of the two spatial modes, and to represent the system evolution induced by the Bose-Hubbard Hamiltonian (1.3.34). For a many particle system also the (quasi)probability distribution of the quantum state can be pictorially represented as a density plot on the sphere surface. In the second section the operation of the linear (non-interacting) Mach-Zehnder atom interferometer is described using the Bloch Sphere representation and demonstrating that for a coherent state, where all the particles of the system are prepared in the same single-particle state, the minimum uncertainty in the estimated phase value corresponds to the Shot Noise Limit, scaling with the employed number of atoms as $\Delta\varphi_{SNL} = N^{-1/2}$. In the third section the advantages of quantum-enhanced interferometry will be presented. Although interactions are a fundamental source of loss of coherence in the system, they introduce a "twisting" term in the system evolution by the means of the nonlinear term of the BH Hamiltonian. This term introduces quantum correlations between the atoms composing the system, allowing us to reduce the

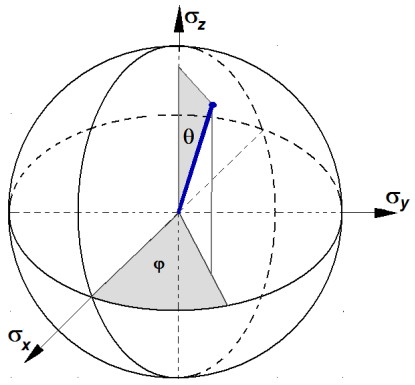


Figure 2.1.1: In the Bloch Sphere representation the variables $\theta$ and $\varphi$ representing the relative probability of the two states and their relative phase are both represented.

phase quantum fluctuations and consequently reduce the phase estimation uncertainty below the SNL. Then I will introduce in a qualitative manner three "maximally entangled states" that are planned to be studied in the future of the experimental activity I am reporting, and that would allow the best achievable scaling of the phase uncertainty with the atom number, $\Delta\varphi \propto N^{-1}$. The possible methods to obtain them and their intrinsic limitations will be discussed.

## 2.1 Spin Formalism and Bloch Sphere representation

A particularly useful representation of the coherent states in the two level many body system can be achieved in the spin formalism, representing the state on the Bloch sphere. This allows to have a complete pictorial representation of the system including both the relative phase of the two modes and the population imbalance

### 2.1.1 Single particle

The single particle representation in the Bloch Sphere is elementary and would not be required in this discussion, nevertheless it allows to discuss the relevant features of the representation in a simple model, and an easier extension to the case of a coherent state of $N$ independent

particles. The quantum state of a single particle in a two level system is

$$|\psi\rangle = Cos(\theta)\,|a\rangle + Sin(\theta)\,e^{i\varphi}\,|b\rangle \tag{2.1.1}$$

with the variable $\theta$ referred to the relative probability of occupation of the two states, and $\varphi$ to the relative phase between the two states. This problem's Hilbert space is bidimensional, and can be remapped to a point on the surface of a sphere (the Bloch Sphere). The state vector, pointing from the center to the surface of the sphere is a $s = 1/2$ spin vector whose third component eigenstates correspond to the system eigenstates in the chosen reference frame

$$|a\rangle = \begin{pmatrix} 0 \\ 1 \end{pmatrix} \qquad |b\rangle = \begin{pmatrix} 1 \\ 0 \end{pmatrix} \tag{2.1.2}$$

In the Bloch sphere the variables $\theta$ and $\varphi$ completely defining the state are represented at the same time (Figure 2.1.1) . This important advantage is retained in the dynamical description of the system. A general Hamiltonian in the two-dimensional Hilbert space

$$\hat{H} = E_a\,|a\rangle\langle a| + E_b\,|b\rangle\langle b| + \Omega\,|a\rangle\langle b| + \Omega^{\star}\,|b\rangle\langle a| \tag{2.1.3}$$

can be written as a superposition of identity matrix and the three Pauli matrices

$$I = \begin{pmatrix} 1 & 0 \\ 0 & 1 \end{pmatrix} \quad \hat{\sigma}_z = \begin{pmatrix} 1 & 0 \\ 0 & -1 \end{pmatrix} \quad \hat{\sigma}_x = \begin{pmatrix} 0 & 1 \\ 1 & 0 \end{pmatrix} \quad \hat{\sigma}_y = \begin{pmatrix} 0 & -i \\ i & 0 \end{pmatrix} \tag{2.1.4}$$

with the result, redefining the energy origin, defining energy difference $\Delta = E_b - E_a$ and taking a real coupling for simplicity

$$\hat{H} = \Delta\hat{\sigma}_z + \frac{\Omega}{2}\hat{\sigma}_x \tag{2.1.5}$$

The corresponding evolution operator

$$\hat{U}(t) = e^{-\frac{i}{\hbar}\left(\Delta\hat{\sigma}_z + \frac{\Omega}{2}\hat{\sigma}_x\right)t} \tag{2.1.6}$$

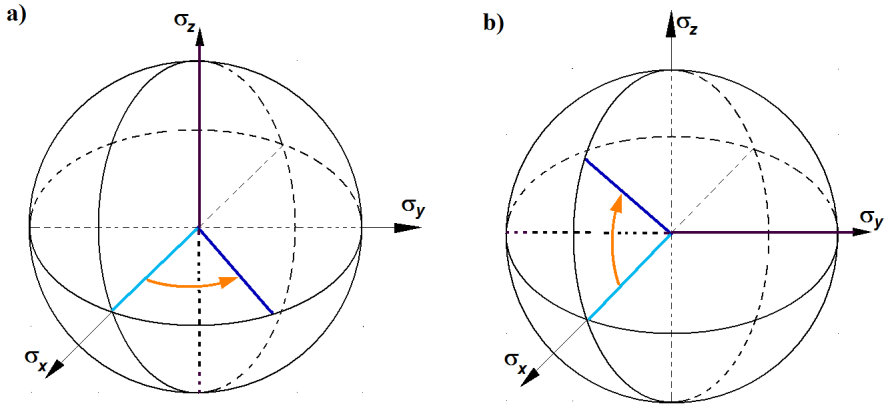


Figure 2.1.2: Evolution induced on the representative spin by an energy difference Hamiltonian term proportional to $\hat{\sigma}_z$ **(a)** and by a coupling term proportional to $\hat{\sigma}_y$ **(b)**

In the spin representation an evolution operator induces a precession of the representative spin around the axis identified by the $\hat{\boldsymbol{\sigma}}$ components. As shown in Figure 2.1.2, an energy difference term between the two modes, proportional to the $\sigma_z$ component of the Hamiltonian induces a precession of the representative vector around the corresponding axis, correctly predicting on the Bloch Sphere the temporal evolution of the phase difference between the two states. In the same way, coupling terms corresponding to a superposition between $\sigma_x$ and $\sigma_y$ components correspond to oscillation in the relative occupation probability (Rabi oscillation).

**Quantum fluctuations** The different components of the spin operator are conjugate variables, and their commutation relations are $[\hat{\sigma}_i, \hat{\sigma_j}] = i\epsilon_{ijk}\hat{\sigma}_k$. For this reason a minimum uncertainty relation is to be expected. Taking a spin vector in one direction, and computing the variance of the spin observables in orthogonal directions the result is

$$\left\langle (\hat{\sigma}_\perp - \langle \hat{\sigma}_\perp \rangle)^2 \right\rangle = (\Delta \hat{\sigma}_\perp)^2 = \frac{1}{4} \tag{2.1.7}$$

### 2.1.2 Extension to many-particle coherent states

Now I will discuss the extension of the Bloch Sphere representation to the case of many bosonic atoms. This extension is not straightforward: the tensorial product of the Hilbert spaces of $N$ representative spins is $2^N$, and the most general $N$-particle state cannot be represented on a spherical surface. More formally we can define a collective spin operator

$$\hat{J} = \frac{1}{2}\sum_{i=1}^{N}\hat{\sigma}_i \tag{2.1.8}$$

whose length is

$$\left\langle \hat{J}^2 \right\rangle^{1/2} = \sqrt{J\left(J+1\right)} \leq \frac{N}{2} \tag{2.1.9}$$

A state of maximal polarization corresponds to have the maximum value of the collective spin length. The Hilbert space dimensionality of the system reduces to $(N+1)$ and a suitable basis to describe the system is the symmetric Dicke States basis $|J,m\rangle$ that has a 1:1 correspondence with the Fock States basis $\left|\frac{N}{2}+n\right\rangle_l \left|\frac{N}{2}-n\right\rangle_r$. A coherent spin state is obtained preparing all the $N$ particles in the same single particle state.

$$|\theta,\varphi\rangle \propto \left[Cos\left(\frac{\theta}{2}\right)\hat{a}_a^\dagger + Sin\left(\frac{\theta}{2}\right)e^{i\varphi}\hat{a}_b^\dagger\right]^N |vac\rangle \tag{2.1.10}$$

corresponding, in the spin representation, to have all single particle spins pointing in the same direction; the collective spin vector has the maximal length, that can be approximated to $J \simeq N/2$ for a sufficient number of atoms. This state can be represented on a generalized Bloch Sphere of radius $J$. The system observables, including the Hamiltonian, can be written as a sum of total spin operators with the substitutions (1.3.11,1.3.12,1.3.13) where $\epsilon_{ijk}$ is the Levi-Civita symbol. The coherent state (2.1.10) represented in the Fock states basis

$$|\theta,\varphi\rangle = \sum_{n=-\frac{N}{2}}^{\frac{N}{2}} c_m\left(\theta\right)e^{-i\left(\frac{N}{2}+n\right)\varphi}|n\rangle \tag{2.1.11}$$

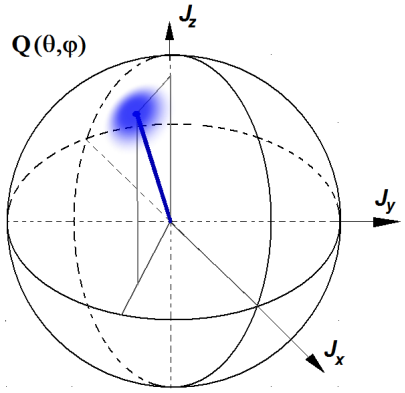


Figure 2.1.3: The representation of the quasi-probability function distribution of the state on the sphere

and the coefficients $c_m(\theta)$ follow a binomial distribution

$$c_m(\theta) = \sqrt{\frac{2J!}{(J-m)!\,(J+m)!}} Cos^{\left(\frac{N}{2}-n\right)}\left(\frac{\theta}{2}\right) Sin^{\left(\frac{N}{2}+n\right)}\left(\frac{\theta}{2}\right) \tag{2.1.12}$$

The effect of the evolution operator on the $N$ particle coherent state on the generalized Bloch Sphere is the same that we introduced for the single particle system, allowing for a simple pictorial representation of the dynamics of the system.

**Quantum fluctuations** The collective spin vector variance in orthogonal directions for a coherent spin state (2.1.10) can be taken as the sum of individual particle spin variances (2.1.7). The resulting variance is isotropic and its value

$$\left(\Delta \hat{J}_{\perp}\right)^2 = N\left(\Delta \hat{\sigma}_{\perp}\right)^2 = N/4 \tag{2.1.13}$$

corresponds to the minimum product of uncertainties derived from the commutation relations (1.3.14), taking $\mathbf{n_1}$,$\mathbf{n_2}$,$\mathbf{n_3}$ orthogonal directions

$$\left(\Delta J_{\mathbf{n_1}}\right)^2 \left(\Delta J_{\mathbf{n_2}}\right)^2 \geq \frac{1}{4}\left\langle \hat{J}_{\mathbf{n_3}} \right\rangle^2 \tag{2.1.14}$$

The relative fluctuations scale with the number of atoms as expected for binomial statistics

$$\frac{\Delta \hat{J}_{\perp}}{J} = \frac{1}{\sqrt{N}} \tag{2.1.15}$$

As it will be clearly stated in next Section, quantum fluctuations are tied to the fundamental precision limit of the interferometer. The way to improve the interferometer performance is to alter the probability distribution of the states to have a non-isotropic distribution, and this will be addressed later in this chapter. For this reason it is useful to represent the quasi-probability distribution of the state on the Bloch Sphere, as shown in Figure 2.1.3. One of the possible definition of the $Q(\theta, \varphi)$ functions that can be found in literature is [13]

$$Q(\theta, \varphi) = \frac{2J+1}{4\pi} \langle \theta, \varphi | \hat{\rho} | \theta, \varphi \rangle \tag{2.1.16}$$

where $\hat{\rho}$ is the system density operator. For our purposes the discussion will be limited to the variances of the distribution.

## 2.2 Linear Mach-Zehnder interferometer and Shot Noise Limit

The non-interacting Bose-Hubbard Hamiltonian in the angular momentum operators formalism, including the well imbalance term, can be written

$$\hat{H} = 2\delta \hat{J}_z - 2\frac{E_J}{N} \hat{J}_x \tag{2.2.1}$$

Control over the energy imbalance and tunneling allows to perform a complete Mach Zehnder interferometric sequence. The interferometer operation is represented in Figure 2.2.1. A state is prepared in a single mode, that for our double well potential correspond to one of the two localized spatial modes. The equivalent of the 50:50 beam-splitter is provided by letting the state evolve under the coupling Hamiltonian for a given amount of time to have a coherent population of both modes with the same probability, or equivalently a "$\pi/2$ pulse" is applied. Then a phase difference between the two modes is accumulated applying an energy imbalance

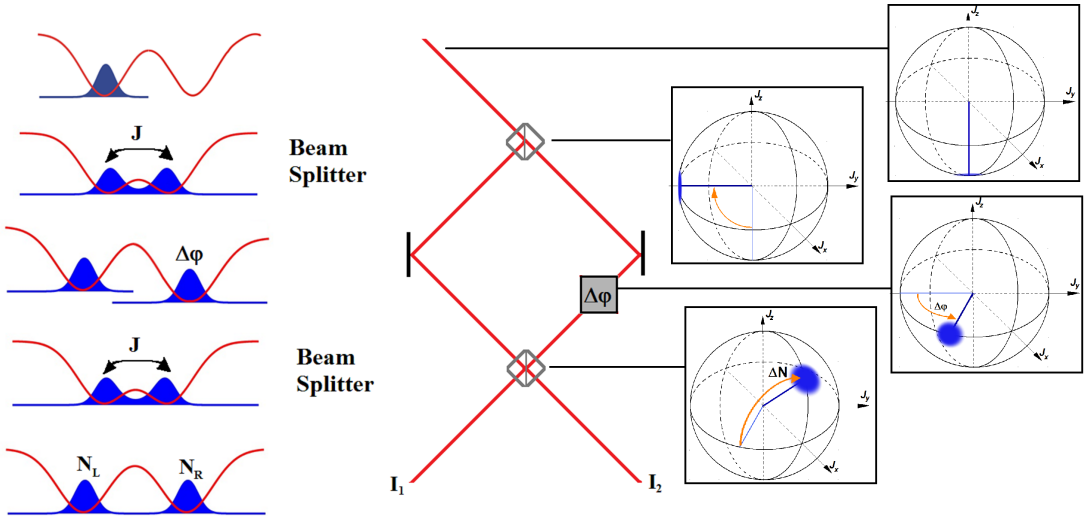


Figure 2.2.1: Linear Mach-Zehnder interferometric sequence with a BEC in a double-well potential compared with it's traditional optical counterpart. On the right the evolution of the state is represented on the Bloch Sphere

between the wells. Then the second beam splitter (corresponding to another $\pi/2$ rotation of the collective spin vector) remaps the physical information about the relative phase (the position on the equatorial plane of the Bloch Sphere) to the number difference (the projection of the vector on the $J_z$ axis of the sphere), that is an observable of our system. This is clearly shown in Figure 2.2.2a.

**Projection Noise and Shot Noise Limit** The uncertainty of the interferometer on phase measurements is then estimated projecting the number fluctuations $\Delta J_z$ after the last beam splitter on the phase space through the functional dependence of the measured final number difference $\langle \hat{J}_z \rangle$ on the accumulated phase $\varphi$; more formally

$$\Delta\varphi = \frac{\Delta J_z}{\left| \frac{\partial \langle \hat{J}_z \rangle}{\partial \varphi} \right|} \tag{2.2.2}$$

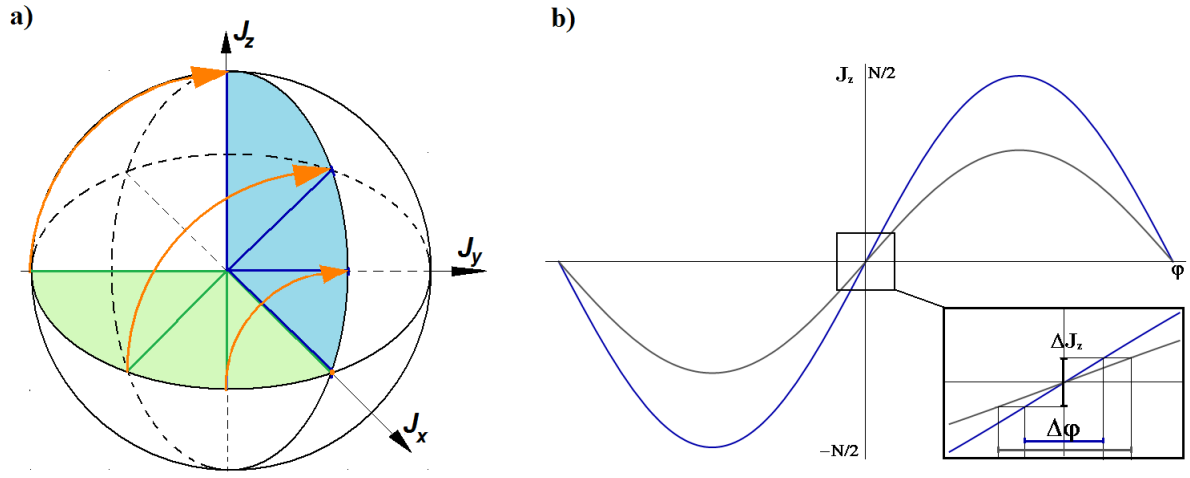


Figure 2.2.2: **a)** The last $\pi/2$ rotation of the interferometer remaps the physical information about the relative phase between the two modes (the angle of the J vector on the equatorial plane of the Bloch Sphere) that is not an observable, into the relative population of the two modes (the projection of J on the z axis). **b)** The effect of visibility on the phase error comparing an interferometer with maximum coherence $\alpha = 1$ (blue) with one with reduced contrast (gray) in the point with maximum slope.

as shown in Figure 2.2.2b. As the indetermination value on the number the minimal value for uncorrelated particles, that is $\Delta J_z = \sqrt{N}/2$ is taken. The derivative in the denominator is

$$\frac{\partial \langle \hat{J}_z \rangle}{\partial \varphi} = \frac{\partial}{\partial \varphi}\left[\frac{N}{2} Sin\left(\varphi\right)\right] = \frac{N}{2} Cos\left(\varphi\right) \tag{2.2.3}$$

in the most sensitive point of the interferometer, where $Cos\left(\varphi\right) = 1$ we obtain

$$\Delta\varphi_{SNL} = \frac{\sqrt{N}/2}{N/2} = \frac{1}{\sqrt{N}} \tag{2.2.4}$$

That is the "Shot Noise Limit", corresponding to the fundamental minimum value of uncertainty reachable with uncorrelated particles. The physical interpretation of this value is straightforward, meaning that operating with a coherent superposition of $N$ uncorrelated particles equals statistically to repeating $N$ times the experiment with a single particle.

Eventual loss of coherence in the system reduces the contrast of $\langle \hat{J}_z \rangle$ in function of the

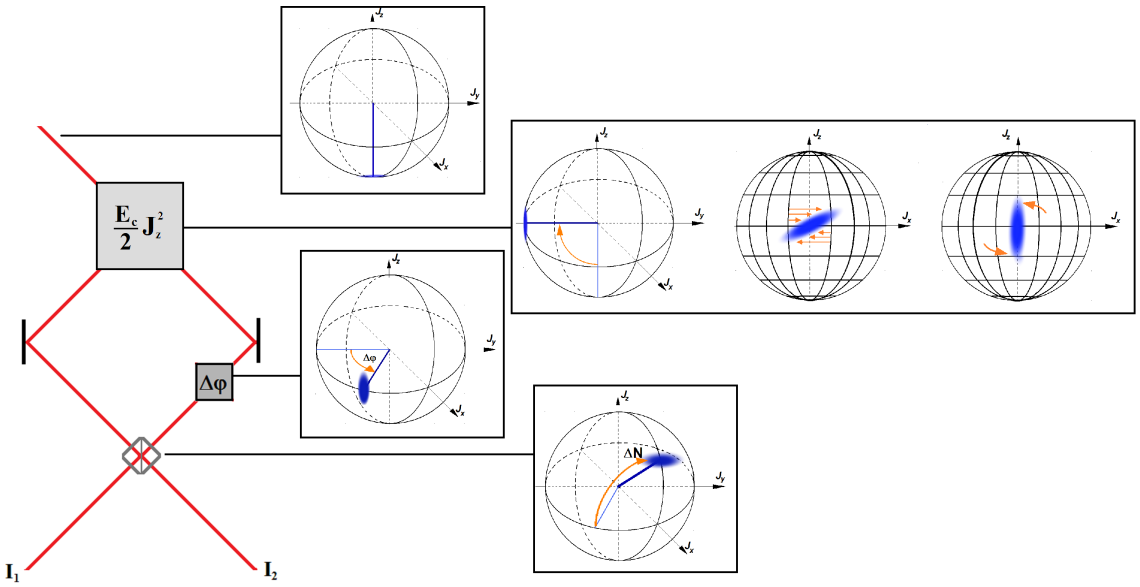


Figure 2.3.1: Mach-Zehnder interferometer employing spin-squeezing. This is analogous to the linear interferometer except for the first atomic beam-splitter that consists into three operations: coherent splitting, squeezing, and rotation of the probability distribution around its axis to have the minimum fluctuations in the phase direction. The output state at the end of the interferometric sequence is characterized by reduced number fluctuations (remembering that the number difference measurement is used to estimate the relative phase value)

phase $\varphi$ as it is shown in Figure 2.2.2b, reducing the value of the derivative (2.2.3), leading to an increase of the phase error

$$\Delta\varphi = \frac{1}{\alpha\sqrt{N}} \tag{2.2.5}$$

## 2.3 Quantum-Enhanced interferometry

### 2.3.1 One-Axis Twisting

Spin Squeezing corresponds to the introduction of entanglement in the system to redistribute quantum fluctuations between noncommuting observables, preserving the minimum uncertainty product. A formal definition of entangled states is the non separability of the density operator in a product of single particle operators, meaning that the density operator cannot

be written in the form

$$\hat{\rho} = \sum_k p_k \hat{\rho}_k^{(1)} \otimes \hat{\rho}_k^{(2)} \otimes ... \otimes \hat{\rho}_k^{(N)} \tag{2.3.1}$$

To quantify the amount of squeezing in a general way (independent from the chosen reference frame), Kitagawa and Ueda introduced a squeezing parameter [14]

$$\xi_N^2 = \frac{\left(\Delta \hat{J}_\perp\right)^2_{MIN}}{J/2} \tag{2.3.2}$$

That is the ratio between the variance in the tighter axis of the distribution and the variance calculated for a coherent spin state of uncorrelated particles. For $\xi_N < 1$ the state is said to be "squeezed". They also demonstrated that this kind of state can be obtained letting a coherent state on the Bloch sphere equator evolve under the nonlinear Hamiltonian

$$\hat{H}_I = \frac{E_C}{2} \hat{J}_z^2 \tag{2.3.3}$$

that is exactly the atomic interaction term of the two-mode Bose-Hubbard Hamiltonian (1.3.34). The minimum of the squeezing parameter is reached for an optimal time after which the state loses coherence. An example of interferometric sequence employing this kind of states is shown in Figure 2.3.1 and exemplifies the key point that the relevant difference between classical and quantum-enhanced interferometry lies in the initial preparation of the state, while the subsequent operations are the same

The resulting phase error for a squeezed state ($\xi_N < 1$) with maximum coherence, from (2.2.2), is

$$\Delta\varphi = \xi_N \frac{1}{\sqrt{N}} \tag{2.3.4}$$

that is below the shot noise limit. The experimental realization of this kind of interferometers has been achieved lately; for example in [16, 17] the shot noise limit was overcame with an internal state atomic interferometer, where the two modes correspond to internal atomic hyperfine states instead of spatially separated modes of the confining potential.

**Connection with Entanglement** It has been introduced in [15] another squeezing criterion

$$\xi_S^2 = \frac{N\left(\Delta \hat{J}_{\mathbf{n}_1}\right)^2}{\left\langle \hat{J}_{\mathbf{n}_2}\right\rangle^2 + \left\langle \hat{J}_{\mathbf{n}_3}\right\rangle^2} \tag{2.3.5}$$

for orthogonal directions $\mathbf{n}_1$,$\mathbf{n}_2$,$\mathbf{n}_3$. This definition takes into consideration the state coherence. Taking for instance a global spin vector pointing in the $J_x$ direction, so that $\langle \hat{J}_y\rangle = 0$

$$\xi_S^2 = \frac{\left(\Delta \hat{J}_z\right)^2}{\left\langle 2\frac{\hat{J}_x}{N}\right\rangle^2 N/4} = \frac{\xi_N^2}{\alpha^2} \tag{2.3.6}$$

where $\alpha$ is the coherence defined in (1.3.27). It has been demonstrated [15] that the more stringent squeezing condition $\xi_S < 1$ is sufficient to have a non-separable (namely entangled) state, with the definition of separability (2.3.1)

### 2.3.2 Beyond Squeezing: Maximally entangled states and Heisemberg Limit

The explanation of the squeezing protocol introduced in the previous Subsection allowed me to introduce three important points

- The fundamental role of the non-separability (entanglement) of states.
- The reduction in number fluctuations is also an important resource for quantum interferometry, since linear operations (precessions on the Bloch Sphere) allow to rotate the probability distribution of the states to exchange number and phase fluctuations.
- The main difference between classical and quantum-enhanced interferometry lies in the initial preparation of the states.

In this subsection I will introduce three possible states characterized by a strong entanglement between particles, the possible ways obtain them with our experimental apparatus and some of their weaknesses. Since this topic concerns the future developments of the experiment I

worked on, and would require the introduction of formal tools beyond the scope of this Thesis to be discussed properly, the discussion will be limited to a qualitative survey.

**Twin Fock States** A possible example of an entangled state with strongly reduced number fluctuations that will be attempted to prepare in our experimental apparatus is the "Twin Fock" state, corresponding to the pure Fock state with half occupation of the left well and half of the right.

$$|\Psi\rangle = \left|\frac{N}{2}, \frac{N}{2}\right\rangle \tag{2.3.7}$$

The way to obtain this state in our system would be to induce strong repulsive interactions between atoms in the single main well by the means of a Feshbach resonance, and to ramp up adiabatically the central barrier to prepare the system in the ground state, with half average population in each well. As demonstrated in Subsection 1.3.3 the ground state number fluctuations in the deep Fock regime are strongly damped, ideally up to the limit corresponding to the state (2.3.7). On the Bloch sphere this state corresponds to a thin ring covering the sphere equator (definite number and totally undefined phase).

**NOON states and Heisemberg Limit** Another possibility is to prepare a state raising up adiabatically the central barrier in presence of strong attractive interactions. In this case the occupation of a single well would be highly favored for energetic reasons, and number fluctuations would be damped as for the repulsive case. In the hypothesis of an ideally symmetric double well, in absence of symmetry-breaking perturbations there is no reason for the system to occupy one well over another, and we expect the prepared state to be in a quantum superposition of a state with all atoms occupying the left well and all atoms occupying the right well

$$|\Psi\rangle = \frac{1}{\sqrt{2}}\left(|N,0\rangle + |0,N\rangle\right) \tag{2.3.8}$$

referred to as "NOON state". The effect of a phase evolution on a NOON state, being $\hat{J}_z$ in the formalism we adopted the operator that generates the phase evolution

$$\hat{U}\left(\varphi\right) = e^{-i\hat{J}_z\varphi} \tag{2.3.9}$$

is

$$|\Psi(\varphi)\rangle = \frac{1}{\sqrt{2}}\left(e^{-i\frac{N}{2}\varphi}|N,0\rangle + e^{i\frac{N}{2}\varphi}|0,N\rangle\right) \tag{2.3.10}$$

showing a phase response enhanced by a factor $N$ compared to separable coherent states. The minimum phase error that can be achieved with this state corresponds to the Heisenberg Limit [18]

$$\Delta\varphi_{HL} = \frac{1}{N} \tag{2.3.11}$$

that is the fundamental precision limit achievable [19]

**Loss and revival of coherence and Phase Cat States** Another way to obtain a maximally entangled state of the sort of (2.3.8) consists into pushing the one-axis twisting protocol for long times, initial loss of coherence. To demonstrate this possibility let's take a coherent state in the form of (2.1.11) on the Bloch Sphere equator and evolve it under the interaction term

$$\frac{E_C}{2}\hat{J}_z^2 \tag{2.3.12}$$

obtaining

$$|\psi(t)\rangle = \sum_{n=-\frac{N}{2}}^{\frac{N}{2}} c_m e^{-i\left(\frac{N}{2}+n\right)\varphi} e^{-i\frac{E_c}{2\hbar}n^2 t}|n\rangle \tag{2.3.13}$$

that in general is not a coherent state anymore, due to the quadratic evolution term. However at certain evolution times coherence is re-obtained

- For $t = \tau = \frac{4\pi\hbar}{E_C}$ the nonlinear evolution term exponent is a multiple of $2\pi$ for every $n$. We obtain the initial coherent state

$$|\psi(\tau)\rangle = |\varphi\rangle \tag{2.3.14}$$

- For $t = \frac{\tau}{2}$ the evolution term exponent can be written as $i\pi n$. This can be absorbed into the coherent state phase term $n(\varphi + \pi)$ obtaining

$$\left|\psi\left(\frac{\tau}{2}\right)\right\rangle = |\varphi + \pi\rangle \tag{2.3.15}$$

- For $t = \frac{\tau}{4}$ we obtain the superposition of two coherent states [20]

$$\left|\psi\left(\frac{\tau}{4}\right)\right\rangle = \frac{1}{\sqrt{2}}\left(e^{-i\frac{\pi}{4}}\left|\varphi + \frac{\pi}{2}\xi_N\right\rangle + e^{i\frac{\pi}{4}}\left|\varphi - \pi + \frac{\pi}{2}\xi_N\right\rangle\right) \tag{2.3.16}$$

  where $\xi_N = 0$ for an even total number of atoms and $\xi_N = 1$ for an odd number of atoms and both are usually referred to as "Phase Cat states". The state with $\xi_N = 1$ is simply rotated of a $\pi/2$ angle on the Bloch Sphere, and is otherwise equal to the one with $\xi_N = 0$ .

Applying the atomic beam-splitter to the Phase Cat state gives a NOON state as a result. This alternative might be easier to implement in a real experiment, considering that the other protocol requires to work with attractive interactions, limited by the consequent instability of the condensate, and it is based on the assumption of a perfectly symmetric double well potential, for which is not clear the tolerance against technical noise. On the other hand in typical experimental conditions there is no control over the parity of the total atom number during the preparation of the Phase Cat state, and in this case the system is described by a classical mixture of both the states.

The states I described in this subsection are in principle capable of pushing the obtainable phase precision limit down to the Heisemberg Limit (with the exception of the Twin Fock, for which it can be demonstrated anyway that the limit scales with the particle number as the Heisemberg Limit). However these maximally entangled states are very fragile against noise or other effects that are surely present in a real experiment. For example we can imagine, starting with a NOON state (2.3.8) to lose a single atom from the trap. This atom could interact with another part of the experiment in such a way to be the equivalent of a measurement on the original position of the atom, collapsing then the NOON state in only one of the two wells.

# Chapter 3

# Experimental Apparatus and Procedure

In this Chapter I will describe the experimental apparatus highlighting some of the relevant features of potassium atoms that justify the choices that were made in the design. Nearly everything that is discussed here is part of the former group members' work in the past years, and more details can be found in their theses and publications [23, 24, 25] with some minor exceptions, while the description of the additional piece of equipment that I mounted and optimized as part of this thesis work will be discussed in Chapter 4.

From the general viewpoint the apparatus consists in two optical tables; the first one is devoted to the preparation of the laser beams necessary to cool, trap and manipulate the atoms. The prepared laser beams are then injected into optical fibers whose outputs are located on the other table, where the experiment takes place. The fundamental part of the experiment consists in three vacuum chambers connected by low conductivity tubes achieving proper differential vacuum levels, as shown in Figure 3.0.1 [25]. In the first one $^{39}$K atoms are sublimated from a solid sample, and a 2D$^+$ MOT is used to produce an atomic beam that is collected from a 3D MOT in the second cell, where a three-steps technique especially designed for potassium allows to cool the sample to sub-Doppler temperatures with a satisfying density. Then the atomic cloud is confined in a magnetic trap mounted on a mechanical translational stage and brought to the last vacuum chamber characterized by the

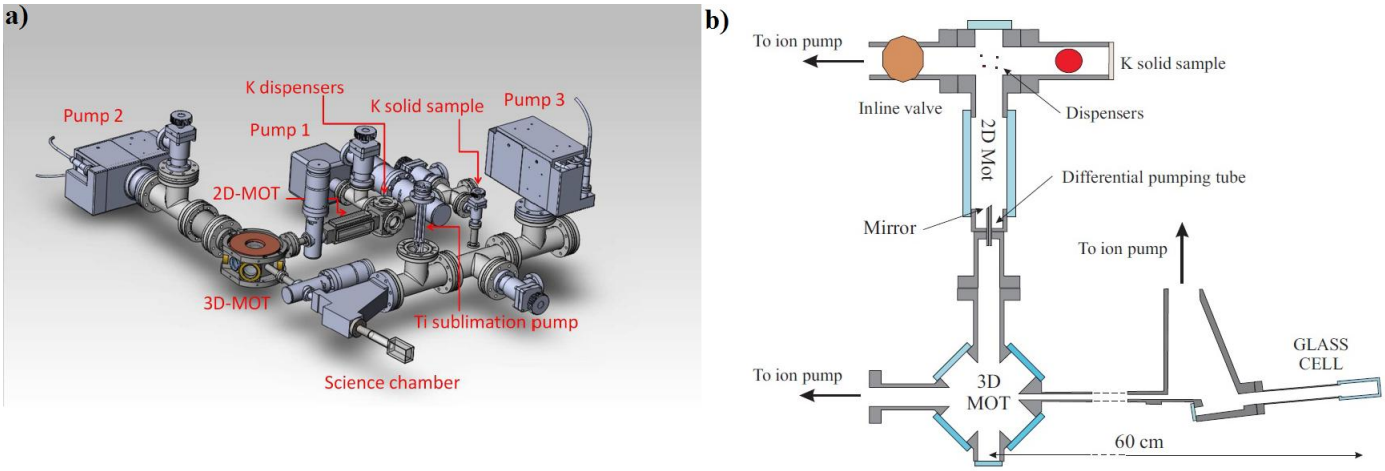


Figure 3.0.1: Representations of the three vacuum chambers where potassium atoms are cooled, led to condensation and used for interferometry .

lowest pressure and a wide optical access, where Bose Einstein condensation is accomplished by means of evaporative cooling into an optical dipole trap potential; this has been achieved, for the first time, without the need of sympathetic cooling with $^{87}$Rb [26] tuning interactions between atoms exploiting Feshbach Resonances. The condensate is then trapped in a single or in multiple double well potentials and the interferometric sequences are performed exploiting the fine control over the potential parameters.

To describe in the most readable way the entire apparatus operation I decided to divide it in four conceptual blocks. In the first one, the "preparation phase", I will describe the first two vacuum chambers, where the sub-Doppler cooling of potassium is achieved, including the magnetic transport to the science chamber, highlighting relevant properties of potassium spectrum and describing how the laser beams necessary for laser cooling and imaging are produced. In the second part I will describe the evaporative cooling sequence of potassium inside the science chamber, and some important collisional properties of this atomic species. The third part will be dedicated to the interferometric experimental sequences: the preparation of the trapping laser beams, where the atoms are condensed and controlled, and the experimental tunability of the trapping potential will be discussed. In the fourth, and last part, a brief description of the imaging systems will be given.

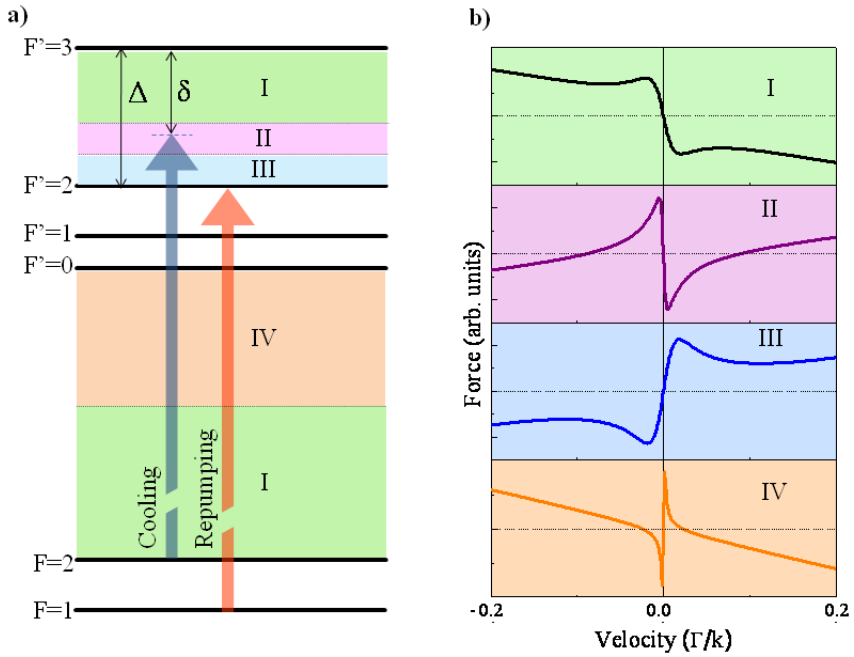


Figure 3.1.1: Working regions of sub-Doppler cooling of $^{39}K$ **(a)** and correspondent cooling forces in function of atomic velocities **(b)**. Doppler cooling is active in regions I and IV, while sub-Doppler in regions I and II.

## 3.1 Preparation Phase

### 3.1.1 Trapping and cooling of potassium atoms

Potassium $^{39}$K atomic level structure has two relevant features compared to other alkalis [27, 28].

The first one is the small level separation in the excited $^2P_{3/2}$ manifold, corresponding to the $D_2$ transition at 767 nm, that is of the same order of magnitude as the natural linewidth of the cooling transition $F_g = 2 \rightarrow F_e = 3$; for this reason the evaluation of the force exerted by the laser beams require a more detailed treatment compared to the simpler case of isolated transitions. Detailed calculations allow to demonstrate [27, 28, 24] that the force in an optical molasse shows different qualitative behaviors depending on the detuning (Figure 3.1.1). Both "Zone I" and "Zone II" detunings allow in principle to cool atoms to sub-Doppler

temperatures, but "Zone I" (that corresponds to the typical behavior for isolated transitions) is characterized from one side by a large capturing range (to above Doppler temperatures), from the other by the low detuning and the consequent high scattering rate that triggers a competing heating mechanism (light-assisted collisions) in the molasse that strongly limits its efficiency.

The second feature is the strong depletion of the $F_g = 2$ to the $F_g = 1$ caused by optical pumping, that requires another repumper beam of higher frequency as shown in Figure 3.1.1a; the frequency difference between the "Cooling" and "Repumping" beams is about 462 MHz. This can be exploited to our advantage, since we are allowed to control the relative population of the bright state $F_g = 2$ with respect to the dark state $F_g = 1$ without the need of an additional depumper laser, and consequently to keep the reabsorption of spontaneously emitted photons under control.

Despite these difficulties sub-Doppler temperatures have been achieved,as will be described below, with a dynamic control over both above mentioned parameters (frequency detuning and repumper relative intensity) during the cooling process.

### 3.1.2 The MOTs laser system

The MOTs and imaging laser system's purpose is to generate all the needed beams, for both cooling and repumping frequencies, starting from a single master laser beam. The master laser is a Toptica DL Pro 780 diode laser with external cavity, whose output beam frequency is stabilized on the potassium cooling transition. Despite being very stable this laser source emits only 50 mW at our wavelength of interest, which is not enough to feed all the needed beams. For this reason we employ four MOPAs (Master Oscillator Power Amplifier) that amplify the input laser signal intensity (ideally up to 2 W) maintaining its spectral characteristics; even though the output spatial mode is degraded and requires to be filtered with optical fibers afterwards, we get on the experimental table about 400 mW of available total power for each one of the two MOTs.

Since the cooling and repumping frequencies are separated by only 462 MHz we use several 200 MHz AOMs (Crystal Technology 3200-124) in double pass configuration to produce the needed beams at the proper frequencies with an additional tunability interval of several tens

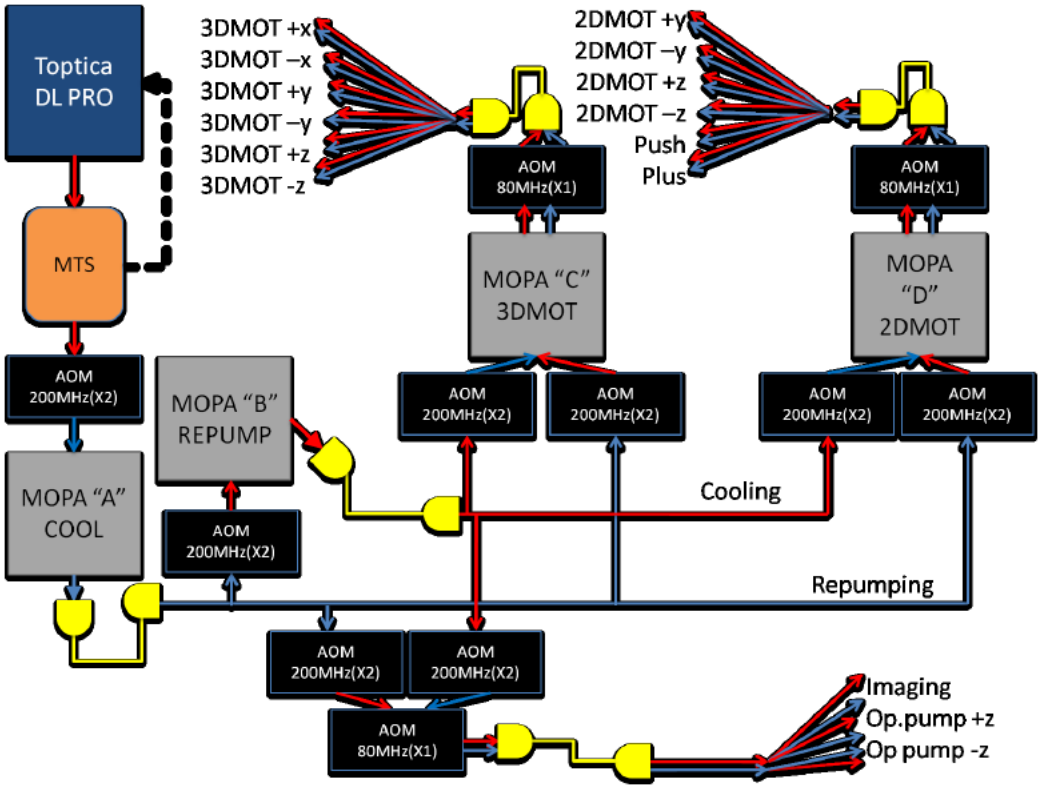


Figure 3.1.2: The MOTs and imaging laser system conceptual scheme. The laser beam is frequency-stabilized at the "cooling" frequency (Red arrows) using the Modulation Transfer Spectroscopy (MTS). 200 MHz AOMs in double-pass configuration are used to switch the frequency of the signal to the "repumping" frequency (Blue arrows) or back with an additional tunable shift. 80 MHz AOMs instead are used as fast shutters. Four MOPAs are employed to generate the needed power for MOTs operation, using optical fibers (represented in yellow) to purify their output spatial mode. [24]

of MHz. To act as "fast pre-shutters" instead we use 80 MHz AOMs (Crystal Technology 3080-122), taking advantage of their fast response compared to mechanical shutters.

A conceptual scheme of the apparatus is shown in Figure 3.1.2.

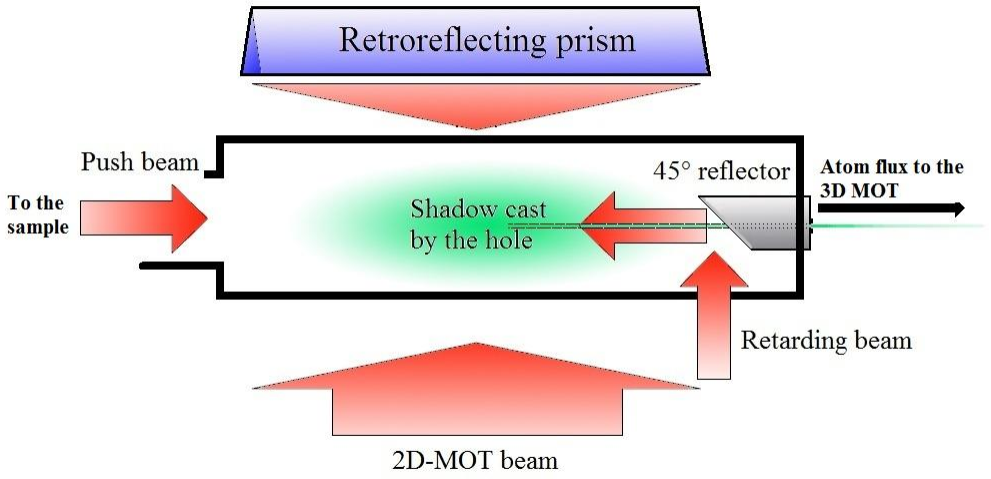


Figure 3.1.3: Side view of the $2D^+$ MOT.

### 3.1.3 The first vacuum chamber

In the first vacuum chamber a solid sample of potassium is thermally sublimated and captured into a $2D^+$ MOT represented in Figure 3.1.3, similar to the one described in [29]; the pressure inside this chamber is estimated to be about $10^{-7} - 10^{-8}\, mbar$.

The $2D^+$ MOT consists of two couples of rectangular coils (37 x 132 mm) whose central axes (that define radial directions) are orthogonal. To have magnetic confinement only in radial direction, for each couple of coils, currents must flow in opposite directions, and magnetic fields must point inside the chamber for a couple and outside for the other. The laser beam coming out of the "MOPA D" optical fiber with a total power of about $400\, mW$ is circularly polarized and splitted in four beams, two of which are retroreflected providing radial cooling and trapping, while of the remaining two, one (push) propagates towards the next vacuum chamber (forward direction), the other (retarding) is reflected in backward direction on a 45° mirror with a 1.5 mm diameter hole in the middle. This hole allows atoms to pass to the next vacuum chamber and causes the pull beam to propagate with a hole in the central axis. The beams' waists are set with telescopes before the MOT chamber.

The spectrum of the beams, monitored with a Fabry-Perot cavity, comprises both the

cooling and repumping frequencies plus sidebands at frequencies $\omega_C - \Delta$ and $\omega_R + \Delta$, with $\Delta \simeq 400\,MHz$, generated by nonlinear effects inside the MOPA gain medium; the sidebands' frequencies are far from atomic transitions and their effect on the atoms should be negligible.

Thermal atoms arriving in this chamber are cooled and confined in radial direction, towards the hole of the retarding beam, so that the coldest atoms are selectively pushed inside the hole of the mirror and to the next vacuum chamber. All the parameters have been optimized to maximize the capture rate of the 3D MOT, located in the subsequent vacuum chamber, that improves for both high atom number flux and low average velocity. The obtained optimal values are $2 \cdot 10^{10}$ atoms/s flux with an average velocity of 25 m/s. [25, 24].

### 3.1.4 3D MOT

Atoms from the first chamber are collected in a 3D MOT inside the second chamber. The pressure is estimated to be $10^{-9}$ mbar. The laser beam coming out of the optical fiber that was injected by "MOPA C" is circularly polarized and splitted in six beams (in this case counter propagating beams are not obtained by retroreflection of the same beam) and a total power of about $400\,mW$ is available, comprising as before repumper and cooling frequencies and the sidebands. The magnetic confinement potential is provided by three pairs of coils in anti-Helmoltz configuration. 3D-MOT operation consists in 3 stages. The first part (loading phase) aims to maximize the captured atom number. Saturation is obtained in about$5s$ for $\backsim 3 \cdot 10^{10}$ atoms, with a temperature of the order of the mK. The detuning in this phase is chosen to be small, with the consequence that the achievable density is limited by light-assisted collisions. In the next phase (Compressed MOT) the repumper light power is ramped down and the cooling laser is increased. Lowering the repumping intensity tend to favor the occupancy of the F=1 hyperfine level, that is a dark state for cooling frequency light, reducing the multiple scattering events, causing an increase of the density by a factor of 10 with some losses in the atom number. In the last phase (Molasses ) the aim is to reach sub-Doppler temperatures, and for this purpose the magnetic field trapping is turned off, the cooling beam detuning is increased and the repumper light is ramped down even more. At the end of the sequence a temperature of about 25 $\mu K$ is reached, with $\backsim 1.5 \cdot 10^{10}$ atoms occupying the $|F = 1\rangle$ ground state hyperfine level.

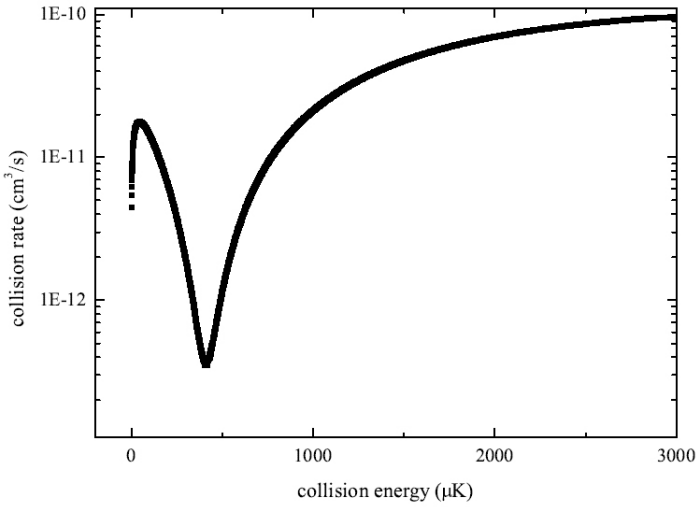


Figure 3.2.1: Ramsauer [25]

### 3.1.5 Magnetic Transport

The atomic cloud is then transferred through a distance of about 540 mm to the Science Chamber where Bose Einstein condensation is achieved with evaporative cooling, and the experimental sequences are carried over. For this purpose a magnetic quadrupole trap is mounted on a motorized translational stage and is turned on inside the MOT chamber after the molasses sequence. Of the $|F = 1\rangle$ manifold only the $|F = 1, m_F = -1\rangle$ state is trapped with a consequent loss of about 2/3 in the atom number. Heating has shown to be negligible with a 2s transport time, while another reduction in atom number of a factor 4 due to the few-seconds lifetime of the cloud in the connection tubes and to the fact that the tube cross section diameter is of the same order as the cloud dimensions is observed.

## 3.2 Bose-Einstein Condensation

### 3.2.1 Collisional properties of potassium atoms

The effect of atomic interactions on dilute cold bosonic atoms physical properties is transversely characterized by the s-wave scattering length $a$, that defines the low energy limit for

the elastic scattering cross-section

$$\lim_{k\to 0} \sigma_{tot} = 8\pi a^2 \tag{3.2.1}$$

This parameter allows to describe interaction in a simple picture, where the particular features of the interatomic potential can be neglected in favor of an effective pseudopotential,

$$V_{int}(\mathbf{x}, \mathbf{y}) \simeq \frac{4\pi\hbar^2 a}{m}\delta(\mathbf{x} - \mathbf{y}) \tag{3.2.2}$$

from which is evident that the sign of $a$ determines if the effective potential is attractive ($a < 0$) or repulsive ($a > 0$). This approximation relies on physical assumptions usually valid in case of cold bosons, namely low collisional energy and the symmetry of the atomic wavefunction for identical particle exchange.

In case $a$ is small and negative a minimum in the scattering cross section for low energies is observed; this is also the case of potassium whose scattering cross section drops for collisional energies of $\sim 400\ \mu K$ as in Figure 3.2.1. For this reason evaporative cooling efficiency is hampered once that temperature is reached since the atom cloud isn't anymore able to thermalize due to the suppression of elastic collisions rate; in the past years the only way to cool evaporatively potassium atoms was the employment of sympathetic cooling [26], consisting in the preparation of a mixture of two atomic species, one of which (usually Rb) has suitable collisional properties to thermalize the entire mixture for the whole range of temperatures down to quantum degeneracy. In this experiment we avoided the technical difficulties and long evaporation times tied to the aforementioned method exploiting the presence of Feshbach resonances.

Feshbach resonances are a general feature of the physics of collisions and emerge also in the general analytically solvable model of scattering by a square-well potential. The phenomenon consists in the dispersive behavior of collisional cross section when the energy of free particles in a scattering channel approaches the energy of a bound state in another channel (see Figure 3.2.2). The scattering length will be large and negative (positive) if the energy of the free state is slightly lower (higher) than energy of the bound state. If these channels correspond to different magnetic moments their relative energy can be shifted by

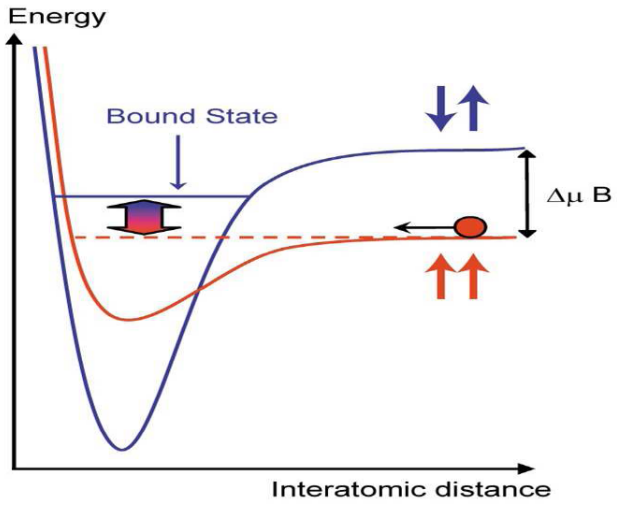


Figure 3.2.2: Basic principle of Feshbach Resonances

the presence of a magnetic field. This allows to tune the interactions between atoms if a suitable transition is present, avoiding the Ramsauer-Townsend minimum and increasing the scattering rate, leading to faster thermalization of the sample during evaporation. There are several drawbacks that experimentalist must consider when adopting this technique. First of all since magnetic resonances depend on the involved magnetic quantum numbers and some states are difficult to prepare, some resonances could not be worth the technical difficulties . Second, a proper control and stability of the magnetic field intensity are required, depending on the width and the slope of the particular resonance employed; other sources of magnetic fields, including trapping gradients, must be avoided if their effect is significative. Third, when high interactions are desired, the the working point must be chosen according to a tradeoff between the interaction value and the emergence of an inelastic scattering peak near the resonances, leading to an increase in atom loss rates. In Figure 3.2.3 Feshbach resonances for potassium are shown.

### 3.2.2 The Science Chamber

The Science Chamber consists in a 4x4x7 cm glass cell characterized by a wide optical access, allowing the use of different laser trapping beams to manipulate the condensate and multiple

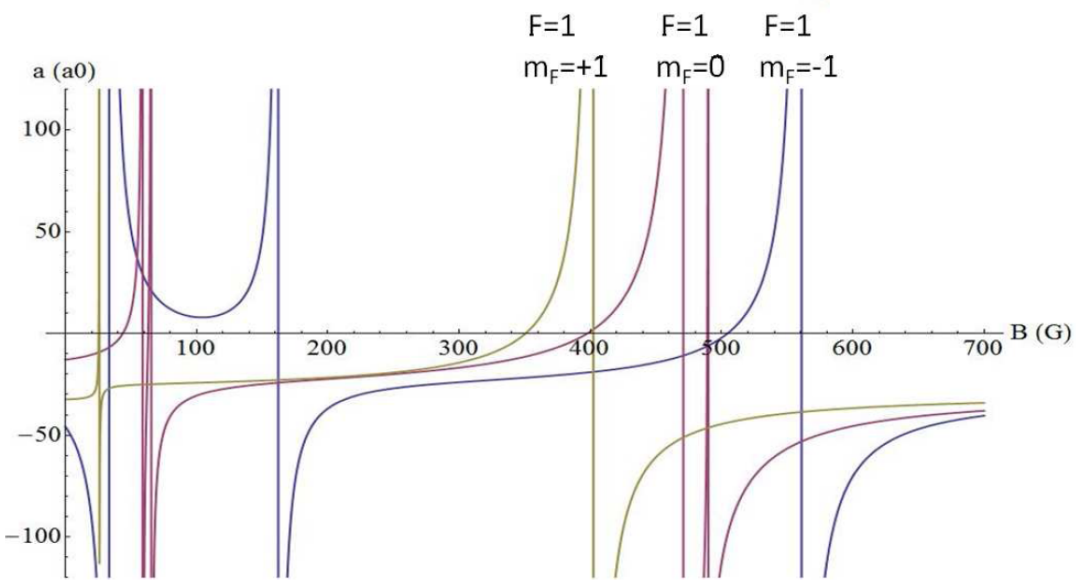


Figure 3.2.3: Feshbach resonances in potassium 39

imaging systems. The pressure inside the Science Chamber is even lower than in the other chambers, about $10^{-11}$ mbar, with a consequent strong increase in the trapped atom cloud lifetime to $\sim 100\ s$ due to the reduction of background scattering losses. Magnetic coils, able to provide both confining and gravity compensation gradients plus the homogeneous magnetic field necessary to tune the atom-atom interactions, are positioned above and below the chamber.

After the translational stage reaches the chamber, a magnetic quadrupole potential is turned on inside the chamber and the transport trapping potential is turned off, drawing the atoms in the middle of the chamber. After the transfer we have $\sim 10^9$ atoms with a temperature of $\sim 250\,\mu K$ trapped in the science chamber quadrupole magnetic potential.

### 3.2.3 Evaporative Cooling

After the atoms have been drewed in the quadrupole trap of the science an optical potential is turned on using an IPG photonics YLR-100-LP-AC ytterbium fiber laser . This laser operates at about 1064 nm wavelength, affecting atoms with an attractive potential, being red-detuned

with respect to the atomic transitions, and provides the optical confinement where the first part of the evaporation is achieved. The dipolar trap is not superimposed to the center of the quadrupole magnetic trap to avoid Majorana spin flips. After few seconds with both dipolar and quadrupolar potentials $\sim 10^7$ atoms are trapped with a temperature of $\simeq 1000\,\mu K$ in the dipole trap, and the quadrupole trap is switched off. This step required some optimization, due to the fact that the IPG beam waist had to be chosen as a tradeoff between the need of good overlap with the quadrupole trap (less focusing) and the requirement to have a proper longitudinal confinement (more focusing); moreover, to remain trapped in the optical trap, an atom must collide with another one to transfer its excess energy, and care has to be taken to avoid the Ramsauer minimum at this stage. Another issue comes from the fact that the IPG is a multimode laser, that shows power-dependent losses. This is caused by photo-association of two photons and two atoms, namely light assisted two-body collisions [30].

The realization and optimization of evaporative cooling revolves around the involved processes' time scales. It's intuitively obvious that the lower limit to the process is set by the thermalization time scale, that can be assumed of the same order of elastic collision time $(nv\sigma)^{-1}$: if the evaporative sequence is faster then atoms don't have time to thermalize and we stop discriminating the most energetic atoms during the evaporation. The upper limit is set instead by heating and losses. The evaporation time scale can be optimized between these two limits setting the ratio between the potential depth and the thermal energy scale, or truncation parameter

$$\eta = \frac{U_0}{k_B T} \tag{3.2.3}$$

lower truncation parameter determines faster evaporation and vice versa. The evaporation had been optimized dividing the sequence in ten steps, and optimizing the parameters for each step to maximize the phase space density. The strong power dependence of light-assisted losses makes them more significative at the beginning of the evaporation, with the consequence that the optimal evaporation ramp is faster at the beginning.

We use two different Feshbach resonances during the evaporation process. At the beginning we keep the atoms in the $m_F = -1$ state, and exploit the resonance at $B \simeq 34G$ (Figure 3.2.3) tuning the scattering length to positive values. Then we adiabatically transfer atoms to the $m_F = +1$ ground state with an RF-field circular antenna and increase the magnetic

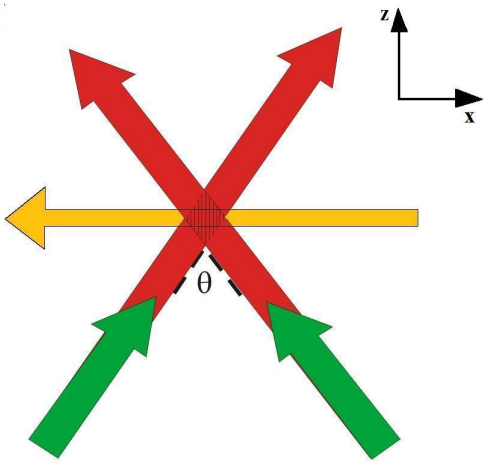


Figure 3.3.1: **a)** A pictorial representation of the laser trapping beams. The two arms coming out of the box are equal and each of them consists in a superposition of a 1064 nm infrared light beam (Red in figure) and a 532 nm green light beam (green in figure). From their interference an array of double well potentials for potassium atoms is obtained. The 1064 nm Radial confinement beam (yellow in figure) propagates in the direction of the lattice.

field to the $B \simeq 400\,G$ Feshbach resonance.

## 3.3 Double-Well potentials

### 3.3.1 Double wells potential 1D model

The experimental realization of the array of double well potentials has been designed following two important requirements. The first one is to have direct experimental control over the Bose-Hubbard Hamiltonian parameters, namely tunneling and energy imbalance between the two wells. The other important requirement is stability: while tracking and eliminating every possible source of noise is the most obvious and effective strategy, an ideal cancellation is not possible and a proper design can reduce their effect on the experiment.

A single tunable-period optical lattice can be obtained crossing two laser beams with the same frequency $\omega$, intensity and electric field polarization direction $\hat{\epsilon}$. This can be simply

modeled calculating the interference between two plane waves propagating with a relative angle $\theta$

$$\mathbf{E_{TOT}}(\mathbf{x},t) = \mathbf{E}_1(\mathbf{x},t) + \mathbf{E}_2(\mathbf{x},t) = E \cdot \hat{\epsilon}\left(e^{i(\mathbf{k_1}\cdot\mathbf{x}-\omega t)} + e^{i(\mathbf{k_2}\cdot\mathbf{x}-\omega t+\phi)} + c.c.\right) \tag{3.3.1}$$

Describing the crossing beams with plane waves is a good approximation if the overlapping region is in the focal region of the beams, within the Rayleigh Range of the beams.

$$z_R = \frac{\pi w_0^2}{\lambda} \tag{3.3.2}$$

where $w_0$ is the beam waist in the focus. With $|\mathbf{k}_1| = |\mathbf{k}_2| = k$, using trigonometric relations and expressing $\mathbf{x}$ in Cartesian coordinates $(x, z)$ (chosen as in Figure 3.3.1a)

$$\mathbf{E_{TOT}}(\mathbf{x},t) = 4E\,Cos\left(k\,Cos\left(\frac{\theta}{2}\right)z - \omega t + \frac{\phi}{2}\right)\,Cos\left(k\,Sin\left(\frac{\theta}{2}\right)x - \frac{\phi}{2}\right)\hat{\epsilon} \tag{3.3.3}$$

In the crossing region the field shows a stationary periodic envelope in the $\hat{x}$ direction with period depending on the crossing angle $\theta$.

The relative phase between the two beams $\phi$ determines the exact position of the maxima and minima of the envelope. Our primary lattice is obtained with infrared light ($\lambda_{IR} = 1064\,nm$), red-detuned with respect to the potassium atomic transitions, leading to an attractive potential proportional to the local intensity.

$$I(x) \propto 1 + Cos\left(2k\,Sin\left(\frac{\theta}{2}\right)x - \phi\right) \tag{3.3.4}$$

with period

$$d = \frac{\lambda_{IR}}{2\,Sin\left(\frac{\theta}{2}\right)} \tag{3.3.5}$$

corresponding to $d \sim 10\,\mu m$ with our choice of $\theta \sim 6°$.

The double well potential can be achieved superimposing a second optical lattice to the first one, crossing two laser beams with $2\omega$ frequency and the same crossing angle. In our case it corresponds to $\lambda_G = 532\,nm$, that is blue detuned with respect to potassium atomic transitions leading to a repulsive potential. The periodicity of this secondary lattice is half

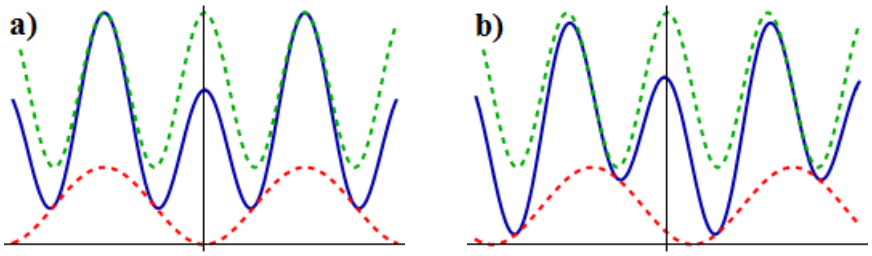


Figure 3.3.2: Spatial variation of an array of double well potentials (Blue), plotted in arbitrary units, obtained summing two intensity contributions in the form of (3.3.4) for the infrared lattice (Red) and the green lattice (Green). **a)** The configuration where the green potential maxima correspond to the maxima and the minima of the infrared lattice. **b)** The infrared lattice is translated with a phase factor $\pi/4$, and the resulting potential with unbalanced minima is plotted.

the primary, corresponding to $\sim 5\,\mu m$.

So far, atoms are free in directions orthogonal to the lattice $\hat{x}$ and $\hat{y}$ . To provide radial confinement another infrared beam ($\lambda_{RAD} = 1064\,nm$) is employed. In ideal working conditions this beam lies on the same vertical plane of the two crossing lattice beams, and propagates in the horizontal symmetry axis (the x direction), as shown in Figure 3.3.1a.

This multiple-well configuration yields an increase in the measurement statistics, having many experiments running in parallel for a single condensation cycle. Moreover it allows to detect the effect of common mode noise.

**Achieving control and stability** As it is evident from (3.3.4), controlling the relative phase between the beams for each of the two lattice allows to translate them in space. The symmetric double-well potential corresponds to the situation where green intensity maxima are superimposed to the maxima and minima of the primary infrared lattice intensity, as shown in Figure 3.3.2a. Introducing a relative shift the double well configuration is retained with an energy imbalance between the two wells (Figure 3.3.2b). This is a critical parameter, and fluctuations here are undesired.

As a matter of fact a small (of the order of a single wavelength) fluctuation in the optical path length of one of the two beams will have a dramatic effect on the relative position of the corresponding lattice, destroying the double well configuration. For this reason the

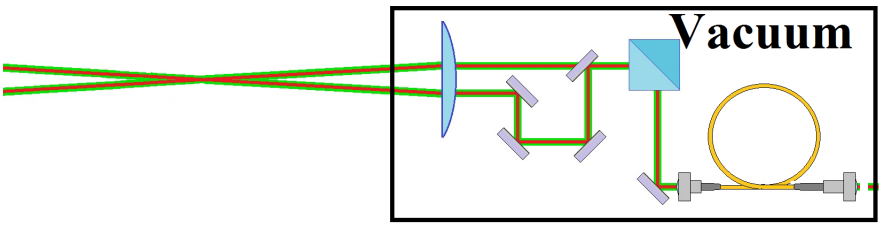


Figure 3.3.3: The two copropagating beams are splitted in a vacuum box and a path difference of $\sim 25\,cm$ is imposed between the two arms, before crossing again in the science chamber.

experimental setup has been designed to reduce the effect of this kind of fluctuations to a common mode shift of both lattices, to maintain the double well potential shape. As shown in Figure 3.3.3 two beams with the frequencies of interest are send into an optical fiber. After its output each of the two superimposed beams is splitted in a 50:50 optical beam-splitter suitable for both wavelengths. A path difference of $\sim 25\,cm$ is imposed between the two arms; the four beams are finally crossed inside the science chamber. The three important features of this design and their consequence on the potential stability and control are

- The pair of beams for each lattice are obtained splitting a single beam. Eventual phase fluctuations or jumps in the laser signal are canceled, since it is a common phase factor. Power fluctuations of the laser source affects both beams in the same way.

- After the splitting, beams in each branch are superimposed. A fluctuation in one of the branches path length $\delta l$ induces a phase shift $\delta\phi = k_{IR} \cdot \delta l$ for the infrared lattice envelope, and double this quantity for the green lattice $2\delta\phi$. The two lattices are then translated of the same quantity in real space

$$\Delta x_{IR} = \frac{\delta\phi}{2k\,Sin\left(\frac{\theta}{2}\right)} = \frac{2\delta\phi}{4k\,Sin\left(\frac{\theta}{2}\right)} = \Delta x_G \tag{3.3.6}$$

  so fluctuations in the path length translate rigidly the array of double wells.

- The macroscopic path difference allows to change the relative position of the two lattices controlling the quantity $\Delta\nu = \nu_{IR} - 2\nu_G$, where $\nu_{IR}$ and $\nu_G$ are the infrared and green laser frequencies respectively and $\Delta\nu \ll \nu_{IR,G}$. After propagation with a path difference

$\Delta L$ between the two arms the phase difference shift is

$$\Delta\phi = \Delta L \frac{2\pi\Delta\nu}{c} \tag{3.3.7}$$

meaning that for $\Delta L = 25\,cm$ a phase shift of $\pi$ is obtained with $\Delta\nu = 600\,MHz$, corresponding to a complete sweep of the central barrier position in the fundamental well.

As it will be explained in more details in next subsection, the height of the central potential barrier (hence the tunneling between the two wells) is controlled changing the power of the green laser beam injected into the fiber before the splitting and the relative position between the two lattices (and consequently the energy imbalance between the two wells) is selected tuning the primary lattice laser frequency.

**Open problems** At the moment we are running the experiment in the single double well configuration. In the past months we indeed observed that we were not able to center the potential barrier in all the wells simultaneously. After investigating the problem we concluded that the fiber collimator we are using inside the lattice box induces a difference in the angular spread of the beams above the maximum tolerance. For this reason we cannot satisfy the plane-wave approximation in the same region for both beams simultaneously, and we observe a change in relative lattice periodicity for different wells. To solve this problems we have ordered a new collimator.

Increasing the power we have at disposition for the green lattice beams will allow us to reduce the beam focusing in the crossing region, increasing the power and period uniformity of the lattice, that is of critical importance to have an high number of high-fidelity replicas of the same double well potential. For this reason a new frequency doubling crystal has been prepared, as described in Chapter 4

### 3.3.2 Laser System

The laser beams necessary to perform the last part of the experiment are prepared, like the ones for the MOT system, on a separate table. In Figure 3.3.4 a conceptual scheme of the

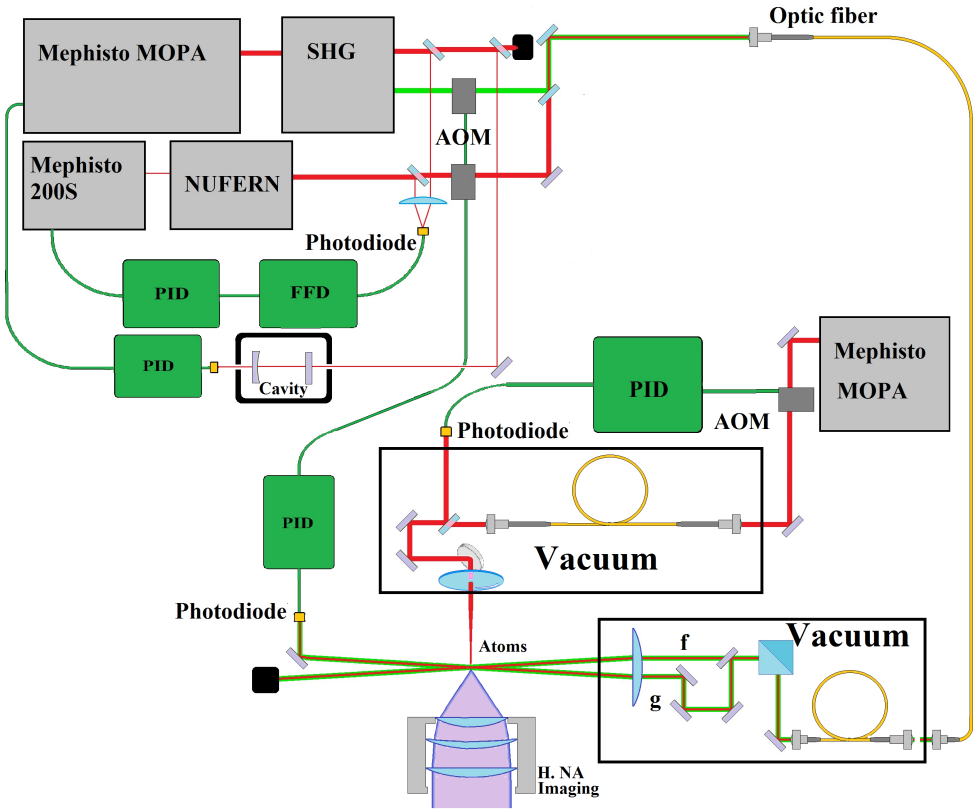


Figure 3.3.4: Laser system conceptual scheme

apparatus is shown.

The infrared radial trapping laser beam is provided by a Mephisto MOPA single mode laser. It's output feeds directly a second harmonic generation crystal whose output is used for green secondary lattice. Part of my thesis work, as will be discussed in details in Chapter 4, consisted in mounting and optimizing a new second harmonic generation crystal that has not still been implemented in the experiment.

The infrared primary lattice beam instead is generated by a Mephisto 200S laser amplified in a NUFERN fiber amplifier that delivers about 10 W of power. Part of the output infrared signals, both from the NUFERN and from the Mephisto MOPA are sent to a photodiode capable of revealing the modulation of the beat note. The signal is mixed with an independent

tunable oscillator, and the resulting signal is stabilized with respect to another frequency reference, changing the frequency of the Mephisto 200S. This allows both to control and stabilize the relative frequency of the primary and secondary lattice beams, with the consequent stability and tunability of the corresponding optical lattices relative positions. The absolute frequency of the Mephisto MOPA is stabilized employing a resonant cavity, to improve the stability of the lattice against common mode translations.

Before injecting the beams into optical fibers leading to the experimental table, their power is stabilized sending each of them through an AOM driven by a PID controller.

**The Vacuum Boxes** On the experimental table the beams are sent into specially designed box, where the last optical elements are put under vacuum and acoustically insulated from the boxes walls. One box is dedicated to the radial beam, and it's located at one side of the science chamber, while in the other, located below the science chamber, the two superimposed lattice beams are splitted and prepared as described before. The alignment between the crossing lattice beams and the radial beam is remotely controlled tilting the last mirrors of both vacuum boxes with stepper motors.

### 3.3.3 Atom condensation

While evaporation is still taking place in the IPG potential, the Radial beam is turned on; the two beams cross in the most tightly focused region of both, and the IPG potential is still dominant. After the IPG potential becomes comparable with the Radial beam potential, if we want to distribute atoms in an array of double well potentials, we continue ramping down the IPG, transferring atoms to the radial potential, then complete the evaporation sequence ramping down the radial intensity with the primary lattice turned on, producing several condensates in the primary lattice potential wells. If instead our objective is to use all the atoms for a single interferometer we evaporate in the crossing between the IPG and the Radial beam ramping down both of them, then raising up the lattice potential and turning off the IPG. In both cases the final total number of atoms in the condensate is $\sim 10^3$, and interactions between atoms can be turned off setting the magnetic field at about 350 G. At this point the proper interferometric sequence is commenced.

## 3.4 Imaging Systems

One of the imaging systems in the experiment is used in the initial setup of the experiment to optimize the atom number and load rate of the 3D MOT. The resonant MOT laser beams flash the atoms with an intensity well above the saturation intensity $I \gg I_S$ for a very short time, and a fraction of the re-emitted light is captured by a CCD camera (Stingray F-145B/C, Allied Vision Technology). The atom number is inferred from the fluorescence signal intensity. To avoid saturation of the signal the detuning of the imaging light with respect to the atomic transition can be increased.

The other three imaging systems instead are used to reveal and count atoms via absorption imaging in the final part of the experiment, exploiting the wide optical access of the science chamber. This technique consists into sending a low intensity ($I \ll I_S$) probe resonant light beam through the atoms to the measuring device. Atoms absorb part of the incoming signal proportionally to the local column density of the atomic cloud according to the Lambert-Beer Law

$$\frac{I}{I_0} = e^{-\sigma n(x,y)} \tag{3.4.1}$$

where $\sigma$ is the scattering cross-section for the imaging light. The presence of atoms is then registered as a negative image in the probe beam intensity profile. In principle to measure the ratio $I/I_0$ for each point it would be sufficient to acquire two images, one of the imaging light without the atoms and one of the light with the atoms, and calculate the ratio for each pixel. To increase the signal-to-noise ratio we acquire a third image without imaging light and without atoms, and subtract it from both images before performing the ratio.

Two of the three imaging systems employ Stingray CCD cameras to acquire the images, one from the vertical direction and the other from the horizontal direction. The last system, referred to as the "high resolution imaging system" employs a long focal length objective lens and an Andor Ikon-M digital camera, and acquires images in the horizontal direction . The micrometers to pixel conversion factor have been measured for both horizontal imaging systems observing atoms in free fall for different times. For the "low resolution" system the conversion factor is

$$\alpha = (0.74 \pm 0.07)\ \frac{pixel}{\mu m} \tag{3.4.2}$$

and for the "high resolution" system

$$\alpha = (2.4 \pm 0.2)\ \frac{pixel}{\mu m} \tag{3.4.3}$$

# Chapter 4

# Second Harmonic Generation of light

As explained in Section 3.3.1, the possibility to use our superlattice configuration to have an array of equal double well potential is based on the hypothesis that the crossing beams can be locally approximated as plane waves. Should this hypothesis break, in presence of curved wavefronts, the lattice periodicity would be different for different points in space and the position of the central barrier in each well would change. This issue can be solved increasing the laser beam power at our disposition, in this way we could reduce the beam focusing increasing the region of space where the plane wave approximation is well-grounded. Defocusing also increases the smoothness of the intensity profile of the beams, improving the hypothesis of having an uniform beam intensity in a larger area. For these reasons we ordered a new Second Harmonic Generation crystal for our wavelength of interest, capable of giving more output power. The task of mounting, testing and optimizing the crystal had been assigned to me as an individual project inside the experimental framework.

In the first Section of this Chapter I introduce the general physical phenomenon underlining the importance of taking symmetry properties into consideration. In the second Section the problem of Phase-Matching and its usual practical solutions will be explained. In the third Section the optimal focusing parameter for Gaussian beams will be introduced. In the last three Sections the experimental apparatus, the optimization procedures and the results I obtained will be presented

## 4.1 Second Harmonic generation in nonlinear anisotropic media

For homogeneous linear optical material the induced dielectric polarization vector is proportional to the electric field propagating inside the medium

$$\mathbf{P^{(1)}} = \epsilon_0 \boldsymbol{\chi}^{\mathbf{(1)}} \cdot \mathbf{E} \tag{4.1.1}$$

where $\epsilon_0$ is the dielectric constant of the vacuum and $\boldsymbol{\chi}^{\mathbf{(1)}}$ is the linear electric susceptibility tensor (scalar for isotropic materials).

For sufficiently strong fields real materials exhibit deviations from the linear behavior. These deviations, if small enough, can be accounted for with a series expansion [31]

$$\mathbf{P} = \epsilon_0 \boldsymbol{\chi}\left(\mathbf{E}\right) \cdot \mathbf{E} \simeq \epsilon_0 \left( \boldsymbol{\chi}^{\mathbf{(1)}} \cdot \mathbf{E} + \boldsymbol{\chi}^{\mathbf{(2)}} : \mathbf{EE} + \boldsymbol{\chi}^{\mathbf{(3)}} \vdots \mathbf{EEE} + ... \right) \tag{4.1.2}$$

writing explicitly the second order term (taking $\epsilon_0 = 1$ from now) we get

$$P_i^{(2)} = \sum_{jk} \chi_{ijk}^{(2)} E_k E_j \tag{4.1.3}$$

where the indices $i, j, k$ are referred to the Cartesian components. Since each index of the $\chi_{ijk}^{(2)}$ tensor can take three values, the most general second order susceptibility tensor has 3 x 3 x 3 = 27 components.

Second harmonic generation (SHG) can be obtained exploiting the second order nonlinear term (4.1.3). To see this in a very simple way we can consider a monochromatic wave propagating in the $x$ direction and polarized in the $z$ direction

$$\mathbf{E}\left(\mathbf{x}, t\right) = E_z \left[ e^{i(kx - \omega t)} + c.c. \right] \hat{z} \tag{4.1.4}$$

Assuming the medium is transparent in the frequency range of interest the susceptibility is independent of frequency. Inserting (4.1.4) in (4.1.3) we get a second order polarization

component of frequency $2\omega$

$$P_i^{(2)} \simeq \chi_{izz}^{(2)} E_z^2 \left(2 + e^{i(2\mathbf{kx}-2\omega t)} + c.c.\right) \tag{4.1.5}$$

and leads to the emission of light with the same frequency. It is worth noticing that other second order effects can be obtained in the same way if we have more waves propagating with different frequencies inside the nonlinear medium, including sum frequency generation (SFG), difference frequency generation (DFG), optical parametric amplification (OPA) [35, 36]

**Electric field permutation symmetry** There is no physical meaning in the order of the two electric field components in (4.1.3), so we can introduce the permutation symmetry between $j$ and $k$ indices

$$\chi_{ijk}^{(2)} = \chi_{ikj}^{(2)} \tag{4.1.6}$$

that allows to contract $jk$ in a single subscript

$$xx \to 1 \quad yy \to 2 \quad zz \to 3 \quad yz \to 4 \quad xz \to 5 \quad xy \to 6$$

with a reduction of the independent coefficients to 3 x 6 = 18, and to write the susceptibility tensor in matrix form, employing the Kleinman $d$ coefficients.

$$\begin{pmatrix} P_x \\ P_y \\ P_z \end{pmatrix} = \begin{pmatrix} d_{11} & d_{12} & d_{13} & d_{14} & d_{15} & d_{16} \\ d_{21} & d_{22} & d_{23} & d_{24} & d_{25} & d_{26} \\ d_{31} & d_{32} & d_{33} & d_{34} & d_{35} & d_{36} \end{pmatrix} \begin{pmatrix} E_x^2 \\ E_y^2 \\ E_z^2 \\ 2E_yE_z \\ 2E_xE_z \\ 2E_xE_y \end{pmatrix} \tag{4.1.7}$$

**Non-ionic process in lossless media** As discussed by Kleinman [32] another restriction to $\chi_{ijk}$ apply if the dominant polarization mechanism is electronic rather than ionic and the media is lossless. In these conditions it is possible to define for the crystal an energy function

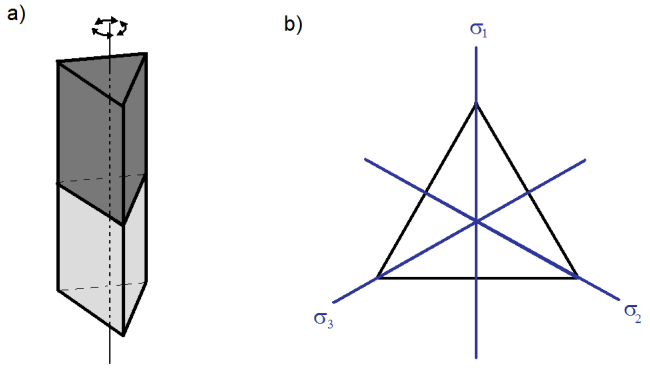


Figure 4.1.1: **a)** Generic object exhibiting $C_{3v}$ symmetry **b)** Top view showing the displacement position of reflection symmetry planes

dependent only on the electric field $U(\mathbf{E})$ such that

$$\mathbf{P} = -\nabla_{\mathbf{E}} U(\mathbf{E}) \tag{4.1.8}$$

the energy function can be written as a power series, and for the third order term

$$U^{(3)} = -\frac{1}{3}\sum_{ijk} \chi^{(2)}_{ijk} E_i E_j E_k \tag{4.1.9}$$

from which

$$P^{(2)}_i = -\frac{\partial U^{(3)}}{\partial E_i} = \sum_{jk} \chi^{(2)}_{ijk} E_j E_k \tag{4.1.10}$$

from (4.1.9), since there is no physical meaning associated to the order of the electric field components in the definition of the third order energy $U^{(3)}$, the second order susceptibility $\chi_{ijk}$ must be symmetric with respect to exchange of all three indices. With this symmetry we get one single coefficient $\chi^{(2)}_{ijk}$ if all the three indices are different, 3 x 2 = 6 possible combinations picking up a couple of equal indices out of three, and 3 coefficients corresponding to three equal indices, for a total of 10 independent coefficients. This symmetry is well justified for SHG applications, since they are usually carried in the lossless regime and above the frequency of ionic resonances [33].

**Crystal symmetry: the case of Lithium Tantalate**

For crystalline materials the remaining coefficients are not, in general, independent all of each other, neither all different from zero. The susceptibility tensor is required to be invariant under all the spatial transformations that leave the crystal structure unvaried - these, called symmetry operations, form a group. Formally the second order susceptibility must satisfy for each operation $R$ in the symmetry group the characteristic equation

$$\chi^{(2)}_{ijk} = \sum_{\alpha\beta\gamma} \chi^{(2)}_{\alpha\beta\gamma} R_{\alpha i} R_{\beta j} R_{\gamma k} \tag{4.1.11}$$

The simplest example to underline the importance of symmetry is the case of point-inversion symmetry. In that case for the Cartesian basis representation $R_{\alpha i} = -\delta_{\alpha i}$ and invariance (4.1.11) requires

$$\chi^{(2)}_{ijk} = -\chi^{(2)}_{ijk} = 0 \tag{4.1.12}$$

for all combinations of Cartesian coordinates showing that point inversion symmetry prohibits SHG.

After this simple example let's consider our case of interest, $LiTaO_3$. Lithium Tantalate cells have $C_{3v}$ symmetry (Figure 4.1.1); it's symmetry elements are a vertical rotation axis (chosen as the $z$ axis) and three vertical reflection planes. The operations $R$ of the symmetry group are clockwise and anticlockwise $\frac{2\pi}{3}$ rotations $C_3^+$ and $C_3^-$, reflection with respect to each of the three planes ($\sigma_1, \sigma_2, \sigma_3$ operations), and of course identity $E$. Representing the operations in matrix form on the basis of Cartesian components, from (4.1.11) the ten coefficients we obtained for lossless media reduce to only three independent, and the second order dielectric polarization dependence on electric field is

$$\begin{pmatrix} P_x^{(2)} \\ P_y^{(2)} \\ P_z^{(2)} \end{pmatrix} = \begin{pmatrix} 0 & 0 & 0 & 0 & d_{31} & -d_{22} \\ -d_{22} & d_{22} & 0 & d_{31} & 0 & 0 \\ d_{31} & d_{31} & d_{33} & 0 & 0 & 0 \end{pmatrix} \begin{pmatrix} E_x^2 \\ E_y^2 \\ E_z^2 \\ 2E_yE_z \\ 2E_xE_z \\ 2E_xE_y \end{pmatrix} \tag{4.1.13}$$

and explicitly computing the right hand side

$$\begin{pmatrix} P_x^{(2)} \\ P_y^{(2)} \\ P_z^{(2)} \end{pmatrix} = \begin{pmatrix} 2d_{31}E_xE_z - 2d_{22}E_xE_y \\ d_{22}\left(E_y^2 - E_x^2\right) + 2d_{31}E_yE_z \\ d_{31}\left(E_x^2 + E_y^2\right) + d_{33}E_z^2 \end{pmatrix} \tag{4.1.14}$$

## 4.2 Phase Matching

The electromagnetic field we obtain for a certain point in space is the sum of fields generated in different points of the crystal. It is critical to obtain efficient conversion that the single contributions interfere constructively, which means that the nonlinear polarization field must be in phase with the second harmonic electric field propagating from other points of the crystal. For a plane wave the simple condition $\mathbf{k}_{pol} = \mathbf{k}^{(2\omega)}$ is sufficient. From (4.1.5) we see clearly that the dielectric polarization wavevector is two times the fundamental wavevector $\mathbf{k}_{pol} = 2\mathbf{k}^{(\omega)}$ and the required phase matching condition is

$$2\mathbf{k}^{(\omega)} = \mathbf{k}^{(2\omega)} \tag{4.2.1}$$

If both the fundamental electric field and the induced dielectric polarization lay on the same plane (and so the second harmonic light generated in the medium) the dispersion of the material prevents the condition (4.2.1) from happening. Indeed, while the $k$-vector of the polarization is twice the one of the input signal (assuming both propagating along the same direction)

$$2k^{(\omega)} = 2n(\omega)\frac{\omega}{c} \tag{4.2.2}$$

and the frequency of the generated light is double the frequency of the input signal $\omega_2 = 2\omega$, for the second harmonic light we have

$$k^{(2\omega)} = n(2\omega)\frac{2\omega}{c} \tag{4.2.3}$$

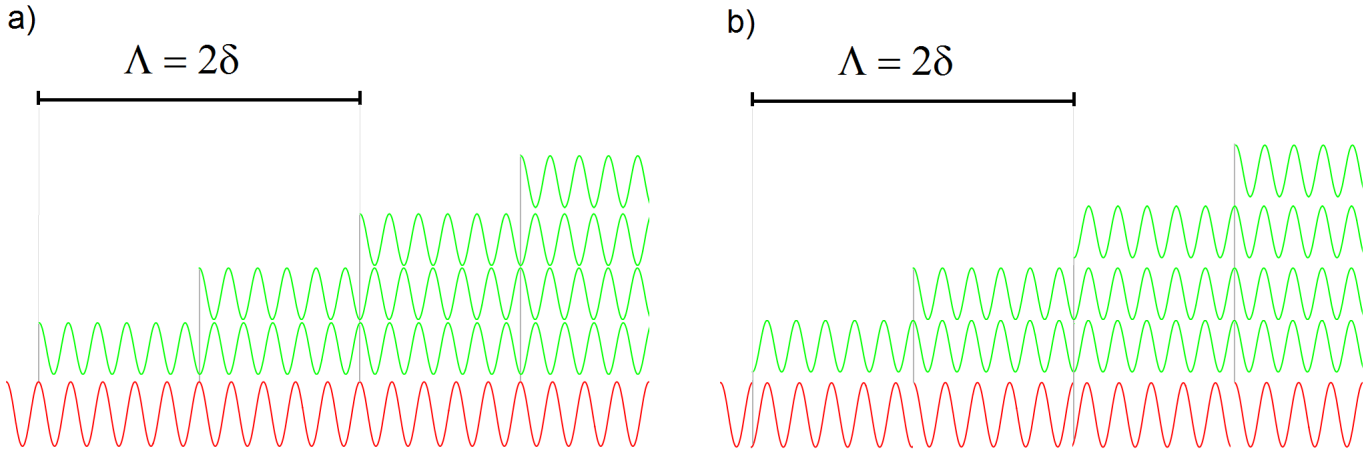


Figure 4.2.1: Periodic Poling Effect in absence of birefringent phase matching. The red line represents the second order induced dielectric polarization, the green lines represent the second harmonic contributions generated in points distanced $\delta = \pi/\Delta k$. The poling period to achieve QPM is indicated as $\Lambda$ **a)** In absence of poling, the second harmonic light generated in points distanced $\delta$ interfere destructively. **b)** In presence of poling the second order polarization of the medium is reversed , adding a $\pi$ phase on the generated light that fixes the phase mismatch.

the corresponding wavenumber mismatch $\Delta k = k^{(2\omega)} - 2k^{(\omega)}$ is then given by

$$\Delta k = \frac{2\omega}{c}\left[n\left(2\omega\right) - n\left(\omega\right)\right] \tag{4.2.4}$$

which is different from 0 unless $n(\omega) = n(2\omega)$. For a given $\Delta k$ a coherence length $l_c = \frac{2\pi}{\Delta k}$ can be defined, as the maximum useful crystal length to generate the second harmonic signal (Figure 4.2.1a). Calculating the coherence length for stoichiometric Lithium Tantalate at room temperature using Sellmeier Equation [37] to estimate refraction indices for our wavelengths of interest (1064 nm for the fundamental and 532 nm for the second harmonic) we obtain $l_c \simeq 8\,\mu m$, and phase mismatch correction methods are necessary to avoid destructive interference.

The effect of phase mismatch can be calculated in a more quantitative way. To reduce the burden of formalism let's take the electric field defined in (4.1.4) and a material with $C_{3v}$

symmetry. From (4.1.14), since $E_x = E_y = 0$ the second order medium polarization is simply

$$\begin{pmatrix} P_x^{(2)} \\ P_y^{(2)} \\ P_z^{(2)} \end{pmatrix} = \begin{pmatrix} 0 \\ 0 \\ d_{33} E_z^2 \end{pmatrix} \tag{4.2.5}$$

The second harmonic frequency component of the polarization enters in the Maxwell Equations, then in the wave equations, through the relation

$$\mathbf{D} = \epsilon_0 \mathbf{E} + \mathbf{P} \tag{4.2.6}$$

in the approximations of lossless medium, plane waves, slow variation of the second harmonic field amplitude and ignoring pump depletion, from time dependent Maxwell Equations inside the material and a nonlinear polarization in the form (4.2.5) the amplitude of the $2\omega$ electric field component follows the equation [33]

$$\frac{dE_z^{(2\omega)}(x)}{dx} = -i\omega\sqrt{\frac{\mu_0}{\epsilon}} d_{33} \left(E_z^{(\omega)}\right)^2 e^{i\Delta k\, x} \tag{4.2.7}$$

that can be simply integrated with the boundary condition requiring no second harmonic input $E^{(2\omega)}(x=0) = 0$

$$E_z^{(2\omega)}(x) \propto \frac{e^{i\Delta k\, x} - 1}{i\Delta k} \tag{4.2.8}$$

from which the second harmonic intensity at position $x$ is proportional to the factor

$$I^{(2\omega)}(x) \propto x^2 \frac{Sin^2\left(\frac{\Delta k}{2} x\right)}{\left(\frac{\Delta k}{2} x\right)^2} \tag{4.2.9}$$

in case $\Delta k \to 0$ the intensity grows quadratically in the crystal $I(x) \propto x^2$, while in presence of phase mismatch the intensity fluctuates between zero and its maximum value, with period equal to the coherence length $l_c$. The comparison is shown in Figure 4.2.2.

**Achieving Phase matching with birefringent crystals: Critical and non-critical Phase matching** The general idea behind birefringent phase matching is to generate second harmonic light polarized in a different direction with respect to the fundamental, and exploit the anisotropy of the crystal to correct for the phase mismatch. To make a clear example let's take an uniaxial crystal, that is characterized by the presence of an optic axis (that we take in the $z$ direction); for light polarized in the $z$ direction the corresponding index of refraction is $n_e$ (extraordinary index of refraction), while for the other two directions it is $n_o$ (ordinary index of refraction). The first consequence is that for light beams propagating orthogonally with respect to the optic axis there are two distinct polarization directions dictated by the crystal structure, that show different phase velocities. On the contrary for beams propagating in a direction parallel to the optic axis the electric field is always polarized in an ordinary direction - there is no dispersion to take advantage of to achieve phase matching.

In the intermediate situation, where the propagation direction has an angle $\theta$ with respect to the optic axis ($\theta$ between 0 and $\pi/2$) the extraordinary direction lays on the plane spanned by the propagation direction and the optic axis, and the effective angle-dependent extraordinary index of refraction is defined by

$$\frac{1}{n_e^2(\theta)} = \frac{cos^2(\theta)}{n_o^2} + \frac{sin^2(\theta)}{n_e^2} \tag{4.2.10}$$

with $n_e(0) = n_o$ and $n_e(\pi/2) = n_e$ as previously stated. Choosing if the fundamental beam is to be polarized along the ordinary or extraordinary direction, depends on the dispersion properties of the material and the sign of $n_e - n_o$. For negative crystals with normal dispersion (the refractive index increases with frequency) phase matching can be achieved with a fundamental ordinary beam and an extraordinary second harmonic. The other parameter that can be used to tune the difference in indices of refraction is the temperature: if the temperature dependencies of the ordinary and extraordinary indices of refraction are different (and usually are) they can be exploited to a certain extent. The condition (4.2.4) can be taken for a fundamental ordinary beam and an extraordinary second harmonic

$$\Delta k = \frac{2\omega}{c}\left[n_e(T, \theta, 2\omega) - n_o(T, \omega)\right] \tag{4.2.11}$$

For $\theta \neq \pi/2$ the phase matching is defined "critical", and has several disadvantages. First of all the phase matching condition is strongly angle-dependent, and small deviations can have a dramatic impact on efficiency. Also, the tunability range is limited, and for nonlinear non-birefringent crystals this method can't be used. Another problem with critical phase matching is the walk-off of the second harmonic generated light with respect to the fundamental induced by the birefringence, that limits the useful interaction length and contribute to distort the second harmonic beam shape. The last problem is that, exactly as the index of refraction also the effective second order tensor parameters that contribute to the generated light (and so the efficiency) are angle dependent, and since different angles are required to compensate phase mismatches for different wavelengths, the obtainable conversion efficiency for a certain material is wavelength-dependent. Some of these problems, including the birefringent walk-off and the strong dependence on the angle are resolved for $\theta = \pi/2$, tuning the temperature. In that case the phase matching is defined "non-critical", but still presents some issues, including the impossibility to exploit materials with large $\chi_{iii}$ coefficients or nonlinear materials that exhibit no birefringence. The kind of phase matching technique I described is referred to as "Type I" PM when the fundamental signal share no polarization component with the second harmonic (such as given by$\chi_{ijj}$ terms with $i \neq j$); another possibility is "Type II" PM when the fundamental has one component in common with the second-harmonic ($\chi_{iij}$ terms with $i \neq j$).

**Quasi-Phase-Matching** Periodic Poling was first proposed [34] as a possible phase correction scheme. It consists in the subdivision of the crystal in domains with inverted sign on the relevant $d$ coefficient to induce additional $\pi$ phase mismatches in the polarization vector with a defined periodicity. This subdivision can be obtained with a wide range of techniques, both during the growth or after. The advantages connected to this kind of phase matching are the possibility to exploit large diagonal terms of the $\chi^{(2)}$ tensor, the possibility to engineer poling domains allows to exploit the whole transparency region of the material for non-critical phase-matching (absence of spatial walk-off and angle-tuning instability), and the possibility to exploit non birefringent materials.

The typical situation is shown in Figure 4.2.1 and the obtained result is defined Quasi-Phase Matching (QPM). Let's suppose to have a fundamental frequency signal with the

electric field direction aligned in the optic axis direction ($\hat{z}$) propagating in direction $\hat{x}$ in a transparent $C_{3v}$ material. From (4.1.14) we get simply ($E_x = E_y = 0$)

$$P_z = d_{33} E_z^2 \tag{4.2.12}$$

and $P_x = P_y = 0$. It's not possible to have the $P_z$ dielectric polarization in phase with the second harmonic field oscillating in the same direction, for the already mentioned dispersion of the material. If $\delta$ is the propagation distance where the accumulated phase mismatch is $\pi$, reversing the crystal structure (inverting the sign of the nonlinear susceptibility tensor) would add another $\pi$ phase on the dielectric polarization of the medium, forcing it back in phase with the second harmonic light. More formally if $\Lambda = 2\delta$ is the poling period we get a QPM condition relating the poling period, the wavelengths (in vacuum) and the refraction indexes

$$\Lambda \cdot \Delta k = \Lambda \left[ \frac{2\pi n\left(\lambda/2\right)}{\lambda/2} - 2 \cdot \frac{2\pi n\left(\lambda\right)}{\lambda} \right] = 2\pi \tag{4.2.13}$$

that carrying simple reductions can be written

$$\Lambda - \frac{\lambda}{2\left[n\left(\lambda/2\right) - n\left(\lambda\right)\right]} = 0 \tag{4.2.14}$$

A more general condition than (4.2.14) is often found in literature, that includes the possibility that the phase mismatch in each domain is a multiple of $\pi$ is often found in literature, and corresponds to an higher order matching condition $\Lambda = \frac{2\pi}{\Delta k} m$, where $m$ is an integer and it is defined as the QPM order. This possibility extends the frequency choice for a given poled crystal, however it is less efficient.

The choice of temperature is critical to achieve QPM. Temperature acts twofold on the QPM condition (4.2.14) , from one side it changes the domain length (due to thermal expansion) while on the others changes the material indices of refraction, both for fundamental frequency and for second harmonic. To estimate the phase matching temperature empirical relationships are used, both for crystal expansion and refractive index (Sellmeier Equation) [37].

Of course, since this correction scheme operates at fixed intervals and not continuously (there is still some phase mismatch inside each domain) the efficiency is lower than birefrin-

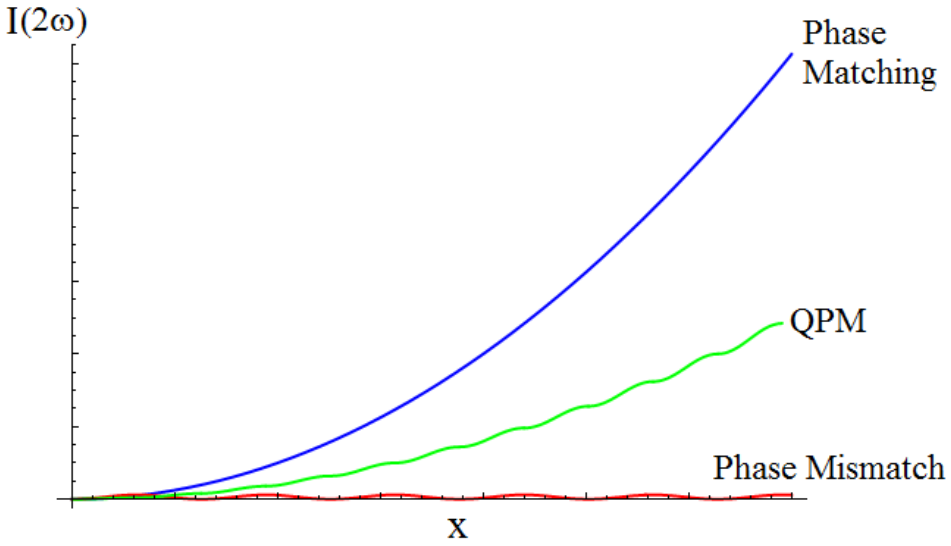


Figure 4.2.2: Intensity of second Harmonic generated light in function of position (arbitrary units) inside the crystal. The comparison is between perfect phase matching (blue line), QPM (green line) and phase mismatch (red line).

gent phase matching.

The equation (4.2.7) now contains a periodic $g(x)$ function with periodicity $\Lambda = 2\delta$.

$$E^{(2\omega)}(x) \propto \int_0^x \mathrm{d}\bar{x} g(\overline{x}) e^{-i\Delta k \bar{x}} \tag{4.2.15}$$

where, for every integer $n$

$$\begin{cases} g(x) = -1 & (2n-1)\delta < x < 2n\delta \\ g(x) = +1 & 2n\delta < x < (2n+1)\delta \end{cases} \tag{4.2.16}$$

expanding in Fourier series and calculating Fourier the coefficients

$$g(x) = \sum_m g_m e^{iG_m x} = -i \sum_m \frac{2}{\pi m} e^{iG_m x} \tag{4.2.17}$$

where $G_m = \frac{2\pi}{\Lambda} m$ are the reciprocal lattice vectors of the poling grating, and $m$ is integer

and corresponds to the phase matching order mentioned above. Then (4.2.15) becomes

$$E^{(2\omega)} \propto \int_0^x \mathsf{d}\bar{x} \sum_m \frac{2}{\pi m} e^{-i(\Delta k - G_m)\,\bar{x}} \tag{4.2.18}$$

The $m$-th order QPM condition is $\Delta k - G_m = 0$. If that condition is satisfied the $m$-th contribution to the electric field in (4.2.18) builds up constructively in the crystal, and the associated intensity can be directly compared with birefringent phase matching output intensity

$$\frac{I_m^{QPM}(x)}{I(x)} = \frac{x^2 \left(\frac{2}{\pi m}\right)^2}{x^2} = \frac{4}{\pi^2 m^2} \tag{4.2.19}$$

showing the reduced conversion efficiency with increasing QPM order.and for $m = 1$ the reduction factor of $(4/\pi^2)$with respect to the birefringent case. Nevertheless Lithium Tantalate is reported to have a strong $d_{33}$ coefficient [38] that can't be exploited in birefringent phase matching, and its comparatively high value more than compensate the lower efficiency of QPM at first order.

## 4.3 SHG with Gaussian laser beams

For the results obtained so far it would appear that the most efficient way to generate double frequency light would be to focus as tightly as possible a laser beam to get advantage of the quadratic behavior of the generated power with respect to the intensity of the fundamental. The fallacy in this reasoning lays into not taking into consideration that reducing the waist of a laser beam reduces also it's Rayleigh length - the length within it can be considered collimated, to a good approximation. Reducing that parameter below a something of the scale of the crystal length reduces the volume where efficient conversion is obtained inside the crystal itself and the optimal focusing condition is a tradeoff between these two effects. This and other issues, were taken into consideration by Kleinman and Boyd [39] for a birefringent crystal, identifying a set of experimental parameters suitable for single mode Gaussian beams. They obtained for the second harmonic generated power $P_2$ in function of the incident one

$P_1$

$$P_2 = KP_1^2 lk_1 e^{-\alpha' l} \cdot h\left(\sigma, \beta, \kappa, \xi, \mu\right) \tag{4.3.1}$$

where $K$ is a constant depending on the effective nonlinear coefficient involved in the conversion, on the indices of refraction and on the frequencies, $l$ is the length of the crystal, $k_1$ is the fundamental wavevector modulus in the medium and $\alpha' = \alpha_1 + \frac{1}{2}\alpha_2$ accounts for absorption coefficients . Regarding the function $h\left(\sigma, \beta, \kappa, \xi, \mu\right)$, it is a function of the phase mismatch (that is proportional to the parameter $\sigma$), the absorption ($\kappa$) , the double refraction effect ($\beta = B\xi^{-1/2}$), the strength of focusing ($\xi$) and the focal position with respect to the crystal center ($\mu$). The focusing parameter is defined as

$$\xi = \frac{l}{2z_R} \tag{4.3.2}$$

where $z_R$ is the Rayleigh Length of the Gaussian beam, that can be expressed in function of the waist of the beam in the focal point $w_0$ and the wavelength of the beam inside the medium $\frac{\lambda}{n(\omega)}$

$$z_R = n\left(\omega\right) \frac{\pi w_0^2}{\lambda} \tag{4.3.3}$$

Equation (4.3.2) is sometimes written in literature using $2z_R = b$.

Setting the absorption coefficient to zero and the focus of the beam in the center of the crystal, and optimizing the phase mismatch parameter $\sigma$ for the given value of $B$ the function $h\left(\sigma_{opt}, B, \xi\right)$ exhibits a maximum in function of $\xi$. In absence of double refraction this value is $\xi = 2.84$, while for $B \neq 0$ this optimal value is reduced (meaning that the focusing of the fundamental beam should be reduced to compensate for birefringent walk-off) and the maximum value of $h$ is reduced (the maximum obtainable efficiency is reduced). Although being explicitly addressed to the birefringent crystal case, this result can be used for periodically poled crystals [40], assuming $B = 0$.

The efficiency may vary appreciably with the beam mode quality. An extension of this approach for elliptical beams is found in literature [41], where it is shown that in presence of birefringent walk-off, preparing the beam in a suitable elliptical shape could be advantageous.

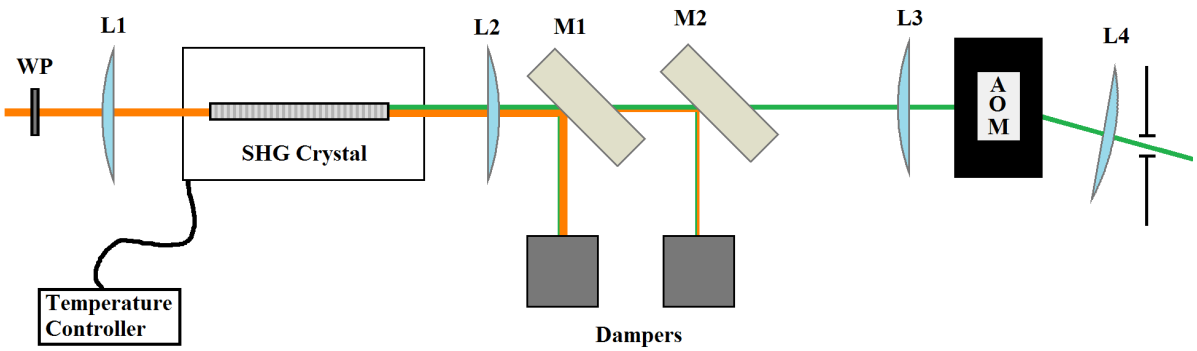


Figure 4.4.1: A sketch of the experimental apparatus

## 4.4 Experimental apparatus

A simple schematization of the experimental section dedicated to the SHG crystal is shown in Fig.4.4.1. The actual displacement on the table is different and features more non essential optics (for example more mirrors) but they were added to fit with the rest of the experiment.

An infrared collimated beam ($\lambda = 1064$ nm) generated by a Mephisto Mopa [specific model and so on] , whose polarization is selected with a $\frac{\lambda}{2}$ wave-plate (WP), is focused by the lens L1 ($f = 40$ mm) inside the crystal (HC Photonics, MgO:sPPLT, 1 x 1 x 20 mm) where the second harmonic signal ($\lambda = 532$ nm) is generated. The crystal is inside an oven whose temperature is kept stabilized within 0.1 °C by a controller, both supplied from the same company HCP . The L1 lens is mounted on a Newport steel translational stage to optimize the focusing point inside the crystal. A second lens L2 ($f = 50$ mm), coated for both wavelengths, is put at the output of the crystal fixed at a proper distance from the center of the crystal to recollimate the output beams. Then two harmonic separator mirrors M1 and M2 (Lambda Research Optics HHS - R1064/T532-45) are used in sequence to filter out the infrared signal from the green. Each one is reported to have a minimum reflectivity of 99.5% , so for a single mirror and 30W fundamental power a maximum leak of 150 mW was expected. To further reduce this we decided to add the second mirror, adding another maximum loss of 15% in the green signal, as reported in the data from the company. Then a telescope (L3 and L4 $f = 300$ mm) is used to focus the second harmonic beam into an acousto-optic modulator (AOM, Crystal Technology 3200-120) and recollimate the output beam, then damping all the

modes apart the first diffracted. The fraction of the first order diffracted power is selected changing the radio-frequency amplitude input of the AOM, which is analogically controlled with a driver employing VCOs (Voltage-controlled oscillators) [models?]

## 4.5 Optimization procedure

The optimization has been carried experimentally; the parameters I could optimize were the waist of the beam in the focal point inside the crystal (selecting the L1 lens focal length among the available ones), the position of the focal point (changing the position of the L1 lens), the alignment of the crystal respect to the beam (it's mount allows small rotations and translations in both vertical and horizontal axes) and the phase matching temperature . While polarization direction choice and alignment optimization are pretty straightforward, for the beam waist and phase matching temperature it has been useful to estimate their optimal value before mounting the system to have a good starting point, and then fine-tuning to maximize the efficiency.

**Phase-Matching temperature** To have a clue about the starting phase matching temperature I computed both the thermal expansion of poling domains and the solutions of the Sellmeier Equation with the phenomenological parameters given in [37], in dependence of temperature. Then I numerically computed the right hand side of (4.2.14) looking for a zero. This was found at about 56 °C. Starting from that point, during the experimental optimization I found the best temperature was lower and slightly dependent on the fundamental beam power (47.7 °C for 30.8W pump). This difference in temperature can be dependent on specific crystal parameters deviations, while the dependence on fundamental power could be explained with absorption induced thermal effects [40].

**Beam Waist** The optimal beam waist was computed by the focusing parameter definition (4.3.2), equating it to the optimal value $\xi_{opt} = 2.84$, whose corresponding optimal waist is about 23.6 $\mu m$ inside the crystal (computing the index of refraction from the Sellmeier equation at the Phase Matching temperature) . I proceeded observing the beam waist of the fundamental beam with a CCD camera before mounting the crystal, obtaining the most

| $f$ | $P_{IN}\,(W)$ | $P_{OUT}\,(mW)$ | $\%Norm\,(W^{-1}cm^{-1})$ |
|---|---|---|---|
| 30 | 4 | 126 | 0.39 |
| 40 | 4 | 157 | 0.49 |
| 50 | 4 | 145 | 0.45 |

Table 4.1: Low-power efficiencies obtained for different focusing lenses

suitable waist among the available lenses with the 40 mm lens. Then calculating the effect of the crystal on the focus position using the ABCD propagation matrices and the calculation of the index of refraction allowed to estimate the best distance from the crystal for the L1 lens at about 48 mm. To test the result I measured the efficiency also with one more focusing ($f = 50$ mm) and one less focusing ($f = 30$ mm) lens, ensuring that the chosen lens was really the best among available ones (see Table 4.1).

## 4.6 Results, conclusions and future improvements

Once the system had been optimized I performed a characterization aligning at high power (30.8 W), maximizing the conversion efficiency with respect to lens distance and oven temperature. Then for subsequent measurements I decreased the input power, then maximized again re-adjusting lens position and QPM temperature. This last step was critical especially at higher powers than 10-15 W where I observed significant drops in normalized efficiency (efficiency per unit power per unit length).

Therefore from low powers to about 12-15 W I observe a linear growth in conversion efficiency (equivalent to quadratic output power respect to input or constant normalized efficiency). Beyond that point the efficiency started saturating. The maximum power measured was 5.55 W for 30.8 W input

The collected data shows both the aforementioned decrease in phase matching temperature with the fundamental power, and the efficiency saturation. This last effect is attributed in addition to thermal phase mismatch effects, to pump depletion (the power of the pump is reduced from the conversion while propagating inside the crystal) and back-conversion [40]. These measurements show a slightly lower efficiency than the ones in Table 4.1. This is because they were taken in different days, and I was able to improve the alignment. Also

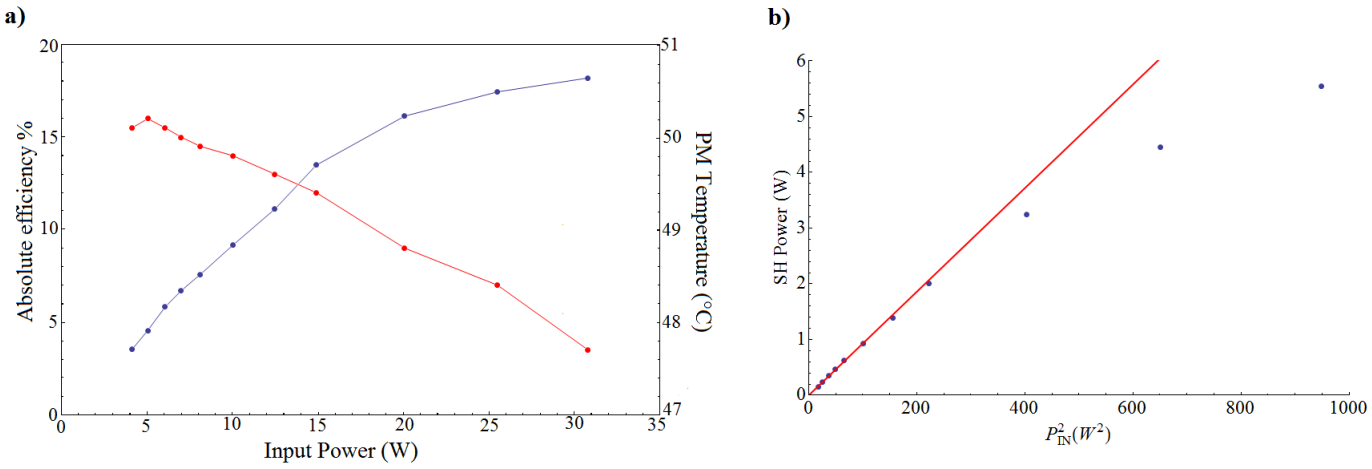


c)

| PMTemp(°C) | $P_{IN}$ (W) | $P_{OUT}$ (W) | %Norm Eff ($W^{-1}cm^{-1}$) | % Eff |
|---|---|---|---|---|
| 47,7 | 30,8 | 5,55 | 0,29 | 18,02 |
| 48,4 | 25,50 | 4,45 | 0,34 | 17,45 |
| 48,8 | 20,07 | 3,24 | 0,4 | 16,14 |
| 49,4 | 14,90 | 2,01 | 0,45 | 13,49 |
| 49,6 | 12,48 | 1,39 | 0,45 | 11,12 |
| 49,8 | 10,01 | 0,92 | 0,46 | 9,16 |
| 49,9 | 8,12 | 0,62 | 0,47 | 7,59 |
| 50,0 | 7,00 | 0,47 | 0,48 | 6,71 |
| 50,1 | 6,06 | 0,35 | 0,48 | 5,83 |
| 50,2 | 5,04 | 0,23 | 0,45 | 4,56 |
| 50,1 | 4,13 | 0,15 | 0,43 | 3,54 |

Figure 4.6.1: **a)** Absolute conversion efficiency % (Blue) in function of fundamental beam power, and the corresponding QPM temperature (Red) **b)** The output second harmonic power in function of the squared power of the fundamental (Blue). The saturation effect is shown fitting the first six points to a line (Red) **c)** The measured data and calculated efficiencies

the obtained normalized efficiency is lower than what has been reported in literature with a similar crystal [40]. This might be due to the beam quality, that showed deviations from the Gaussian shape. This issue was not not addressed for now since the generated output is more than satisfactory for our present practical purpose.

Another issue is the temperature stabilization. The oven and controller supplied by the company is a passive system that is only capable to heat up the sample when it dissipates heat,

oscillating around the set-point. This leads to observed fluctuations in the output generated power of about 10% in less than one minute period. This situation will be improved enclosing the oven in a specifically designed box to reduce the dissipation of heat, before seeing if other stabilization mechanisms are needed. The reported data are always taken at the maximum of these oscillations to compare reliably the measurements and because these points correspond to the best phase-matching temperature.

# Chapter 5

# Experimental results

In this Chapter I will discuss the relevant experimental results we obtained during my thesis period. The efforts were directed towards the characterization of the system's performance at the moment, including coherence time and temperature of the system. For the first time we observed a remarkable coherence time of about $200\,ms$ both for number and phase evolution. From these measurements we inferred the values of the Bose-Hubbard Hamiltonian imbalance and tunneling coefficients corresponding to our experimental choices. Another important aspect is that both procedures are part of the Mach-Zehnder interferometric sequence: achieving a good degree of control and fidelity for population evolution is required to employ the two atomic beam splitter procedures without introducing errors, while the importance of control over the phase accumulation sequence is related to the the fact that it corresponds to the effect of the external perturbation we want to measure; the effect of noise on the energy imbalance between the wells or positioning errors in the relative position of the two optical lattices affect directly the interferometric measurement. For this reason these simple measurements are the testbed for the complete interferometer performances

To give an estimation of the condensate temperature we exploited the effect of thermal fluctuation on the system coherence. This method can be applied for very low temperatures, where the thermal fraction of atoms is negligible (and a direct measurement is impossible) but its effect on the system coherence can still be observed. This is a very important parameter to keep into consideration for interferometric applications, as it was already discussed in Subsection 1.3.4.

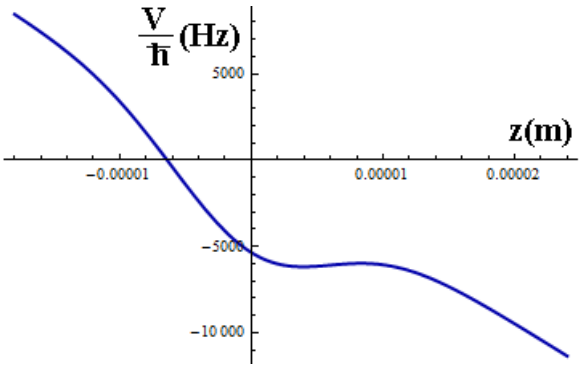


Figure 5.1.1: Plot of a tilted trap potential in the form of (5.1.1).

## 5.1 Optimization of the evaporation sequence

For interferometric coherence the control over the preparation of the state is of capital importance: the thermal occupation of excited levels reduces the coherence of the system and, for high enough temperatures, even break the two mode approximation. While for a system of interacting atoms these excitations include collective modes of the condensate, tuning the interatomic interactions to zero ensures the absence of these excitations, and removing the trap excited levels guarantees that our system will be effectively in the ground state. To obtain this result the final part of the evaporation is achieved in a tilted Gaussian confining trap, where the tilting is due to the effect of a tunable linear potential. In this configuration atoms in the bound states can tunnel out of the trap, and the lifetime of each bound state depends on the specific potential shape. To estimate the optimal experimental parameters a 1D simulation of the lifetimes of bound states has been performed for different parameters, using the WKB method for a simple 1D model, following the approach found in [46]. With this simplification the potential of the trap in $\hat{z}$ direction in the focal region can be written as

$$V(z) = \frac{U_0}{w_0^2} e^{-2\frac{z^2}{w_0^2}} - \left(mg - \mu \frac{\mathrm{d}B}{\mathrm{d}z}\right) z = \frac{U_0}{w_0^2} e^{-2\frac{z^2}{w_0^2}} - \gamma z \tag{5.1.1}$$

where $\gamma$, $U_0$ and $w_0$ are the experimentally tunable parameters. An example is shown in Figure 5.1.1. For a given shape of the potential and a given energy value $E$, the condition $E > V(z)$ identifies the classically allowed region, while for $E < V(z)$we have the classically

forbidden one. We define for the allowed region

$$k(z) = \sqrt{\frac{2m}{\hbar}(E - V(z))} \tag{5.1.2}$$

and its integral

$$L(E) = \int_{E>V(z)} k(z)\,\mathrm{d}z \tag{5.1.3}$$

and correspondingly in the forbidden region

$$\kappa(z) = \sqrt{\frac{2m}{\hbar}(V(z) - E)} \tag{5.1.4}$$

and

$$\Theta(E) = \int_{E<V(z)} \kappa(z)\,\mathrm{d}z \tag{5.1.5}$$

Bound states are found with the condition to have nodes at the boundaries of the allowed region

$$L(E_B) = \left(n + \frac{1}{2}\right)\pi \tag{5.1.6}$$

For these states the Gamow factor, that is one of the quantities defining the lifetime of the state in the trap, corresponds to the probability for a particle with energy $E$ to penetrate the potential barrier

$$G(E) = e^{-2\Theta(E)} \tag{5.1.7}$$

and accounts for an exponential decrease of the wavefunction amplitude in the forbidden region. The other important quantity is the derivative $\hbar\frac{\partial L(E)}{\partial E}$ that can be interpreted as the rate with which the particle hits the potential barrier, being the same quantity for an harmonic potential equal to $\omega^{-1}$. The state lifetime in the trap is thus

$$\tau = \frac{\hbar}{G(E)}\frac{\partial L(E)}{\partial E} \tag{5.1.8}$$

The ground state and the first excited state energies and their lifetimes in trap have been calculated for different parameters. In Figure 5.1.2a, as an example, the energy levels are

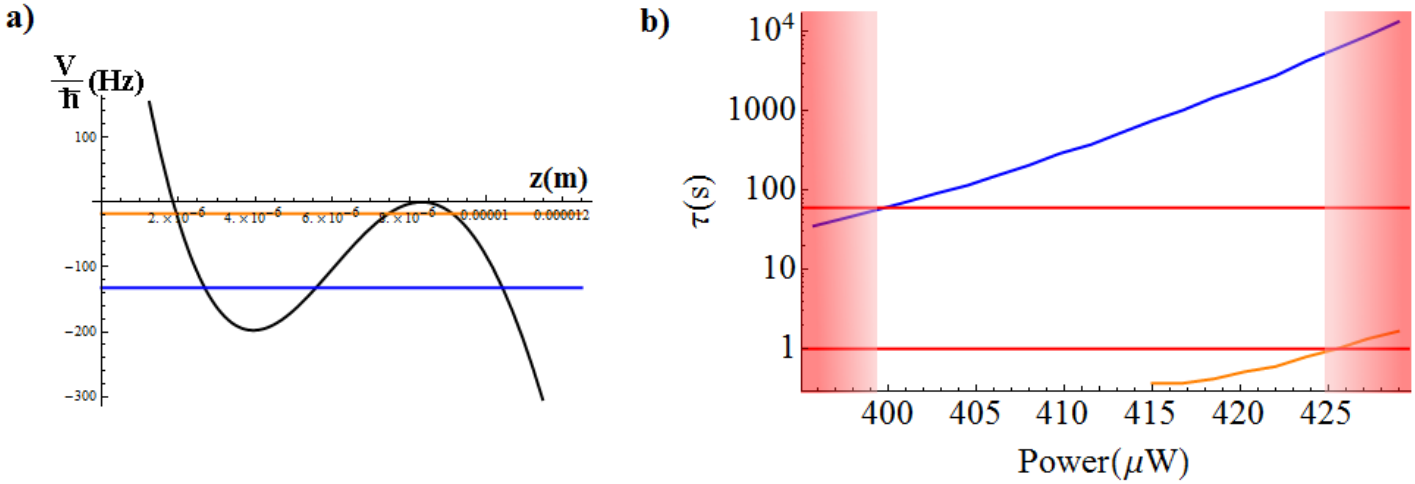


Figure 5.1.2: **a)** An example of confining potential (black) for $w_0 = 12\,\mu m$, $\gamma = 0.5\,g$, $P = 420\,\mu W$ and the calculated ground state (blue) and first excited level (orange) levels **b)** Lifetimes of the ground (blue) and first excited (orange) states calculated for the same values of $w_0$ and $\gamma$ for different values of the power $P$. To compute the required stability the width of the acceptance region (in white) is calculated as the region where both $\tau_G \geq 60\,s$ and $\tau_E \leq 1\,s$ (both thresholds are indicated as red lines in the figure)

shown for $P = 420\,\mu W$, $\gamma = 0.5\,g$, $w_0 = 12\,\mu m$. We searched for the condition that allows us to selectively spill out excited atoms from the trap, requiring long lifetimes for the ground state ($\tau_0 \geq 60\,s$) and short lifetimes for the first excited state ($\tau_1 \leq 1\,s$). For fixed waist $w_0$ and gravity gradient $\gamma$ we calculate the required relative power stability of the beam as

$$\frac{\Delta P}{\bar{P}} \tag{5.1.9}$$

where $\Delta P$ is the ranges of power where the both conditions on lifetimes are simultaneously satisfied (the white region in Figure 5.1.2b) and $\bar{P}$ is the mean value of the interval.

The resulting stability, mean power values and potential trapping frequency for several $w_0$ and $\gamma$ (See Table 5.1) have been calculated. The general trends that can be inferred from the numerical calculations are an increase of stability for tighter beam focusing and decreasing the gravitational gradient along with the trapping beam power. These changes however, while maximizing the stability, reduce the trapping frequency of the potential, increasing the

| $w_0\ (\mu m)$ | $\gamma\,(g)$ | $\nu_T\,(Hz)$ | $\bar{P}\,(\mu W)$ | $\frac{\Delta P}{\bar{P}}\,(\%)$ |
|---|---|---|---|---|
| 10 | 0.5 | **225** | 256 | 6.43 |
| 12 | 0.5 | **200** | 413 | 6.14 |
| 12 | 0.1 | 100 | 100 | 7.5 |
| 12 | 0.01 | 35 | 15 | 13.5 |
| 18 | 0.75 | **190** | 1945 | 3.6 |
| 18 | 0.15 | 90 | 410 | 6.14 |
| 18 | 0.015 | 30 | 55 | 7.5 |

Table 5.1: Some numerically calculated values of stability and trapping frequency for different experimental parameters. The highlighted values of frequency satisfy the constraint on the trapping frequency to ensure adiabaticity when rising up the trapping beam power at the end of the evaporative sequence.

timescale to remain adiabatic when increasing again the trapping potential at the end of the sequence. For this reason we needed a trapping frequency $\nu_T$ of the order of 200 Hz to ensure adiabaticity. Comparing the calculated values in Table 5.1 with$\nu_T \sim 200\,Hz$ emerges that focusing the trapping beam still increases the relative stability, but the gravity gradient must be chosen to ensure the constraint on the trapping frequency instead of maximizing the stability. We focused the beam as much as it was experimentally feasible in our system to a waist of $\sim 10\,\mu m$ and chosen a gravitational gradient of about $0.5\,g$, reducing the excitations.

## 5.2 Rabi oscillations

In this Section, for notational simplicity, I will redefine the tunneling constant defined in (1.3.9) expressing the Bose-Hubbard Hamiltonian in dependence of the experimentally accessible coefficient

$$\frac{2E_J}{N} = \mathcal{J} \tag{5.2.1}$$

The non-interacting atoms are condensed in a well of the primary lattice. Then the barrier is ramped up on one side of the well and, during the the next 50 ms, the barrier is centered (no imbalance) keeping the tunneling at zero. At this point the condensate occupies a single well, or equivalently in the Bloch Sphere formalism, it points to the south pole of the sphere.

Then the tunneling coupling is activated reducing the green lattice beams power in 10

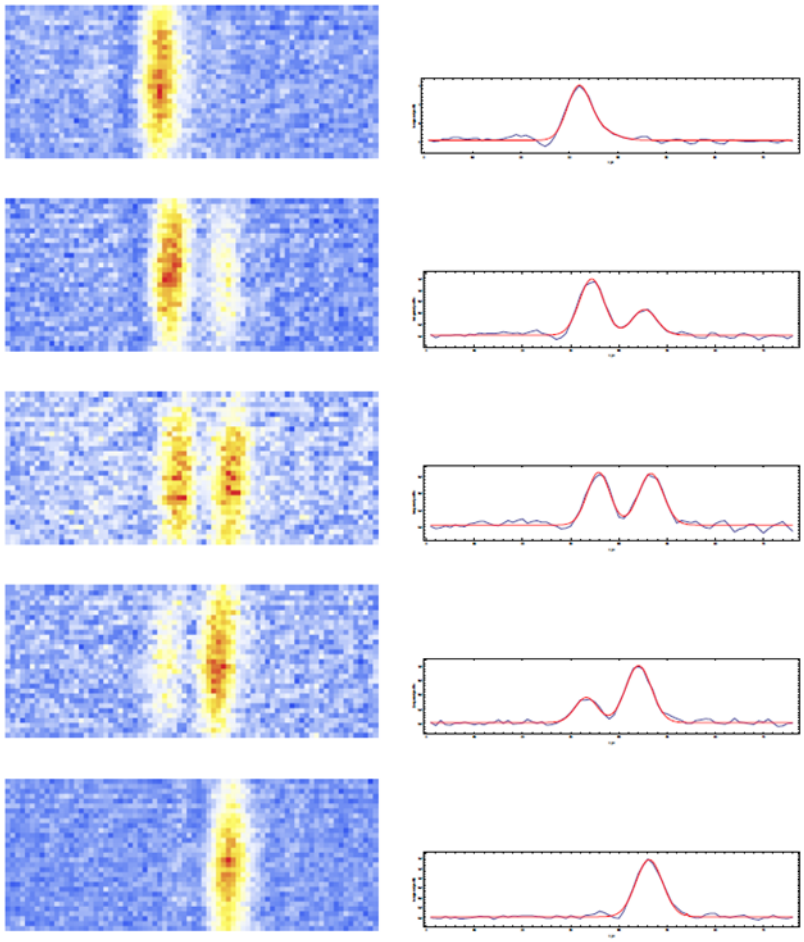

Figure 5.2.1: In-situ images of the atoms (left) in the two potential wells for different tunneling times, showing the oscillating relative population. The images were taken with the high resolution imaging system. The correspondent profiles (right) obtained summing the pixel counts on the vertical direction.

ms, a long enough timescale to not break the adiabaticity but shorter than the tunneling timescale, letting the system evolve under the tunneling Hamiltonian

$$\hat{H} = -\mathcal{J}\hat{J}_x \tag{5.2.2}$$

inducing a precession of the representative angular momentum vector around the $J_x$ axis

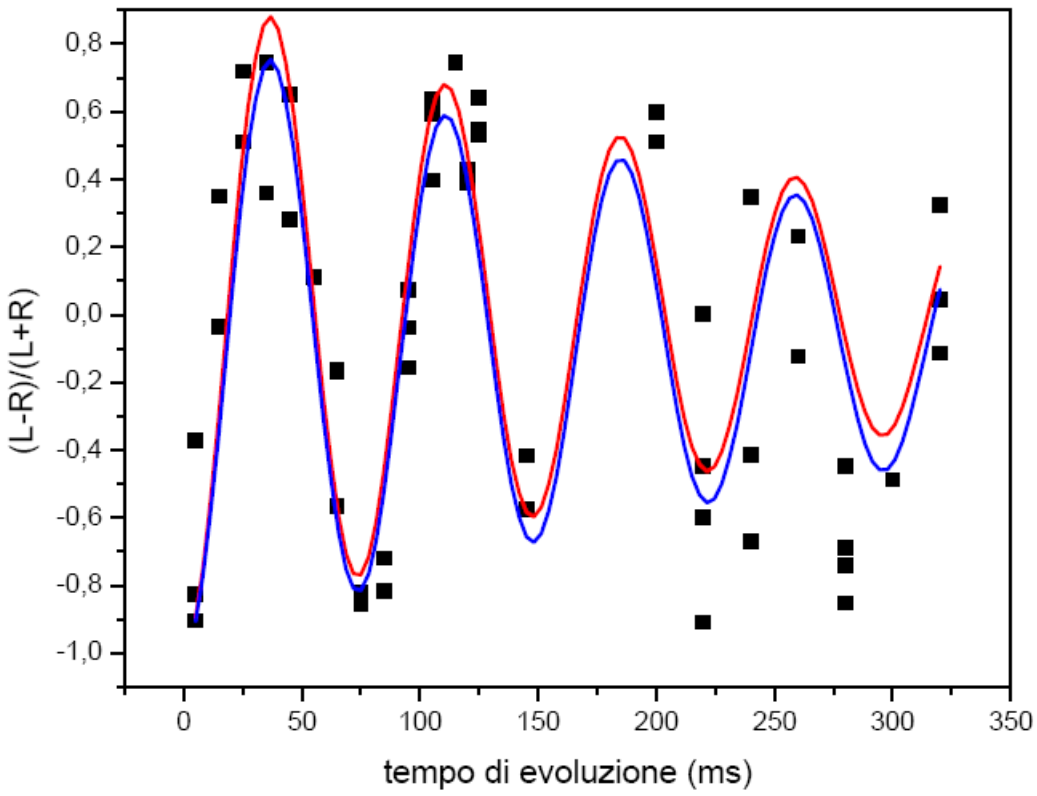


Figure 5.2.2: Results of the fits for Rabi oscillation measurements. The red curve represents the fit result with $f_1(t)$, the blue one represents the result with $f_2(t)$ as fitting function

with period

$$T = \frac{2\pi\hbar}{\mathcal{J}} \tag{5.2.3}$$

and a corresponding relative population of the two wells given by the projection of the vector on the $J_z$ axis

$$\frac{N_L - N_R}{N} = \frac{\langle \hat{J}_z \rangle}{J} = Cos\left(\frac{\mathcal{J}}{\hbar}t\right)$$

After a variable amount of time the central barrier is risen up and the condensate is left to expand in the radial directions, keeping the spatial modes separated with the lattice potential turned on. After the expansion an image is taken. Then we sum up the pixel counts in the

vertical direction and fit the profile with two Gaussian functions, and infer the relative atom number from the integrals of the two profiles.

The effects induced by noise on the tunneling parameter and by the presence of residual energetic imbalance between the two wells are estimated to be the primary causes of a progressive reduction in the contrast of the oscillations and eventually a nonzero mean value of the imbalance. To keep into consideration both possibilities two fitting functions have been used, one that includes only an exponential decay of the contrast

$$f_1(t) = -e^{-(t/\tau_1)} Cos\left(\frac{\mathcal{J}_1}{\hbar}t\right) \tag{5.2.4}$$

the other one predicting the damping to a nonzero value

$$f_2(t) = a\left(1 - e^{-(t/\tau_2)}\right) Cos\left(\frac{\mathcal{J}_2}{\hbar}t\right) - 1 \tag{5.2.5}$$

The results of the fit are shown in Figure 5.2.2. The measured data points were insufficient to discriminate between the two results, that however are consistent within the error. The tunneling energy gave the same result for both fits

$$\mathcal{J}_1 = \mathcal{J}_2 = 2\pi \times (14.25 \pm 0.12)\ Hz \tag{5.2.6}$$

and the obtained exponential decay timescales are

$$\tau_1 = (34 \pm 11) \times 10\, ms \tag{5.2.7}$$

$$\tau_2 = (29 \pm 8) \times 10\, ms \tag{5.2.8}$$

## 5.3 Coherent phase evolution

In this experimental procedure the condensate is prepared in the primary lattice well. The central barrier is ramped up adiabatically, in this way the system is prepared as an eigenstate of the tunneling operator (50:50 coherent population of the two wells). After the tunneling is set to zero an energy imbalance between the two wells is applied for a given amount of time

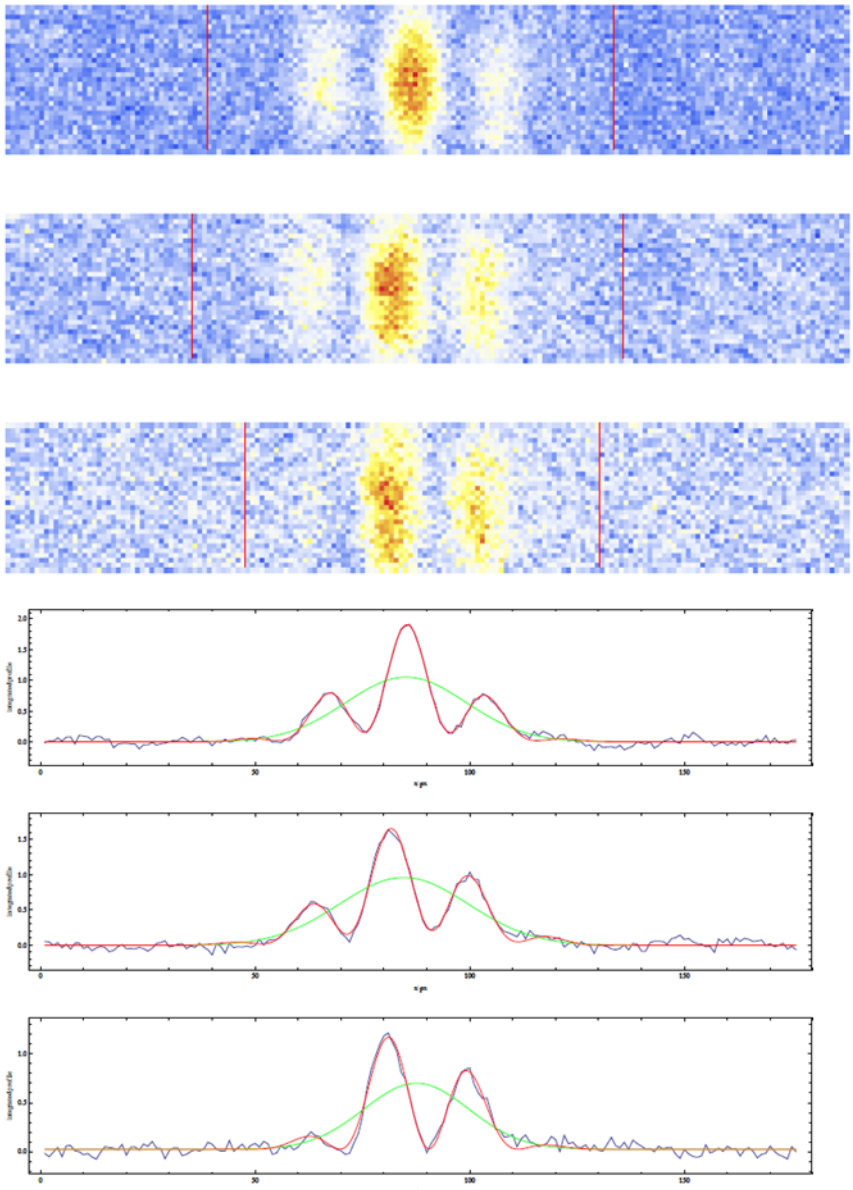

Figure 5.3.1: Observed interference fringes for different phase values (upper images) taken with the high resolution imaging system, and the corresponding profiles (lower)

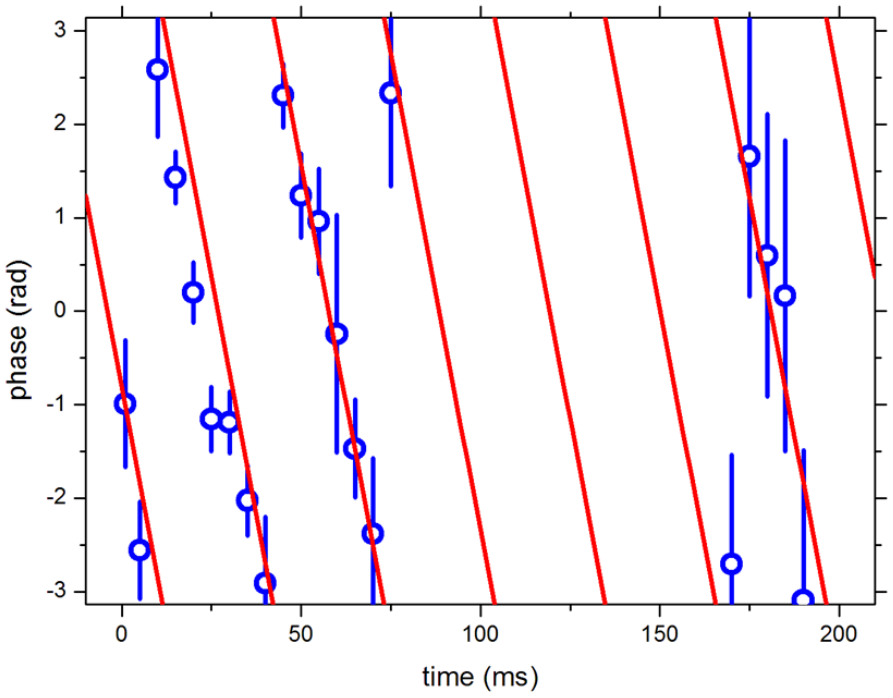


Figure 5.3.2: Phase evolution. Mean values and standard deviations for different phase accumulation times are reported.

$t$, leading to a phase accumulation

$$\Delta\varphi = \frac{\delta}{\hbar}t \tag{5.3.1}$$

Then the trapping potentials are turned of, letting the two modes expand for 4 ms, overlapping. As explained in Section 1.3.6 the phase difference is inferred from the relative position of the interference fringes to the Gaussian envelope function. Also in this case the pixel counts were summed along the vertical direction to construct the profiles showed in Figure 5.3.1, and they were fitted with the function

$$f(x) = B + Ae^{\frac{(x-x_0)^2}{2\sigma_x^2}}\left(1 + C\,Cos\left(\frac{2\pi\,(x-x_0)}{w} + \varphi\right)\right) \tag{5.3.2}$$

where $w$ depends on the expansion time $t_{exp}$ and the distance $d$ between the two spatial modes

$$w = \frac{h}{md} t_{exp}$$

Choosing phase accumulation times separated by 5 ms in the intervals from 0.001 ms to 75 ms and from 170 ms to 190 ms, we obtained the results plotted in Figure 5.3.2. The result shows the expected linear behavior of the accumulated phase with time. The correspondent value of the $\delta$ coefficient is

$$\frac{\delta}{\hbar} = 2\pi \times (31.4 \pm 0.8)\ Hz \tag{5.3.3}$$

From the interference measurements we were able to characterize some of the system's parameters. Having imposed a phase difference of $\Phi = 0.015$ between the two crossing beams of the infrared lattice, from the measured value of the energy imbalance parameter $\delta$ we estimated for the primary lattice

$$V_{IR} = (52 \pm 2)\ nK \tag{5.3.4}$$

Comparing the acquired interference profiles with the time-dependent expansion of two Gaussian packets we estimated the width of the spatial mode before the expansion

$$\sigma_0 = (0.74 \pm 0.08)\ \mu m \tag{5.3.5}$$

and the initial distance between them

$$d = (4.89 \pm 0.06)\ \mu m$$

Once fixed the depth of the primary lattice, the width of the spatial mode in the well depends on the height of the green potential: the higher is the depth, the narrower is the initial atom wavefunction. From a numerical simulation of the trapped BEC we estimate for the green lattice potential [42]

$$V_G = (70 \pm 30)\ nK \tag{5.3.6}$$

Summing the pixel values along the horizontal direction we obtained a profile for the vertical

axis of the image, corresponding to the radial confinement direction. From the width of the profile after expansion we estimated a radial trapping frequency of

$$\omega_T = 2\pi \times (250 \pm 50)\ Hz \tag{5.3.7}$$

**Phase Fluctuations** From the time evolution of the phase standard deviation (Figure 5.3.3) we notice that already in the first 50 ms interval the measured standard deviations are significant and, except for some time values, constant. This indicates the presence of noise in the preparation phase, during the initial splitting of the condensate. For longer times the fluctuations further increase. This can be explained with the presence of noise in the well imbalance coefficient $\delta$, whose effect increases for longer phase accumulation times.

As we can see the lowest measured phase error is of the order of 0.3 rad. The Shot Noise Limit for about 1000 atoms is about 0.03 rad, showing that there are still technical improvements to be done on the system before moving to the quantum-enhanced interferometry. In this regard coherent evolution of the non-interacting system is affected primarily by technical noise, we found an optimal protocol to quantify the degree of improvements that will be achieved in the future.

## 5.4 Coherence thermometry

As discussed in Section 1.3.2, the coherence factor of the system, that is the ensemble average of the operator

$$\alpha = \left\langle \frac{2\hat{J}_x}{N} \right\rangle \tag{5.4.1}$$

corresponds to the fringe contrast of the momentum distribution of the system averaged for several experimental realizations. A very interesting feature of this kind of experiment is the observation of shot-to-shot phase fluctuation, that can be induced by quantum or thermal fluctuations [43]. The dependence of these fluctuations on the temperature can be exploited to measure the condensate temperature well below the transition temperature, in a regime where the classical method of letting a single condensate expand to observe and quantify the fraction of thermal atoms fails [44]. To have an idea of involved quantities, the observed

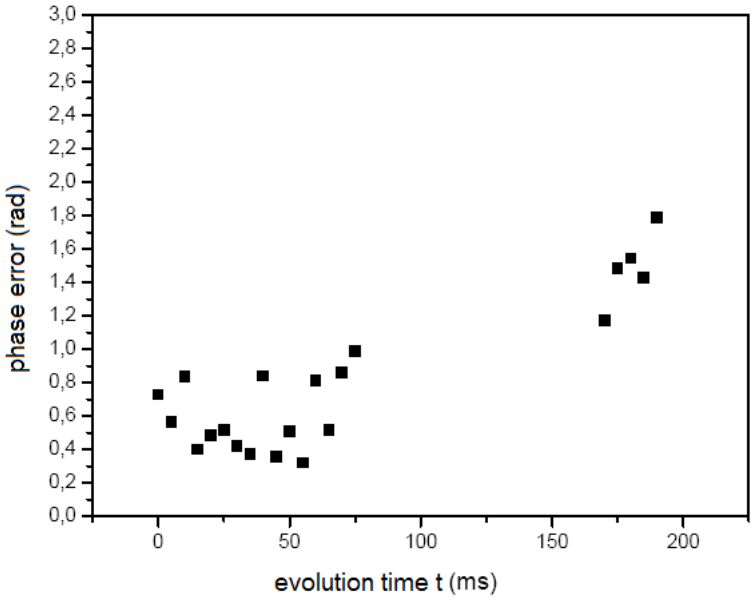


Figure 5.3.3: Phase standard deviations for different phase accumulation times

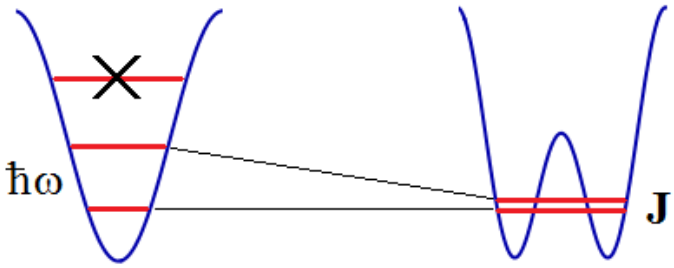


Figure 5.4.1: We assume to start with a thermal occupation of the first two levels of the harmonic potential and that during the adiabatic splitting the thermal occupation does not change.

transition temperature for atoms in our trapping potential is estimated to be of the order of 120 nK ; even for temperatures of the order of $0.1\,T_C = 12\,nK$ in a 3D harmonic trap confinement the relative fraction of thermal atoms on the total would be only 0.001, while their effect on phase fluctuations would be still quite clear.

Introducing some simplifying assumptions we exploited an experimental measurement on phase fluctuations in the double-well system to infer an upper-bound limit for the initial temperature of the system, before the splitting. Although these assumptions are quite strong, they all go in the same direction - leading to an overestimation of the role of thermal fluctuations.

The first hypothesis is to have a thermal occupation of Fock states$|N-n\rangle_g |n\rangle_e$ in the energy eigenstate basis, approximating the single harmonic well as a two-level system. Although the two-level approximation cannot be strictly justified before the splitting, we assumed to start with a low enough temperature to have not a strong deviation in the thermal distribution of atoms, and that atoms in the higher excited levels would contribute reducing the system coherence. The second assumption is that all the observed phase fluctuations are produced by thermal excitations only; actually we attribute the majority of the observed fluctuations to technical noise, both in the preparation phase of the system and in the balance between the two wells. For this reason keeping into consideration only thermal effects greatly overestimates their effect on coherence. The last one is (Figure 5.4.1) that during the adiabatic splitting the thermal occupation of the two levels does not change, although their energy difference is reduced, corresponding to an effective cooling of the system. Again, should this assumption break down, the experimental coherence factor would reduce, and this reduction that would be again ascribed to the starting thermal distribution, overestimating the initial temperature.

Another important fact is that the operatorial part of the coherence factor is the same of the non-interacting Bose-Hubbard Hamiltonian for a symmetric potential, corresponding to the tunneling term only. The coherence factor, the tunneling Hamiltonian after the splitting and the single Harmonic well Hamiltonian are diagonal in the Fock energy eigenstate basis.

The calculation consisted in comparing the experimental coherence factor $\alpha_{exp}$ with the calculated coherence factor from the starting thermal distribution

$$\alpha\left(T\right)=\sum_{n}exp\left(-\frac{\hbar\omega_T}{k_BT}n\right)\langle n|\,\frac{2\hat{J}_x}{N}\,|n\rangle \tag{5.4.2}$$

To calculate the value of the experimental coherence factor I started from a measurement of

the phase standard deviation, for which we obtained $\sigma_\varphi = 0.25\, rad.$ Assuming a Gaussian distribution of the phase I used the experimental standard deviation in the classical definition of the coherence factor (1.3.30)

$$\alpha_{exp} = \langle Cos\,(\varphi)\rangle = \frac{1}{\sigma_\varphi\sqrt{2\pi}}\int \mathsf{d}\varphi\, Cos\,(\varphi)\, e^{-\frac{\varphi^2}{2\sigma_\varphi^2}} \simeq 0.97 \tag{5.4.3}$$

and I found the temperature that satisfied the condition

$$\alpha\,(T) = 0.97 \tag{5.4.4}$$

corresponding to a maximum initial temperature of 15 nK in the harmonic trap, that reduces during the splitting to

$$T\,(E_J) = 3.25\frac{\mathcal{J}}{k_B} \tag{5.4.5}$$

For example, for the tunneling energy value measured with the Rabi oscillations, we would obtain a temperature

$$T_f \leq 2\, nK \tag{5.4.6}$$

# Conclusions

In this Thesis work I report the development of a double-well trapping potential for high sensitivity atom interferometry, studies on quantum entanglement and simulation of condensed matter physics, employing a $^{39}K$ BEC with tunable interactions. The most important result we obtained so far is the observation of coherent evolution of the non-interacting system in phase, under the effect of a controlled energy imbalance between the two localized spatial modes of the interferometer, and in population, allowing atoms to tunnel from one well to the other, over the extraordinary timescale of $\sim 200\,ms$. This result confirms this experiment at the avant-garde among systems employing a macroscopic number of condensed atoms in a micrometric double-well system. Studying the coherent evolution has proven to be the ideal testbed for the system performance, providing from one side a quantitative estimation of the system stability, from the other giving us the means to experimentally characterize the confining potential and system parameters. Indeed we have been able to quantify the Bose-Hubbard Hamiltonian parameters, namely the energy imbalance and the tunneling energy, from the direct observation of the oscillation frequencies. The open issue at the moment is the large (of the order of ten times the Shot Noise Limit) value of phase fluctuations right after the system preparation, and their increase during the evolution of the system. This indicates that the degree of control on the potential parameters (tunneling and well imbalance) and their stability is still to be improved. During the period of my Thesis we worked primarily on technically improving the system against noise sources. The objective at the moment is to increase the interferometer reliability to a satisfying degree in absence of interactions before moving to quantum enhanced interferometry. Among the improvements that allowed us to observe such a long coherence time, I presented in this Thesis the optimization of the last steps of the evaporative process that allowed us to achieve the necessary reduction of

excitations in our trapped condensate. Increasing the power we have at disposition for the green lattice beams employing the new Second Harmonic generation crystal I mounted will allow us to reduce the beam focusing in the crossing region, increasing the power and period uniformity of the lattice, that is of critical importance to have an high number of high-fidelity replicas of the same double well potential.

I reported the application on our system of a method to roughly estimate an upper bound for the condensate temperature from the coherence of the phase measurements. This is very important for metrological applications, since the system performance is highly susceptible to thermal fluctuations even for small fractions of the condensate transition temperature, where the thermal fraction of atoms is very small and cannot be directly observed and quantified in free expansion. We estimated an upper bound for the initial temperature of 15 nK, but we expect this value to be strongly influenced by technical sources of decoherence, and an estimation closer to the true value will be obtained once the system will be further stabilized.

# Special Thanks

I would like to thank professor Massimo Inguscio for being my supervisor in this Thesis work and for involving me in the fascinating world of ultracold atoms physics since I was still a bachelor student. I am grateful for the rare opportunity it has been given to me to participate in this growing and interesting field of research. I also thank professor Giovanni Modugno for having allowed me to work in the laboratory under his responsibility and for encouraging my efforts.

I also want to thank all the people I worked with during these months. Marco Fattori, for being always disposed to dedicate time and personal energies to help me achieving my objectives and deepening my understanding of the research topic, and for his constant advice and support. Giacomo Spagnolli, Andreas Trenkwalder, Manuele Landini and Giulia Semeghini for their patience in following me and explaining me the experimental operations, especially in the first months when I was still getting acquainted with experiment, for the stimulating discussions both about the underlying physics and technical aspects of the experiment and for the good time spent together during lunchtime. All these people contributed in making this one of the most constructive and interesting experience I have lived so far.

I also thank professor Augusto Smerzi for the interesting discussion about theoretical aspects of spin squeezing and for correcting some of my misconceptions about its connections with quantum entanglement.

Voglio infine ringraziare tutte le persone che mi hanno accompagnato in questo viaggio. La mia famiglia per avermi fornito tutti i mezzi necessari per raggiungere questo importante traguardo, Teresa per essermi stata vicina con il suo affetto anche nei momenti in cui sono stato maggiormente assorbito dal lavoro, e gli amici, con cui è sempre un piacere dividere il tempo libero.

# Bibliography


[1] S.N. Bose, "Plancks Gesetz und Lichtquantenhypothese", Z. Phys. 26, 178 (1924).

[2] A. Einstein, "Quantentheorie des einatomigen idealen Gases", Sitzungsber. Kgl. Preuss. Akad. Wiss. 261 (1924) , 3 (1925).

[3] M. H. Anderson, J. R. Ensher, M. R. Matthews, C. E. Wieman, E. A. Cornell, "Observation of Bose-Einstein Condensation in a Dilute Atomic Vapor " Science 269, 198 (1995).

[4] K. B. Davis, M. O. Mewes, M. R. Andrews, N. J. van Druten, D. S. Durfee, D. M. Kurn, W. Ketterle, "Bose-Einstein Condensation in a Gas of Sodium Atoms" Phys. Rev. Lett 75, 3969 (1995).

[5] K. Huang, "Statistical Mechanics" , Capp. 8,12.

[6] V.Bagnato, D. Kleppner "Bose-Einstein condensation in low-dimensional traps", Phys. Rev. A 44, 7439 (1991).

[7] A. L. Gaunt, T. F. Schmidutz, I. Gotlibovych, R.P. Smith, Z. Hadzibabic "Bose-Einstein Condensation of Atoms in a Uniform Potential", Phys. Rev. Lett. 110, 200406 (2013).

[8] Z. Yan "General thermal wavelength and its applications" Eur. J. Phys. 21, 625 (2000).

[9] F. Dalfovo, S. Giorgini , L.P. Pitaevskii, S. Stringari "Theory of Bose-Einstein condensation in trapped gases", Rev. Mod. Phys. 71, 463 (1999).

[10] J. Javanainen, M.Y. Ivanov, "Splitting a trap containing a Bose-Einstein condensate: Atom number fluctuations", Phys. Rev. A 60, 2351 (1999).

[11] G. J. Milburn ,J. Corney, E. M. Wright, D. F. Walls, "Quantum dynamics of an atomic Bose-Einstein condensate in a double-well potential", Phys. Rev. A 55, 4318 (1997).

[12] R. W. Spekkens, J. E. Sipe, "Spatial fragmentation of a Bose-Einstein condensate in a double-well potential", Phys. Rev. A 59, 3868 (1999).

[13] C. T. Lee, "Q representation of the atomic coherent states and the origin of fluctuations in superfluorescence", Phys. Rev. A 30, 3308 (1984).

[14] M.Kitagawa, M. Ueda, "Sgueezed spin states", Phys. Rev. A 47, 5138 (1993).

[15] A. Sørensen, L.-M. Duan, J. I. Cirac, P. Zoller, "Many-particle entanglement with Bose-Einstein condensates", Nature 409, 63 (2001).

[16] C.Gross, T.Zibold, E.Nicklas, J.Estève, M.K. Oberthaler, "Nonlinear atom interferometer surpasses classical precision limit" , Nature 464, 1165 (2010).

[17] C.Gross "Spin squeezing and non-linear atom interferometry with Bose-Einstein condensates", PhD dissertation, Heidelberg University. (2010).

[18] V.Giovannetti, S. Lloyd, L. Maccone, "Quantum-Enhanced Measurements: Beating the Standard Quantum Limit", Science 306, 1330 (2004).

[19] V.Giovannetti, S. Lloyd, L. Maccone, "Quantum Metrology", Phys. Rev. Lett. 96, 010401 (2006).

[20] F. Piazza, L. Pezzé, A. Smerzi ,"Macroscopic superpositions of phase states with Bose-Einstein condensates", Phyis. Rev. A 78, 051601(R) (2008)

[21] Y. Shin, M. Saba, T. A. Pasquini, W. Ketterle, D. E. Pritchard, and A. E. Leanhardt, "Atom Interferometry with Bose-Einstein Condensates in a Double-Well Potential", Phys. Rev. Lett. 92, 050405 (2004).

[22] T. Schumm, S. Hofferberth, L. M. Andersson, S. Wildermuth, S. Groth, I. Bar-Joseph, J. Schmiedmayer, P. Krüger, "Matter-wave interferometry in a double well on an atom chip", Nature Physics 1, 57 (2005)

[23] G. Spagnolli, "Experimental realization of a bosonic Josephson junction using two weakly linked $^{39}K$ Bose-Einstein condensates", Master's Degree Thesis, Università Degli Studi di Milano (2012).

[24] M.Landini "A tunable Bose-Einstein condensate for quantum interferometry", PhD Dissertation, Università Degli Studi di Trento (2011).

[25] M. Landini, S. Roy, G. Roati, A. Simoni, M. Inguscio, G. Modugno, M. Fattori "Direct evaporative cooling of $^{39}K$ atoms to Bose-Einstein condensation" Phys. Rev. A 86, 033421 (2012).

[26] L. De Sarlo, P. Maioli, G. Barontini, J. Catani, F. Minardi, M. Inguscio "Collisional properties of sympathetically cooled $^{39}K$" Phys.Rev. A 75, 022715 (2007).

[27] C. Fort, A. Bambini, L. Cacciapuoti, F.S. Cataliotti, M. Prevedelli, G.M. Tino, M. Inguscio "Cooling mechanisms in potassium magneto-optical traps", Eur. Phys. J. D 3, 113-118 (1998).

[28] M. Landini, S. Roy, L. Carcagnì, D. Trypogeorgos, M. Fattori, M. Inguscio, G. Modugno, "Sub-Doppler laser cooling of potassium atoms", Phys. Rev. A 84, 043432 (2011).

[29] K. Dieckmann, R. J. C. Spreeuw, M. Weidemüller, J. T. M. Walraven, "Two-dimensional magneto-optical trap as a source of slow atoms", Phys. Rev. A 58, 3891 (1998).

[30] T. Lauber, J. Küber, O. Wille, and G. Birkl, "Optimized Bose-Einstein-condensate production in a dipole trap based on a 1070-nm multifrequency laser: Influence of enhanced two-body loss on the evaporation process", Phys. Rev. A 84, 043641 (2011).

[31] M.Bass, E.W . Van Stryland, D.R . Williams, W.L . Wolfe, "Handbook Of Optics Volume II", Chapter 38.

[32] D.A. Kleinman, "Nonlinear Dielectric Polarization in Optical Media", Phys. Rev. 126, 1977 (1962).

[33] A.Yariv "Quantum Electronics".

[34] J.A. Armstrong, N. Bloembergen, J.Ducuing, P. S. Pershan, "Interactions between Light Waves in a Nonlinear Dielectric", Phys. Rev. 127, 1918 (1962).

[35] M. Bass, P. A. Franken, A. E. Hill, C. W. Peters, G. Weinreich, "Optical Mixing", Phys. Rev. Lett. 8, 18 (1962).

[36] N.M. Kroll, "Parametric Amplification in Spatially Extended Media and Application to the Design of Tuneable Oscillators at Optical Frequencies", Phys. Rev. 127, 1207 (1962).

[37] A.Bruner, D. Eger, M.B. Oron, P.Blau, M. Katz, "Temperature-dependent Sellmeier equation for the refractive index of stoichiometric lithium tantalate", Opt. Lett. 28, 194 (2003).

[38] I. Dolev, A. Ganany-Padowicz, O. Gayer, A. Arie, J. Mangin, G. Gadret, "Linear and nonlinear optical properties of MgO:$LiTaO_3$", Appl Phys B 96, 423 (2009).

[39] G.D. Boyd, D.A. Kleinman , "Parametric Interaction of Focused Gaussian Light Beams", J. Appl. Phys. 39, 3597 (1968).

[40] G. K. Samanta, S.C. Kumar, M. Ebrahim-Zadeh "Stable, 9.6 W, continuous-wave, single-frequency, fiber-based green source at 532 nm", Opt. Lett. 34, 1561 (2009).

[41] T. Freegarde, J. Coutts, "General analysis of type I second-harmonic generation with elliptical Gaussian beams", J. Opt. Soc. Am. B 14, 2010, (1997).

[42] E.Lippi, "Coherent dynamics of a Bose-Einstein condensate in a double well potential", Bachelor Degree Thesis (in italian), Università Degli Studi di Firenze (2014).

[43] L. Pitaevskii1, S. Stringari "Thermal vs Quantum Decoherence in DoubleWell Trapped Bose-Einstein Condensates", Phys. Rev. Lett. 87, 402 (2001).

[44] R. Gati, B. Hemmerling, J. Fölling, M. Albiez, M. K. Oberthaler, "Noise Thermometry with TwoWeakly Coupled Bose-Einstein Condensates", Phys. Rev. Lett. 96, 130404, (2006)

[45] R.Gati, "Bose-Einstein Condensates in a Single Double Well Potential", PhD dissertation, Heidelberg University (2007).

[46] T.B. Ottenstein "Few-body physics in ultracold Fermi gases", PhD dissertation, Heidelberg University (2010).